ADDIS ABABA UNIVERSITY

COLLEGE OF NATURAL AND COMPUTATIONAL SCIENCES

SCHOOL OF EARTH SCIENCES

MONITORING OF RICE CROP USING SENTINEL 2 OPTICAL AND SENTINEL 1 RADAR IMAGES IN FOGEREDA WEREDA, ETHIOPIA

By:

TESHOME TALEMA

GSR/7326/09

Advisor:

Dr. BINYAM TESFAW

A Thesis submitted to

School of graduate studies of Addis Ababa University in Partial Fulfillment of the requirements for the Degree of Masters of Science in Remote Sensing and Geo-informatics

Addis Ababa, Ethiopia
June, 2018

ADDIS ABABA UNIVERSITY

COLLEGE OF NATURAL AND COMPUTATIONAL SCIENCES

SCHOOL OF EARTH SCIENCES

MONITORING OF RICE CROP USING SENTINEL 2 OPTICAL AND SENTINEL 1 RADAR IMAGES IN FOGEREDA WEREDA, ETHIOPIA

By:

TESHOME TALEMA

GSR/7326/09

A Thesis submitted to

School of graduate studies of Addis Ababa University in Partial Fulfillment of the requirements for the Degree of Masters of Science in Remote Sensing and Geo-informatics

Addis Ababa, Ethiopia

June, 2018

Addis Ababa University

School of Graduate Studies

This is to certify that thesis prepared by **TESHOME TALEMA MEKONNEN**, entitled: "Monitoring of Rice Crop using Sentinel 2 Optical and Sentinel 1 RADAR images in Fogera Wereda, Ethiopia" and submitted in partial fulfillment of the requirements for the degree of Masters of Science in Remote sensing and Geo-informatics complies with the regulations of the University and meets the accepted standards with respect to the originality and quality.

Signed by the Examining committee:

Examiner

..... Signature_____ Date _____

..... Signature_____ Date _____

Advisor

Dr. Binyam Tesfaw Signature _____Date _____

Co-Advisor

---------- Signature_____ Date _____

Chairperson

---------- Signature_____ Date _____

Acknowledgements

My heartfelt gratitude goes to my advisor Dr. Binyam Tesfaw for his in-depth comments, guidance and shaping the general structure of my thesis. Indeed, the work would have not successfully been completed without his continued support. I would like to thank Dr. Binyam, not only advising in this work but also for his academic and educational support in my stay in the university. I am also truly indebted and thankful to Dr. Tesfaye Korme for his support during my study period.

I acknowledge to my office Central Statistical Agency (CSA) for giving the sponsorship to learn my MSc and every kind of support I get from the office. I would also like to thank School of Earth Sciences; Remote Sensing and Geo -informatics Stream for accepting me to join the university and for all the support and cooperation I get from the department and academic staff there during my study.

I would like to express my sincere thanks to European Space Agency (ESA) for providing me with the free SAR data to carry out the research work.

I acknowledge the Ethiopian Metrological Agency and Geological Survey of Ethiopia for their kindness in providing the necessary data and information to carry out this research. Finally, I would like to give my heartfelt thanks to my work college to Sewunet Shiferaw who always encourages me in all my works.

Table of Contents

List of Tables

List of Figures

List of Appendices

Acronyms

ALOS	Advanced Land Observing Satellite
ASAR	Advanced Synthetic Aperture Radar
ASF	Alaska Satellite Facility
CCRS	Canadian Center for Remote Sensing
CSA	Central Statistical Agency
CART	Classification and Regression Trees
dB	Decibel
DEM	Digital Elevation Model
DN	Digital Numbers
EO	Earth Observation
ERDAS	Earth Resource Data Analysis System
ENVI	Environment for Visualizing Image
Envisat	Environmental Satellite
ERS	European Remote Sensing
ESA	European Space Agency
EU	European Union
EW	Extra Wide
FAO	Food and Agricultural Organization
GPS	Global Positioning System
GRD	Ground Range Detection
HH	Horizontal transmission and Horizontal reception
HV	Horizontal transmission and Vertical reception
IWS	Interferometric Wide Swath
JERS	Japanese Earth Resources Satellite
LULC	Land-Use Land-Cover
LAI	Leaf-Area-Index
MODIS	Moderate Resolution Imaging Spectroradiometer
MNDWI	Modified Normalized Difference Water Index
NASA	National Aeronautics and Space Administration
NMA	National Metrological Agency
NIR	Near Infrared
NIR	Near Infrared

NDVI	Normalized Difference Vegetation Index
PALSAR	Phased Array type L-band Synthetic Aperture Radar
PA	Producer's Accuracy
RADARSAT	Radar Satellite
RADAR	Radio Detection And Ranging
RGB	Red, Green, Blue
SAFE	Standard Archive Format for Europe
SM	Strip Map
SNAP	Sentinel Application Platform
SWIR	Shortwave Infrared
SRTM	Shuttle Radar Topography Mission
SAFE	Standard Archive Format for Europe
SAR	Synthetic Aperture Radar
SPOT	Systeme Probatoire d'Observation de la Terre
TOA	Top Of the Atmosphere
TOPSAR	Terrain Observation with Progressive Scans Synthetic Aperture Radar
UA	User's Accuracy
UTM	Universal Transverse Mercator
VH	Vertical transmission and Horizontal reception
VV	Vertical transmission and Vertical reception
VNIR	Visible Near Infrared
WM	Wave Mode

Abstract

Though optical remote sensing has various importance for land-cover mapping and monitoring, it is very difficult to assess and monitor rice agriculture over large areas due to cloud cover on the images and the nature of rice agriculture. Therefore, in this study, Sentinel 1 RADAR and Sentinel 2 images were integrated to alleviate this problem. Specifically, time series Sentinel 1 RADAR Interferometric Wide images were utilized to identify optimal polarization, map rice extent, and inundation in the rice fields of Fogera wereda, Ethiopia, during the 2017 growing season. To map paddy fields using Sentinel 1 RADAR, first extracting the temporal backscatter value of rice fields and background land-cover types at the vertical transmitted and vertically received (VV) and vertically transmitted and horizontal received (VH) polarizations of Sentinel 1 RADAR data. From Sentinel 1 RADAR, the temporal backscatter value of rice increased sharply at the early planting stage and decreased during the high flooding stages as well as relatively the same temporal backscatter of the other land-cover types like rice. However, the increase in rice backscatter is more sustained at the Sentinel 1 RADAR VH polarization, and two-class separability measures further showed the superiority of VH over VV in discriminating rice fields. CART model was used for the identification of optimal node of sentinel 1 RADAR VH images, that is used to different time mapping of rice. The rice extent extracted from CART optimal node was 20,911.2 ha for 14 June 2017 and 19,892.5 ha for 01 August 2017 growing seasons. Then, the temporal VH images of Sentinel 1 RADAR was combined with the normalized difference vegetation index (NDVI) and the modified normalized difference water index (MNDWI) derived from a single-date cloud-masked Sentinel 2 image (October 09, 2017). The integration of these optical indices with temporal backscatter eliminated all commission errors in the rice class and increased overall accuracy by 9.6%, demonstrating the complementary role of optical indices to Sentinel 1 RADAR data in mapping rice fields in tropical areas such as Fogera. The refined land use land-cover map identified by integrating Sentinel 1 RADAR and Sentinel 2 optical indices rice area was 19,157.8 ha with general ($R^2 = 0.94$) agreement with wereda census statistics. This study shows that the freely available Sentinel 1 RADAR images are important and applicable for assessing and monitoring paddy rice.

Keywords: Sentinel 1 RADAR; Sentinel 2; Fogera wereda; CART; rice mapping

CHAPTER ONE

1. Introduction

1.1 Background of the Study

Rice (*Oryza sativa*) is one of the world's major agricultural crops (Torbick *et al.,* 2017) and is the staple food for more than half of the world population (Dawe *et al.,* 2010). The Asian rice, *Oryza sativa* and African rice *Oryza glaberrima* were the two most cultivated species (Reddy, 2004). The basis for rice introduction in Ethiopia was the adaptation of wild rice in Amhara region Fogera plain in the early 1970s (Astewul Takele, 2010). In the early 1980s through the technical support of North Korean experts, research on rice was initiated in Shaga (Fogera wereda) cooperatives. This was, however, discontinued when farmers' cooperatives were dismantled in 1991 (Getachew Afework, 2000). In the 1990s, rice agricultural extension service was one of the major focus areas in both Fogera and the region. However, all attention was given to the lowland paddy rice variety in the six Kebeles or small districts of Fogera wereda. During the early days of rice introduction, the extension system was geared towards promoting rice production to more farmers. Farmers were, therefore, provided with free inputs (seeds and fertilizer) and more farmers were also trained on the agronomic practices. Despite all these efforts, there was resistance due to the wrong perception that rice causes infertility in humans (Tilahun *et al.*, 2012). This, however, ceased as time went by, through strong extension and research systems. In 1993, 30 households (HHs) in two Kebeles of Fogera wereda planted six hectares of land and produced 16 tone with an average yield of 2.67 t/ha using the X-Jigna variety (Tilahun et al., 2012). X-Jigna was the dominant rice variety grown in the wereda on the flooded plain (Tilahun et al., 2012). In 2005, the area expanded to around 6871 ha producing about 28,877 tone (4.0 t/ha), while the number of agricultural households increased to 12,770 (Tilahun *et al.,* 2012). With the continuous engagement of extension systems, rice production has been expanding in the low-lying areas. Producers used rice for food (Injera and Bread) and local alcoholic drinks like 'Tela' and 'Arekie'. Rice was also a cash crop. Rice straw and stubble were also used as a source of animal feed and for house construction. Using rice bran which was very important as livestock feed was not well known. Nowadays rice cultivation is the main crop in Fogera wereda. The most widely and easily monitored variable of rice cultivation is acreage. Under the assumption of ceteris paribus, an increase in the rice planted area should translate to an increase in rice productivity and food supply (Mansaray *et al.,* 2017; Torbick *et al.,* 2017). Monitoring rice acreage with traditional ground-based surveys is time and labor consuming and also requires huge finance for resource mobilization especially when it is implemented at large scales (Shen *et*

al., 2009; Bouvet and Le Toan, 2011). Thus, remote sensing technology has been increasingly applied to provide data on rice planted areas at a variety of spatial scales with minimal finance, time and human resources. Both optical and RAdio Detection and Ranging (RADAR) remote sensing data have been exploited to map and monitor rice growth (Mansaray *et al.,* 2017). Compared to optical data, the use of Sentinel 1 RADAR data in agricultural applications has not been well developed, partly due to the complexity, diversity, and availability of RADAR data, and partly due to the difficulty of data interpretation (Veloso *et al.,* 2017).

Up to now, monitoring crop dynamics was hampered by the lack of availability of high temporal and spatial resolutions satellite time series. A new era started with the launch of the first Sentinel satellite developed by the European Space Agency, providing a large and unprecedented amount of free data for the operational needs of the Copernicus program (Veloso *et al.,* 2017). Sentinel 1 RADAR, the first SAR (Synthetic Aperture Radar) satellite, launched in April 2014, has started to provide multi-temporal series of SAR imagery (C-band) at an outstanding time interval of 12 days. With Sentinel-1B, launched in April 2016, the data provision is expected for every 6 days. Sentinel-2A, the optical satellite, launched in June 2015, provides data at an interval of 10 days. With Sentinel-2B launched in March 2017, the time interval should be 5 days. The relatively dense time series of Sentinels offer a unique opportunity to systematically monitor crops at a weekly repeat cycle (from 5 to 12 days, depending on the data type and the region in the world). In addition, the continuity of Sentinel data is guaranteed up to 2030 and the next generation of Sentinel is planned beyond 2030, allowing long-term environmental monitoring (Veloso *et al.,* 2017). So far, few studies have been using dense time series SAR data for crop monitoring. Only recently, Sentinel 1 RADAR data have been used (Navarro *et al.,* 2016).

However, as optical datasets are frequently contaminated by clouds in tropical areas, Sentinel 1 RADAR datasets are increasingly being preferred especially in rice area estimation due to their all-weather imaging capability (Koppe *et al.,* 2013). Microwave data are complementary to optical data, and in cloud-prone tropical regions, they could be the preeminent data for monitoring paddy rice fields. Mapping rice planted areas using optical satellite remote sensing data is primarily based on the exploitation of the crop's apparent reflectance characteristics in the visible near-infrared (VNIR) portions of the electromagnetic spectrum. It has been observed that after twelve weeks of growth, the reflectance of paddy rice in the near-infrared (NIR) reaches the highest value, while in the visible region it reaches the lowest value (Chang *et al.,* 2005). The diagnostic spectral reflectance exhibited by paddy rice during growth and their associated temporal vegetation indices have been mostly utilized to discriminate the crop from other land-cover categories using optical remote sensing datasets such as Sentinel-2A optical imagery and

the Moderate Resolution Imaging Spectroradiometer (MODIS), which is the flagship of NASA's Earth Observing System (EOS) program. On the other hand, mapping paddy rice using microwave (Synthetic Aperture Radar) satellite data is based on the backscatter response, which is largely a function of growth stage and environmental conditions (Yonezawa *et al.*, 2012).

Backscattering mechanism in the case of rice crop during its growth cycle includes; surface scattering, volume scattering, and surface scattering attenuated by the vegetation volume (Zhang *et al.*, 2009). Prior to sowing/planting, paddy rice fields are flooded and a characteristic low backscatter is observed at this stage due to a dominance of smooth or specular reflections from the water surface (Kuenzer and Knauer, 2013). As the rice grows, a significant increase in backscatter is recorded as a result of multiple scattering (double-bounce) effects involving the water surface and the vertical elements of the crop (Zhang *et al.*, 2009). It is this temporal backscatter change that has been exploited to discriminate the rice crop from other surfaces using microwave remote sensing data such as Sentinel 1 RADAR SAR images (Torbick *et al.*, 2017). A number of studies have explored the comparative advantages of integrating optical and microwave remote sensing datasets for more efficient and accurate crop classifications (Torbick *et al.*, 2017).

These research works have used both optical and microwave remote sensing datasets to map paddy rice based more complex and efficient machine learning algorithm of classification and regression trees (CART). For this study six images from the new generation Sentinel 1 RADAR and Sentinel 2 optical indices used to discriminate paddy rice field in Fogera wereda, at the 2017 rice growing season.

1.2 Statement of the problem

Rice is a heat and water-loving crop. Mapping and monitoring rice crop using time series optical remote sensing data are not possible due to high cloud coverage (Yun *et al.*, 2001; Nguyen Lam-Dao, 2009; Inoue *et al.*, 2014; Nguyen and Wagner, 2017). In Ethiopia, crop monitoring studies were mostly done at regional/national levels covering large areas using low-resolution imagery, small sample units, and few field verifications. Previous studies on rice mapping in Fogera wereda were carried out using different kinds of optical data during Bega (January, February, and March) season where no cloud obstruction was found. A large part of rice crop growing cycle coincides with the rainy season, resulting in only a limited number of cloud-free optical images being possible (Gerald *et al.*, 2014; Balzter *et al.*, 2015; Mansaray *et al.*, 2017). Traditionally, estimates of rice planting area and productivity are based on ground survey data. While ground data collection has some merits, it is often time-consuming and expensive. In addition, the information collected is often imprecise and unreliable, leading to inaccurate crop yield forecasts

and subsequent difficulties for agriculture planners and managers in both regional and national scales (Yun *et al.*, 2001; Nguyen Lam-Dao, 2009; Aboelghare *et al.*, 2011). Earth observation from space allows regular and timely monitoring of rice cultivated areas and can provide accurate information about the status of rice growth. Hence, the use of remote sensing data acquired at the appropriate time expected to help in producing synoptic rice field maps. Mapping of rice crop using optimal polarization VV/ VH Sentinel 1 RADAR image is important to know the backscatter variation of rice at different growth stages (Mansaray *et al.*, 2017). The data of optical remote sensing satellites such as Systeme Probatoire d'Observation de la Terre (SPOT) is used due to its advantage in resolution, both radiometric and spatial. The disadvantage of the optical data is due to the presence of cloud on the images. Thus, it becomes ineffective in establishing land cover map in cloudy covered areas. It becomes inconsiderable in establishing land cover map in cloudy covered areas. However, microwave remote sensing data are not affected by cloud, rather by the relief, so that the integrated approach of using optical and time series microwave (SAR) remote sensing data in rice mapping and monitoring could be robust in rice mapping and monitoring.

1.3 Objectives

1.3.1 General Objective

The general objective of this study was to monitor rice crop using Sentinel 1 RADAR and Sentinel 2 Optical remote sensing data in Fogera wereda, Ethiopia.

1.3.2 Specific objectives

The specific objectives of the present study were:

- To identify the optimal polarization (VV or VH) for rice crop area (acreage) mapping and other land-cover classification.
- Integrating Sentinel 1 RADAR and Sentinel 2 Optical satellite images in order to map rice fields more precisely.
- To validate rice crop map prepared using remote sensing data with the help of field data.
- To map rice inundation using moderate-scale and high temporal frequency Sentinel 1 RADAR optimal imageries.

1.4 Research Questions

The following questions have been formulated to achieve the above-mentioned objectives.

- Which polarization of Sentinel 1 RADAR image VV/VH is good for rice mapping and monitoring?

- How to map rice cropland by integrating Sentinel 1 RADAR and Sentinel 2 Optical satellite imageries?
- How to map rice inundation area using Sentinel 1 RADAR time series imageries?

1.5 Significance of the study

Previous research studies on rice mapping and monitoring were carried out using different kinds of SAR data (e.g. ERS-SAR, RadarSat, JERS-SAR, and Envisat-ASAR) in different geographical sites particularly in tropical and temperate regions of the world (Nguyen Lam-Dao, 2009). The mapping of rice cropping systems from data acquired by these relatively new Sentinel 1 RADAR imageries has been rarely reported in the scientific literature.

Generally, this research is significant for the following reasons:

- This research study introduces the application of Sentinel 1 RADAR images for rice and another land-cover mapping in Ethiopia.
- The identified optimal polarization (VV or VH) Sentinel 1 RADAR imagery that is better for rice mapping will be used for later researchers.
- The research provides a good understanding of integrating time series Sentinel 1 RADAR and optical remote sensing data in rice mapping.

1.6 Limitation of the Study

The major limitations concerned to this study were the data availability at the relevant acquisition mode and the specific time of rice growth stage, especially cloud free Sentinel 2 optical images. The first limitation was that the used imagery was VV (Vertical transmission and Vertical reception) and VH (Vertical transmission and horizontal reception) polarizations. The VV polarization is subjected to the effect of diffuse reflection by vegetation than the HH (Horizontal transmission and Horizontal reception) polarization. Although VH polarization is promising in mapping paddy rice, it is highly accurate by HH transmission and reception method than the VH polarization. Therefore, because of unavailability of HH polarization during the time of 2017 rice-growing season in the study area, the study was limited to use VV and VH polarization of radar signal recording system.

Secondly, Sentinel 1 RADAR image is a recent satellite image, lack of enough literature to review is one of the limitations of this research study. Most of the research studies previously done were based on currently not functioning type of SAR data like Envisat ASAR, Radarsat-1, Radarsat-2 etc. of satellite images.

1.7 Scope of the Study

The spatial extent of the study was limited to the Fogera wereda, Ethiopia. It aims to conduct the study on Fogera wereda through the use of remote sensing technology in monitoring rice crop. Although rice mapping and monitoring using the new generation Sentinel 1 RADAR and Sentinel 2 optical satellite image is at its lowest stage in Ethiopia, there have been a number of changes in respect to the spatial and temporal resolution of satellite images in the past two years. Therefore, the main scope of the study is to map and monitor rice crop using remote sensing satellite images for the 2017 rice growing season

1.8 Organization of the Thesis

The Thesis is organized into five chapters. The first chapter is about the introduction of the paper dealing with a background of the study, statement of the problem, objectives, research questions, Significance of the study, the scope of the study, limitation of the study and organization of the paper. Chapter two gives an overview of microwave (Sentinel 1 RADAR) and Sentinel 2 optical remote sensing as a field of study for rice mapping and monitoring and the theory behind the methods used in different time mapping. It also covers the literature review on the application of Remote Sensing techniques in the study of rice monitoring. The third chapter is about the materials and methods. There are two subtitles under this portion, materials, and methodology. The subtitle Materials deals about the description of the study area, data sources and software programs used in the study while the subtitle methodology deals with all the procedures followed in image preprocessing, classification methods and analysis. Chapter four is all about results and discussions that deals with Sentinel 1 RADAR optimal images for time series rice mapping and all the results of the integrating Sentinel 1 RADAR optimal images with Sentinel 2 optical indices findings. The last chapter discusses conclusion and recommendation based on the research findings of the study.

CHAPTER TWO

2. Literature Review

2.1 Microwave remote sensing

The microwave remote sensing uses electromagnetic waves with wavelengths between 1 mm to 1 m in wavelength (Bakker *et al.*, 2001; CCRS, 2013; Calla, 2013). Compared to optical, microwaves have the following special properties that are important for remote sensing.

- Little dependence on atmospheric conditions
- Full control on the emitted (for active remote sensing) and received electromagnetic radiation: power, frequency, polarization,
- Ability to choose incidence and azimuth angles to meet the objectives of the study, and
- Possibility to obtain information on subsurface features, when low soil density and moisture permit.

These are primary advantages of using microwave/RADAR remote sensing. The microwave remote sensing encompasses both active and passive forms of remote sensing. A passive microwave sensor detects the naturally emitted microwave energy within its field of view. The active microwave sensor transmits a microwave signal towards the target and detects the backscattered portion of the signal (Figure 2.1). According to Henderson and Lewis (1998), the power scattered back toward the radar antenna is represented by the radar equation (2.1).

$$P_{R=} P_T(\sigma^\circ A)\left(\frac{G^2\lambda^2}{(4\pi)^3} R^4\right) \quad (2.1)$$

Where

P_R : the power received,

P_T : the power transmitted toward the target,

G: the gain of the antenna,

R: the range distance from the transmitter to the target,

σ°: the radar scattering coefficient,

λ: the wavelength of the radar system,

A: an area on the ground.

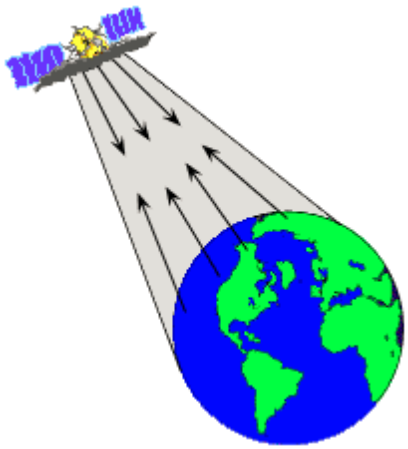

Figure 2.1: The principle of active microwave remote sensing (CCRS, 2013).

There are several advantages to be gained from the use of active sensors. It is possible to acquire data at any time of the day including during the night. Active sensors are divided into two groups: imaging and non-imaging sensors. The most common form of imaging active microwave sensor is the radar. This sensor transmits a microwave (radio) signal towards the target and detects the backscattered portion of the signal.

The second group is non-imaging active-microwave remote sensing. As opposed to imaging sensors these group of sensors is two-dimensional representations (Bakker *et al.,* 2001; Calla, 2013; Getu Tessema, 2017) of the earth's surface.

2.1.1 SAR (Synthetic aperture radar)

Synthetic Aperture Radar (SAR) is an active imaging instrument, i.e. SAR sends a pulse of electromagnetic radiation and then records the amplitude and phase of the radiation coming back from the target (Akbari, 2013; Getu Tessema, 2017). The backscattering coefficient, σ^o, is a measure describing the strength of the recorded radar signals from the target per unit area. The advantage over the optical satellite images, such as Landsat and SPOT, is that SAR uses cloud-penetrating microwaves having a wavelength of few centimeters to even meters (Sanyal and Lu, 2004). Thus, it is possible to have satellite SAR images from the target at user-specified times, which is important in agricultural monitoring where satellite images are needed regularly and the time window for image acquisition is narrow (Lopez-Sanchez *et al.,* 2011). Although it is evident that cloud-penetrating SAR has great potential in agricultural remote sensing (Nelson *et al.,* 2014). Instead, optical satellite images have channels revealing information of the photosynthetically active radiation of the vegetation, and thus, there is a well-established connection between satellite information and vegetation biomass (Nguyen Lam-Dao, 2009; Hagen *et al.,* 2012).

2.1.2 Frequency

Similarly, to optical remote sensing, microwave operate with different bands (Bakker *et al.,* 2001). The commonly used bands in microwave remote sensing are shown in (figure 2.2).

Ka (0.75 - 1.18 cm), K (1.18 - 1.67 cm) and Ku (1.67 - 2.40 cm) bands are very short wavelengths used in early airborne radar systems but uncommon today. X-band (2.40 - 3.75 cm) is used extensively on airborne systems for military reconnaissance and terrain mapping. C-band (3.75 - 7.5 cm) is common on many airborne research systems (CCRS Convair-580 and NASA AirSAR) and spaceborne systems (including ERS-1 and 2 and RADARSAT). S-band (7.5 - 15 cm) is used on board the Russian ALMAZ satellite. L-band (15 - 30 cm) used onboard American SEASAT and Japanese JERS-1 satellites and NASA airborne system. P-band (77 - 136 cm) is longest radar wavelengths used on NASA experimental airborne research system.

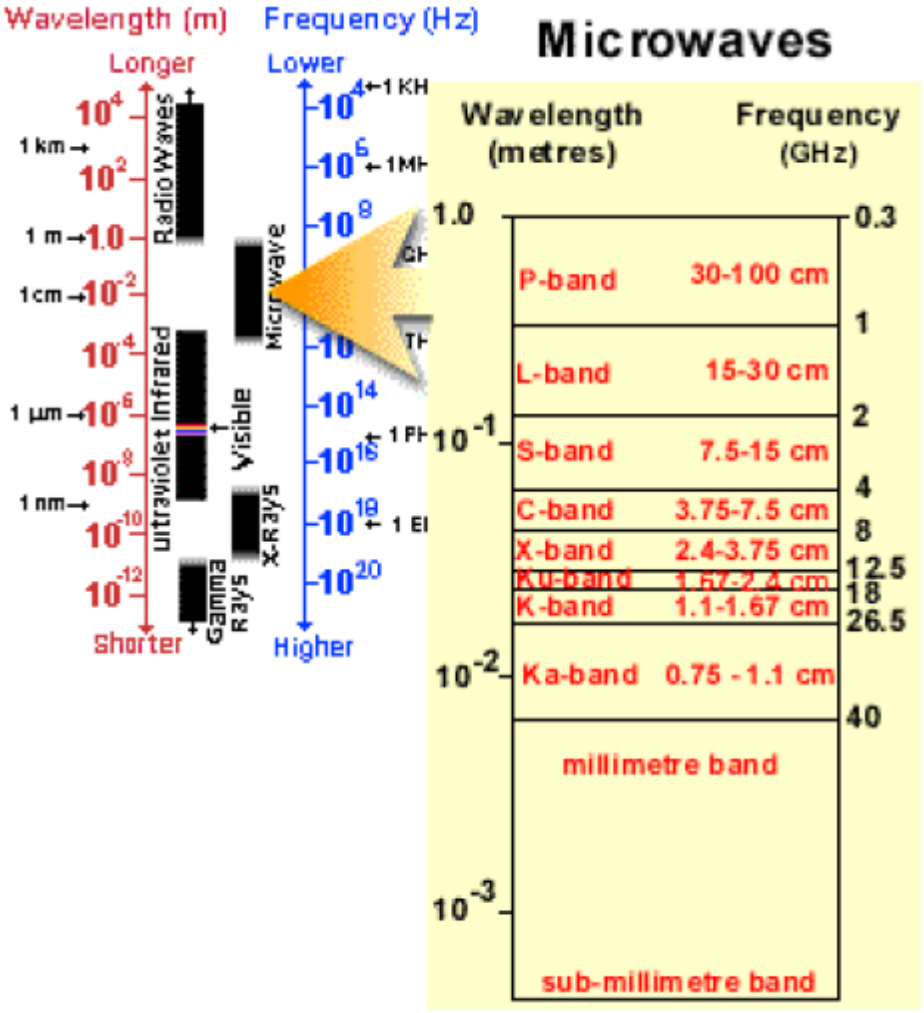

Figure 2.2: Microwave portion of the electromagnetic spectrum

2.1.3 Sentinel 1 RADAR data

Sentinel-1A Launched in April 2014 by the European Space Agency (ESA) on a SOYUZ rocket from the Kourou, Space Center in French Guiana, Sentinel-1A is the first of a series of earth observation satellites for the Copernicus Initiative. The Sentinel-1 mission is the European Radar Observatory for the joint initiative on environment and security between the European Commission and ESA (Mansaray *et al.*, 2017). Sentinel-1 is in a near-polar, sun-synchronous

orbit with a 12-day repeat cycle and 175 orbits per cycle for a single satellite. Both Sentinel -1A and Sentinel -1B share the same orbit plane with a 180° orbital phasing difference. With both satellites operating, the repeat cycle is 6 days. Sentinel-1A is a sun-synchronous, near-polar circular orbit at a height of 693 km and an inclination angle of 98.18° (Torbick *et al.,* 2017). These polar-orbiting satellites acquire images day and night regardless of weather conditions. They continue and compliment C-band imaging missions of ESA's Earth Resources Satellites (ERS 1 and ERS 2), Environment Satellite (ENVISAT), and Canada's RADARSAT-1 and RADARSAT-2 (Skolnik, 2013). The Sentinel-1 SAR instrument operates at 5.405 GHz (C-band, 5.6 cm) with VH and VV polarizations (Phuong *et al.,* 2016). Sentinel-1 presents significant advancement over previous C-band missions as stated above, in terms of spatial and temporal resolution, geographical coverage, reliability and data dissemination. The mission seeks to benefit numerous services as in sea-ice monitoring and maritime surveillance, land monitoring of forest, water, soils and agriculture, monitoring of land surface motions, and mapping to support environment, crisis, and natural disaster management.

2.1.4 Polarization

The polarization of a SAR instrument refers to the orientation of the transmitted SAR beam's electric field vector. In case of the vector oscillating in the horizontal direction, the beam is said to be "H" polarized. In case of oscillation perpendicular/vertical to the horizontal direction, the beam is known as "V" polarized. The possible combinations of Polarization in microwave remote sensing are: horizontal transmission and horizontal reception (HH), vertical transmission and vertical reception (VV), horizontal transmission and vertical reception (HV) and vertical transmission and horizontal reception (VH) (Nguyen Lam-Dao, 2009; sarmap, 2009).

This research study used VV and VH polarization imagery of SAR as a main data source for rice monitoring in the Fogera wereda.

2.1.5 Target interaction

The look direction or aspect angle of the radar describes the orientation of the transmitted radar beam relative to the direction or alignment of linear features on the surface. The look direction can significantly influence the appearance of features on a radar image, particularly when ground features are organized in a linear structure (such as agricultural crops). Look direction is important for enhancing the contrast between features in an image. By acquiring imagery from different look directions, it may be possible to enhance identification of features with different orientations relative to the radar (CCRS, 2013). The orientation of the surfaces at right angles causes most of the radar energy to be reflected directly back to the antenna due to the double bounce reflection. Corner reflectors with complex angular shapes are common in urban

environments (e.g. buildings and streets, bridges, other manmade structures). Naturally, occurring corner reflectors may include upright vegetation standing in water, e.g. rice plants. In all cases, corner reflectors show up as very bright targets in an image (CCRS, 2013).

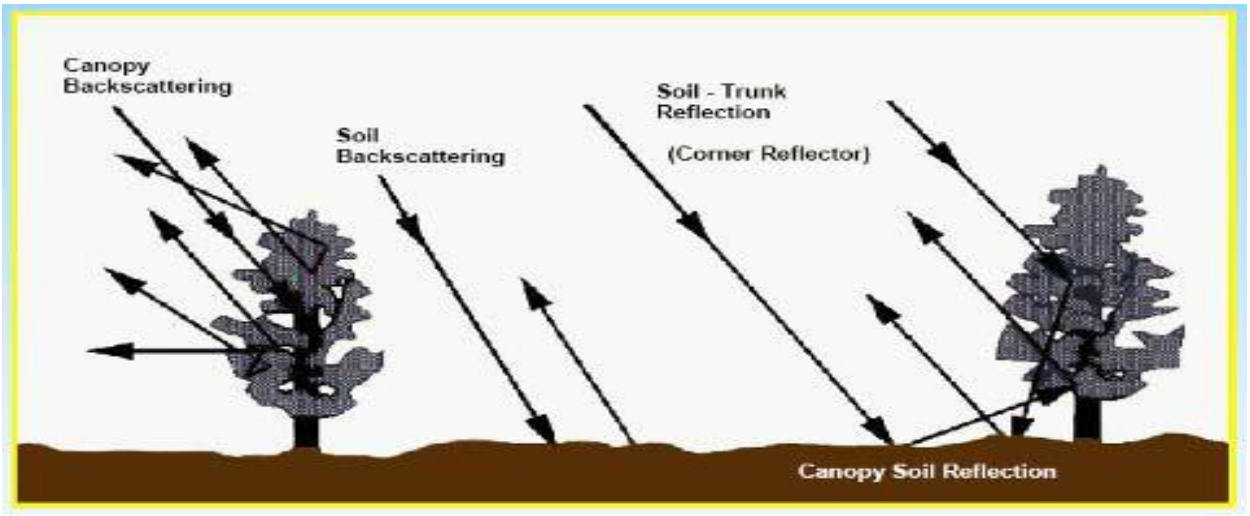

Figure 2.3: Volume scattering, surface scattering, and corner reflection (CCRS, 2013).

2.1.6 Penetration depth and frequency

The longer the microwave wavelength, the greater the penetration into the plant canopy (Skolnik, 2008). Surface scattering takes place at the top of the canopy as the energy interacts with the leaves and stems. Volume scattering by the leaves, stems, branches, and trunk takes place throughout the stand, and surface scattering can occur at the soil surface. The shorter wavelength X-band energy is more attenuated by the top of the canopy (by foliage and small branches). The C-band energy experiences scattering at the top of the canopy as well as some volume scattering in the heart of the stand. Little energy reaches the ground. L-band microwave energy penetrates farther into the canopy, where volume scattering among the leaves, stems, branches, and trunk cause the beam to become depolarized. Also, some energy may be transmitted to the ground, where surface scattering from the soil-vegetation boundary layer may take place. Longer wavelength P-band radar would afford the greatest penetration through the vegetation and mainly reflect off large stems and the soil surface (Yun *et al.*, 2000).

2.1.7 Radar backscatter and biomass

Radar backscatter increases with increasing biomass until it saturates at a biomass level that depends on the radar frequency. In the case of forest, generally, backscatter at lower frequencies (P- and L-band) is dominated by scattering processes involving the major woody biomass components (trunks and branches), while scattering at high frequencies (C- and X-band) is dominated by scattering processes in the top crown layer of branches and foliage. Radar canopy measurements have also been found to be correlated with leaf-area-index (LAI) measurements.

Some general observations about SAR vegetation interpretation include ((Nguyen Lam-Dao, 2009):

- vertically polarized energy is highly attenuated by the vertically oriented canopy components (leaves, stems, branches, and trunk) while horizontally polarized energy is not;
- the brighter the return on like-polarized radar images (HH or VV) in comparison to (HV), the greater the contribution from surface scattering.
- the brighter the return on cross-polarized radar images (HV or VH), the greater the contribution from volume (internal canopy) scattering;
- when the radar wavelength is approximately the same size as the canopy components (C- or X-band), substantial canopy surface and volume scattering will take place and little energy may reach the ground. Consequently, shorter wavelength radars (2 – 6 cm) may be preferred when monitoring crop canopies and tree leaves. Longer wavelength radars (9 – 30 cm) exhibit substantial volume scattering as incident energy interacts with a larger trunk and branch components. Considerable surface scattering from the underlying soil may also occur which can cause confusion;
- cross-polarized images (HV or VH) are less sensitive to slope variations. This suggests vegetation monitoring in mountainous areas may best be performed using cross-polarization techniques. Also, the same row crop planted in different directions can produce like-polarized images that are difficult to interpret. This ambiguity may be reduced when cross-polarized images are available in addition to like-polarized images;
- the more moisture in the vegetation canopies, the greater the dielectric constant and the higher the radar backscatter return. Active microwave remote sensing is capable of sensing canopy (or leaf) water content in certain instances;
- radar imagery can provide some information on landscape-ecology patch size and canopy gaps that are of value when monitoring ecosystem fragmentation and health.

2.2 Radar Image Properties

Spatial resolutions of Sentinel 1 radar depend on the acquisition mode and the level of processing (CCRS, 2013). To determine the spatial resolution at any point in a radar image, it is necessary to compute the resolution in two dimensions: the range and azimuth resolution (Nguyen Lam-Dao, 2009).

2.2.1 Range resolution

The range resolution (in the across-track direction) is proportional to the length of the microwave pulse. The shorter the pulse length, the finer the range resolution. According to Henderson and Lewis (1998), the equation for computing the ground range resolution Gr is shown in equation 2.2.

$$Gr = \frac{c\tau}{2 \sin \varphi} \quad (2.2)$$

Where

c: speed of light

τ: pulse length

φ: look angle

2.2.2 Azimuth resolution

The equation for the optimal azimuth or along-track resolution A_S for a point target in a synthetic aperture radar is (Henderson and Lewis, 1998).

$$As = \frac{l}{2} \quad (2.3)$$

where *l* is antenna length.

2.2.3 Speckle

Synthetic Aperture Radar (SAR) images have inherent salt and pepper like texturing called speckles which degrade the quality of the image and make interpretation of features more difficult. This is caused by random constructive and destructive interference from the multiple scattering returns that will occur within each resolution cell (Skolnik, 2008; Mansaray *et al*., 2017). Reducing speckle will enhance radiometric resolution but at the cost of spatial resolution. Speckle noise in a digital image can be suppressed by the application of a speckle removal filter, which is necessary to improve classification and enhancement before image analysis (Skolnik, 2008). Thus, it is generally desirable to reduce speckle prior to interpretation and analysis by either multi-look processing or filtering techniques. If images are processed with a small number of „looks", distribution intensities will have inconsistencies due to speckle noise. Therefore, in this case, multi-look processing is usually applied (sarmap, 2009). While multi-looking processing is usually done before the delivery of the data product, speckle reduction by temporal and spatial filtering is performed on the output image in a digital image analysis environment.

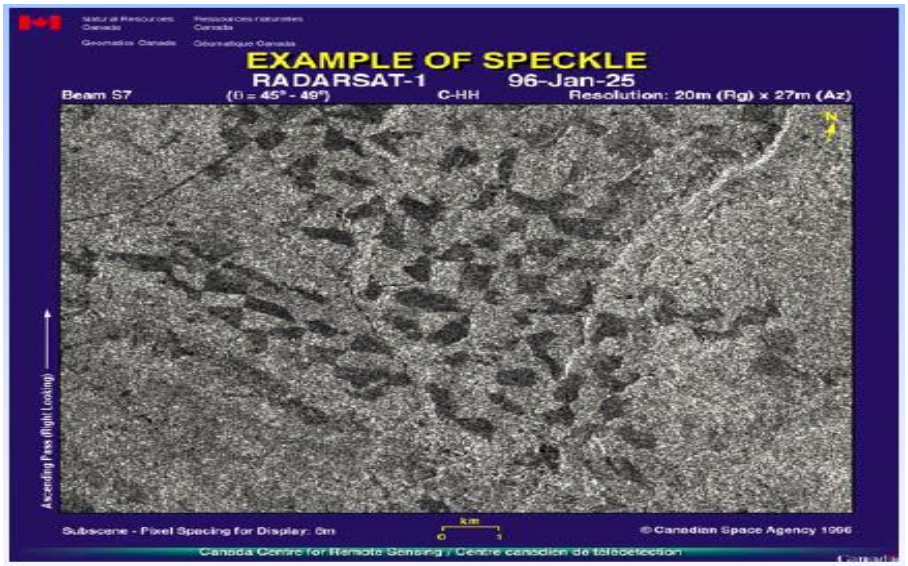

Figure 2.4: Speckle in a radar image **(**CCRS, 2013).

2.3 Sentinel 1 RADAR in agriculture

Sentinel 1 RADAR is used for crop type identification, crop condition monitoring, soil moisture measurement, and soil tillage and crop residue identification (Inglada *et al.,* 2016). This help to assess land use, predict harvests, monitor seasonal changes and assist in implementing a policy for sustainable development (Navarro *et al.,* 2016; Torbick *et al.,* 2017). Sentinel 1 RADAR will also be used for monitoring the changes of agricultural production and productivity of pastures caused by drought and monitoring the decline of land productivity and soil degradation due to excessive cultivation and pasturage and improper irrigation (Navarro *et al.,* 2016). Agricultural maps enable provision of independent and objective estimates of the extent of cultivation in a given country or growing season, which can be used to support efforts to ensure food security in vulnerable areas.

2.3.1 Rice growth phase

The temporal aspect of rice development is important to the understanding of the radar responses of rice fields at different growth phase. The rice plant usually takes 3-6 months from germination to maturity, depending on the variety and the environment under which it is grown (Nguyen Lam-Dao, 2009). The growth of rice plants is divided into three phases (Nguyen *et al.,* 2015).

The first phase is the vegetative phase which is characterized by the development of tillers and more leaves, and a gradual increase in plant growth. The number of days for vegetative phase varies depending on the variety of rice crop but is typically between 55 and 85 days begins with germination and ends with panicle initiation (Nguyen *et al.,* 2015).

The reproductive phase is a bulging of the leaf stem that conceals the developing panicle, called the 'booting' stage. Rice is said to be at the 'heading' stage when the panicle is fully visible.

Flowering begins a day after heading has completed. The reproductive phase lasts approximately 45 days among all varieties. The last phase is ripening phase starts at flowering and ends when the rain is mature and ready to be harvested. This stage usually takes 30 days. Grain filling occurs as nutrients and water are transported from one part of the plant to another; the process is affected by the availability of water and nutrients, and by temperature (Nguyen *et al.*, 2015).

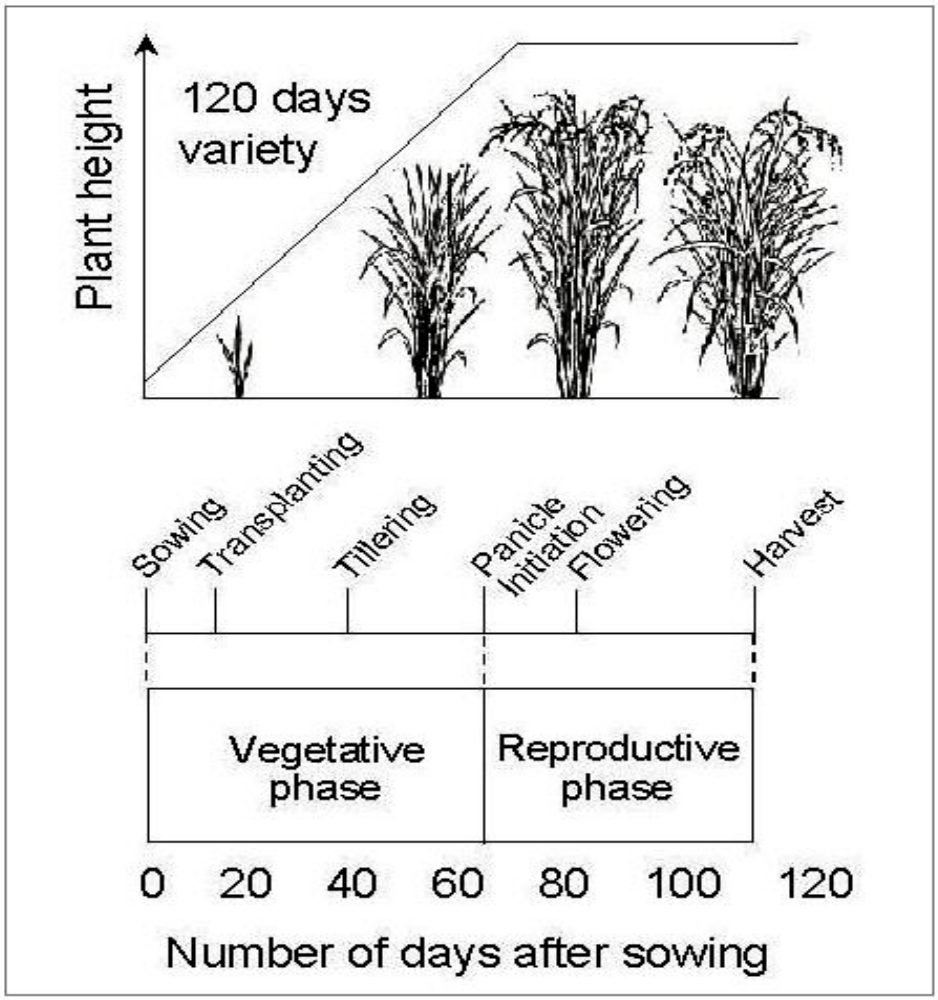

Figure 2.5: Rice growth phases (Nguyen Lam-Dao, 2009)

2.3.2 Sentinel 1 Radar for Rice monitoring

Several studies have been carried out on rice mapping and monitoring since the launch of the first European remote sensing satellite (ERS-1) in 1991, driven by earlier successes of using airborne SAR (Le-Toan *et al.*, 1989) and ground-based scatterometer data. Satellites with a shorter revisit time (e.g., six days at the Equator for the Sentinel-1 constellation can be applied for more frequent observation of a certain area) can be used to better identify the different growth cycle stages that are often imperceptible when using more sporadic data (Navarro *et al.*, 2016). The studies reported results, most of them based on C-band (frequency = 5.3 GHz, wavelength = 5.6 cm) SAR data. Basically, two common methods of SAR-based rice monitoring have been

implemented in multiple study areas using different SAR sensors (Nguyen *et al.*, 2015; Nguyen and Wagner, 2017). Method selection for SAR-based rice mapping and monitoring is essentially determined by the data availability and sensor selection.

2.3.3 Rice backscatter analysis

Sentinel 1 RADAR image is usually presented as a grey scale, with the intensity of each pixel representing the amount of energy returned from that area on the ground (Al-Ali and Mohamed, 2011). An analysis of multi-temporal Sentinel 1 RADAR data was performed to investigate the backscatter behavior of rice crop of the study area using single and dual polarized Sentinel 1 RADAR data. Rice crops typically exhibit a temporally varying backscatter signal due to their phenological interaction with the microwave signal (Nguyen *et al.*, 2015; Nguyen and Wagner, 2017). Several studies have detailed rice backscatter responses for varying wavelengths, polarizations, incidence angles and field properties (Inoue *et al.*, 2014). Rice paddies are inundated prior to the emergence of the crop due to sowing or transplanting, which results in a low radar backscatter response. As rice crops grow and gain in biomass from tilling, pinnacle formation, and flowering, the backscatter response increases proportionally with more interaction from double-bounce and direct volume scattering mechanisms until crops head. After ripening and near harvest, paddies are usually drained if still flooded or decrease in saturation and moisture due to mature haulm and leaf area which causes a shift toward a leveling off or decline in backscatter (Inoue *et al.*, 2014). Thus, using dense time series data tuned to these rice life cycle stages is essential to mapping rice attributes and field conditions. A phenologically sensitive, thresholding approach was applied to identify rice paddy area (Inoue *et al.*, 2014; Torbick *et al.*, 2017).

2.4 CART (Classification and Regression Tree)

The CART decision tree is a binary recursive partitioning procedure capable of processing continuous and nominal attributes as targets and predictors. Data are handled in their raw form; no binning is required or recommended. A CART tree is a binary decision tree that is constructed by splitting a node into two child nodes repeatedly, beginning with the root node that contains the whole learning sample (Batterham *et al.*, 2009). The CART is a recently used data mining methods with the objective of creating a model that predicts the value of a target (or dependent variable) based on the values of several inputs (or independent variables) (Li *et al.*, 2012; Shao and Lunetta, 2012). The three main elements of the CART (and any decision tree algorithm) are:

- Rules for splitting data at a node based on the value of one variable;
- Stopping rules for deciding when a branch is terminal and can be split no more; and

- Finally, a prediction for the target variable in each terminal node

The algorithm is non-parametric and can efficiently deal with large, complicated datasets without imposing a complicated parametric structure (Li *et al.*, 2012). When the sample size is large enough, study data can be divided into training and validation datasets. Using the training dataset to build a decision tree model and a validation dataset to decide on the appropriate tree size needed to achieve the optimal final model. The model is validated through test sample cross-validation, misclassification error, and costs (Batterham *et al.*, 2009).

2.4.1 Decision tree Image Classification

The idea of using decision trees to identify and classify objects was first reported by (Hunt *et al.*, 1996). Decision tree classification algorithms have significant potential for solving some of land-cover mapping problems and have not been tested in detail by the remote sensing community relative to more conventional pattern recognition techniques such as maximum likelihood classification. The decision tree classifier performs multistage classifications by using a series of binary decisions to place pixels into classes. Each decision divides the pixels into a set of images into two classes based on an expression (Kontgis *et al.*, 2015; Mansaray *et al.*, 2017; Nguyen and Wagner,2017). A decision tree classification method is independent of data probability distributions (Mansaray *et al.*, 2017). The decision tree classifier produced consistently higher classification accuracies than ISODATA and maximum likelihood classifier (Kontgis *et al.*, 2015). This research study used decision tree image classification method for Sentinel 2 optical and time series single and dual polarized Sentinel 1 RADAR data.

2.5 Sentinel 2 Optical data.

The European Space Agency (ESA) launched a new optical fine spatial resolution satellite, , namely Sentinel-2A, on 23 June 2015. Sentinel-2A can provide systematic global acquisitions of fine spatial resolution multispectral images with a fine revisit frequency, which is important for the next generation of operational products, such as land cover maps, land cover change detection maps and geophysical variables (Immitzer *et al.*, 2016). The Sentinel-2A images would surely be of great significance for regional water bodies' mapping, due to its appealing properties (i.e., the 10-m spatial resolution for four bands and the 10-day revisit frequency) and the free access (Yun *et al.*, 2016). The Sentinel-2A multispectral image has 13 bands in total, in which four bands (blue, green, red and NIR) have a spatial resolution of 10 m and six bands (including SWIR band) have a spatial resolution of 20 m. The MNDWI (Modified Normalized Difference Water Index) method can be applied to extract water bodies from the Sentinel-2A images since the green and SWIR bands are included. However, it is noticed that the spatial resolutions of green and SWIR bands are at 10 m and 20 m, respectively. An alternative and advisable way to

enhance the performance of water bodies' mapping using the Sentinel-2A imagery is to produce MNDWI at the 10-m resolution by downscaling the SWIR band (Band 11) from 20 m to 10 m (Yun *et al.,* 2016). Spatial interpolation and image fusion (e.g., pan-sharpening are the two most popular kinds of methods applied to increase the spatial resolution of remote sensing imagery (Vivone *et al.,* 2015). Pan-sharpening is widely applied to remote sensing images that have coarse multispectral bands and a fine spatial resolution. In order to produce the 10-m MNDWI from Sentinel-2A, only the spatial resolution of the SWIR band needs to be increased. Therefore, the 10-m bands in the Sentinel-2A imagery can be treated as PAN-like bands, and they can provide important fine spatial resolution information to downscale the 20-m bands to 10 m. 10-m MNDWIs can be used to extract more accurate water body maps than 10-m NDWI and 20-m MNDWI (Yun *et al.,* 2016). Optical indices like NDVI has been widely applied in monitoring various vegetation cover and is frequently used as a proxy of plant growth and productivity, as the amount of solar radiation reflected by the vegetation canopy is related to wavelength, chlorophyll, leaf interior tissues and plant water content (Dorigo *et al.,* 2012). In this research study, MNDWI and NDVI are integrated with time series Sentinel 1 RADAR images to map rice and the other land cover.

2.6 Integrating Sentinel 1 RADAR and Sentinel 2 optical data for land-cover mapping

With the ever-increasing number of satellites and the availability of free data, the integration of multi-sensor images in coherent time series offers new opportunities for land-cover and crop type classification (McNairn *et al.,* 2009; Waldner *et al.,* 2015; Inglada *et al.,* 2016). Radar and optical remote sensing data deliver complementary information; hence land-cover classification tasks can take advantage of the fusion of both data types leading generally to increase mapping accuracy. Many studies have combined optical and microwave images to improve mapping accuracy in agricultural scenarios (Blaes *et al.,* 2005; McNairn *et al.,* 2009). SAR data are independent of solar illumination and depend on the wavelength and on the roughness, geometry and material contents of the targeted surface. In contrast, optical data are greatly influenced by cloud cover and represent the reflectance of solar energy from a target area. The repeatability of observations on a cyclic basis and the availability of high spatial resolution multispectral data are particularly suitable for cost-effectively mapping crops and other land use with satisfactory accuracy (D'Urso *et al.,* 2010). Sentinel-2A and its relevant derivative indices (i.e., MNDWI and NDVI) have spectral bands sensitive to rice paddy conditions (Torbick and Salas, 2014). Multi-sensor data integration for mapping broad land use land-cover classes across a diverse landscape at moderate resolution is important (Ban, 2003; Michael *et al.,* 2005). Fusing optical and microwave spectral regions provided very high overall accuracy and kappa outcomes over a large

geographic region (Torbick and Salas, 2014; Skakun *et al.,* 2015). Phenological approaches applied to time series Sentinel 1 RADAR data allow for monitoring of rice agriculture with relevant information on the extent, inundation, crop calendar, and intensity (Torbick and Salas, 2014).

CHAPTER THREE

3. Materials and Methodology

3.1 Description of the Study Area

3.1.1 Location

Fogera wereda is one of the 151 weredas of the Amhara Regional State. It is found in South Gondar Zone of Amhara Regional State. It has 25 rural kebeles and 2 urban Kebeles. Fogera wereda lies to the south-eastern shore of Lake Tana on the road from Bahir Dar to Gondar, which is 625 km from Addis Ababa and 55 km north of the Regional capital Bahir Dar City. Fogera is bordered to the south by Misrak Este wereda, south-west by Dera wereda, west by Lake Tana, north by Libo Kemkem wereda, east by Farata wereda and northeast by Ebinat wereda. Geographically, it is bounded by latitude 11º38'41"–12º0'37"N and longitude 37º 31'28"–38º 0'29"E, covering a total area of 1,111.42 km² (Figure 3.1).

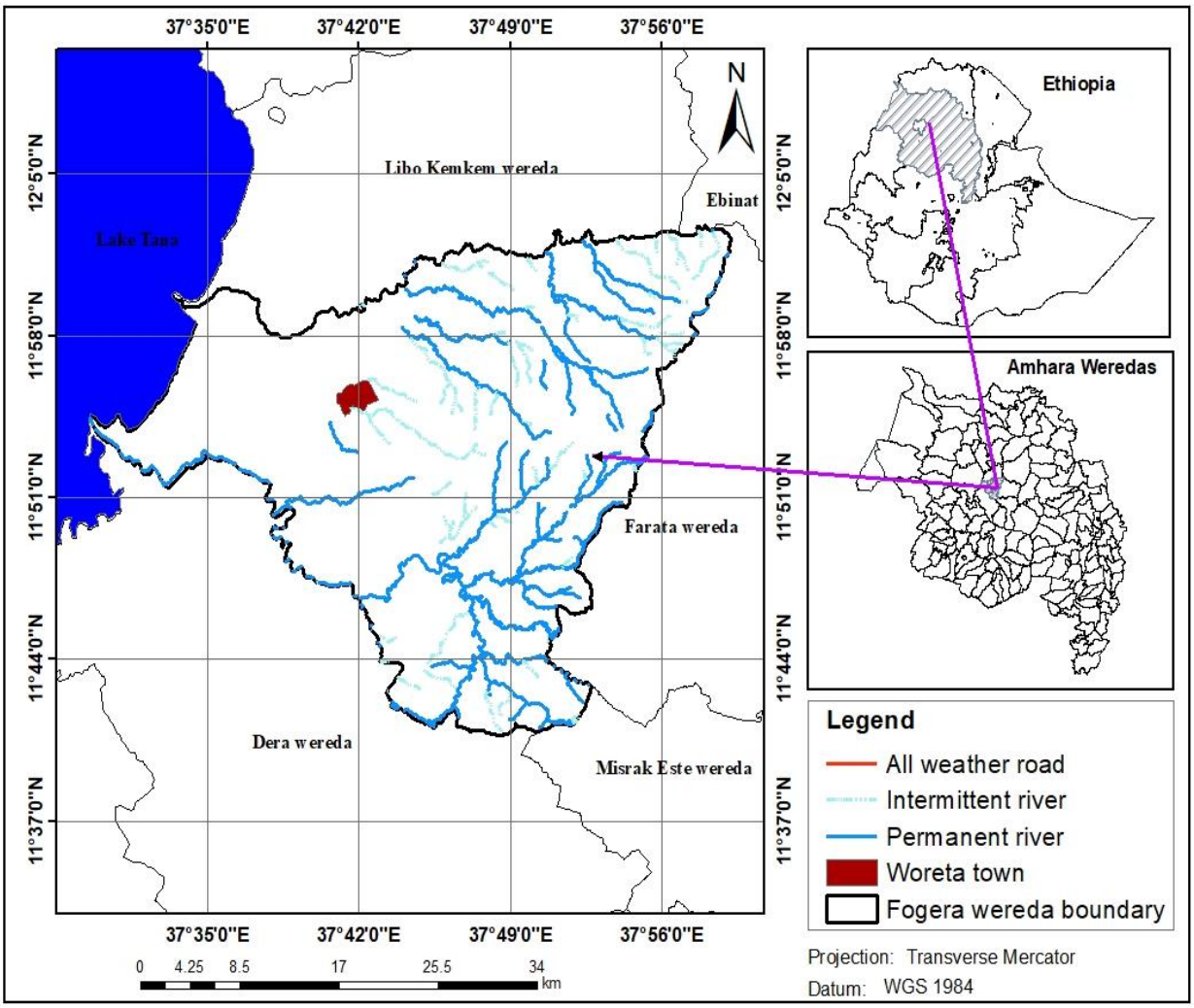

Figure 3.1: Location map of the study area (Fogera wereda).

3.1.2 Population

According to the Ethiopian Central Statistical Agency (CSA, 2007), the total population of Fogera wereda was 228,449. The 2014-2017 population projection (Table 3.1.) shows, the wereda's population in both sex increases by ~2%.

Table 3.1 population projection of Fogera wereda.

Year	Male	Female	Total
2014	134,511	130,001	264,512
2015	136,950	132,400	269,350
2016	139,355	134,704	274,059
2017	141,716	136,963	278,679

3.1.3 Topography

The study area has a very flat topography, which is known by the Fogera plain, adjacent to the eastern coast of Lake Tana. However, proceeding to the eastward, there is a rugged topography (Figure 3.2). Altitude ranges from 1774 to 2494 meters above mean sea level (m.a.s.l). The wereda consists mainly of flat land (76%), while mountains and hills and valley bottoms account for 11% and 13%, respectively (Tilahun *et al.*, 2012).

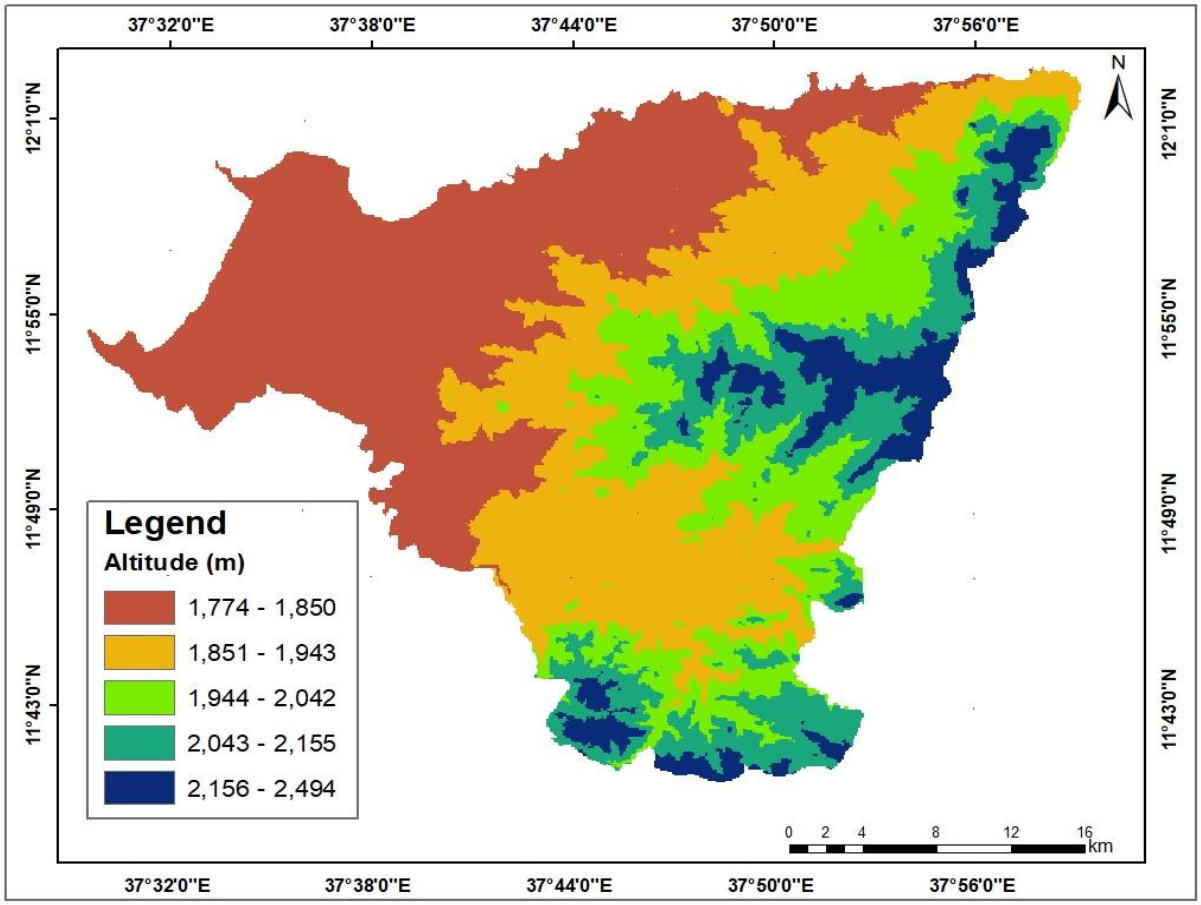

Figure 3.2: Topographic map of the study area.

3.1.4 Climate

According to the National Metrological Agency (NMA), the rainfall of the wereda is characterized by a Unimodal distribution with a peak in July. The mean annual rainfall was 1216 mm ranging from 1103 to 1336 mm from both the short (March and April) and long rains (June to September). The mean monthly values vary between 0.6 mm (January) and 415.8 mm (July), which indicate the poor temporal distribution of rainfall. In-situ monthly precipitation data for two rainfall stations have been collected for the years 2006-2017 from National Meteorology Agency of Ethiopia. Rainfall data for the year 2017 for Woreta station was not found. According to the rainfall records of these two stations, the June-December encompass rice sowing to harvesting season. Whereas in the year 2015 extreme peak rainfall values were recorded in Woreta station (Figure 3.3). Water supply and availability is also an important factor in determining the distribution of rice production. The water supply to a particular rice field is largely determined by rainfall, evaporation, and permeability (Yun *et al.*, 2001).

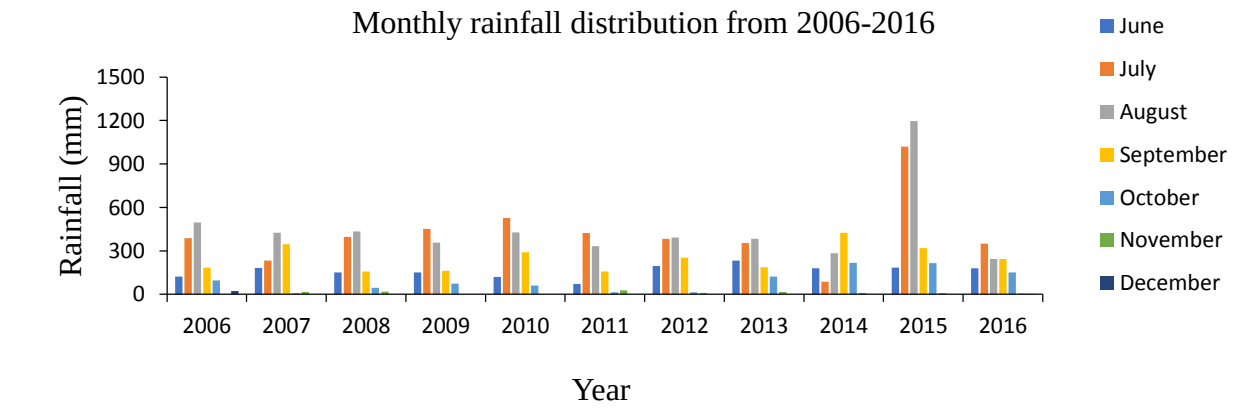

RF station of Woreta

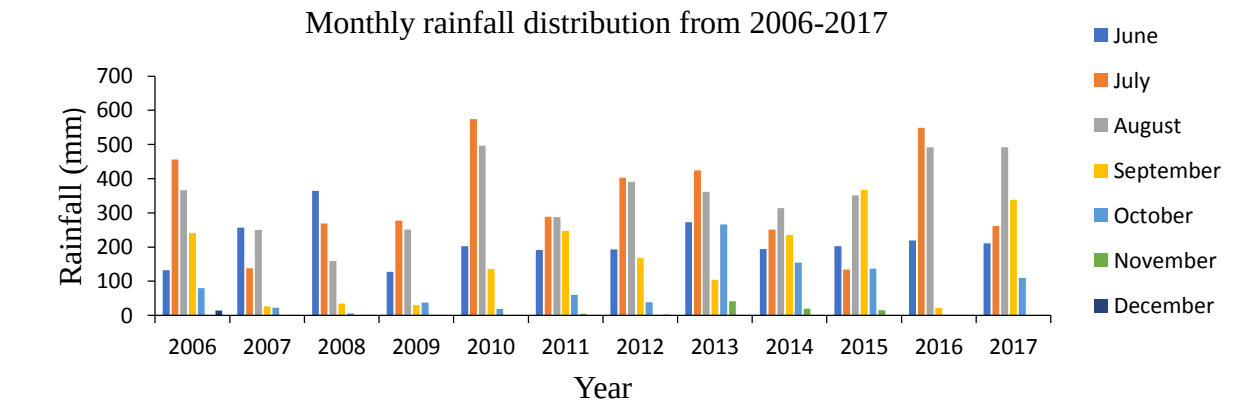

RF station of Amed ber

Figure 3.3: Rainfall (in mm) distribution of the study area.

The mean monthly temperature of the area is about 19 ºC, the monthly mean maximum temperature is about 27.3ºC, the monthly mean minimum temperature is 11.5 ºC, the Diurnal range of temperature is higher (16.7 ºC) at Woreta compared to that of Amed ber (14.9 ºC). The annual average maximum and a minimum temperature of the two stations from 2006-2016 (Figure 3.4).

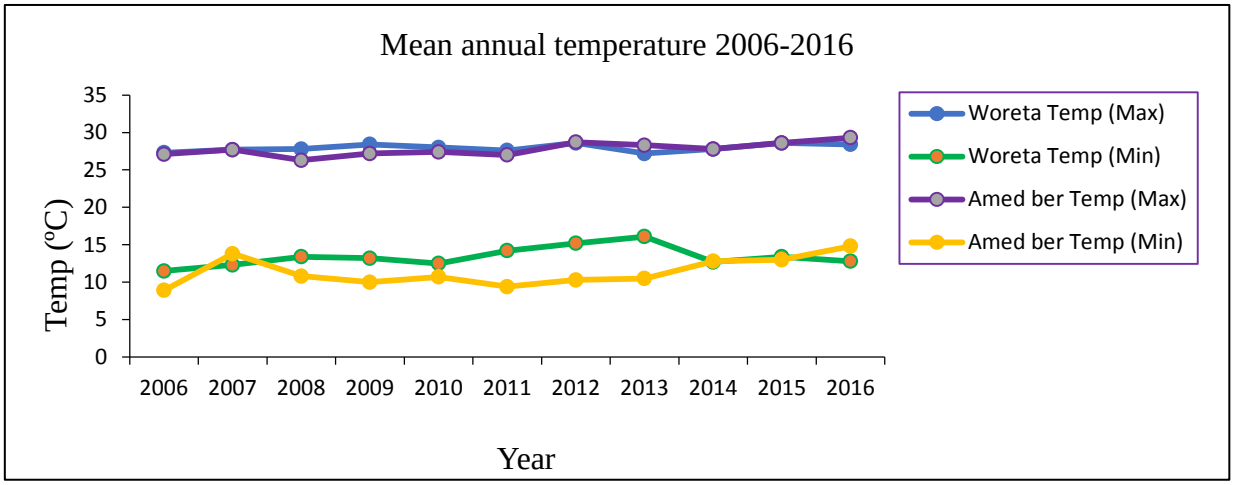

Figure 3.4: Temperature (in ºC) distribution of the study area.

3. 1.5 Soils

Rice plants prefer soil with good water-holding capacity, fertility, permeability, and a middle pH value (Yun *et al.*, 2001). Sandy or clay soil is usually most suitable. The major soil types in Fogera wereda exhibit a general relationship with altitude and slopes. According to the soil data from a geological survey of Ethiopia (2010), the study area has 9 major soil types (Figure 3.5). The dominant soil type is Haplic xerosols which cover 36.34% of the soil in the area. It is about 40,555.2 ha area followed by Chromic vertisols that account 30,548.9 ha area (Table 3.2). The soil type with the least area coverage is Leptosols that covers only 72.9 ha (0.01%).

Table 3.2 Major soil type area coverage and proportion.

Soil Type	Area(ha)	Proportion (%)
Haplic xerosols	40555.2	36.34
Chromic vertisols	30548.9	27.53
Eutric nitisols	14545.1	12.99
Calcic xerosols	11099.4	10.01
Orthic luvisols	7166.4	6.43
Orthic solonchaks	4852.7	4.44
Eutric regosols	2167	2.12
Dystric nitisols	132.8	0.13

Leptosols	72.9	0.01
Total	**111140.4**	**100**

Haplic xerosols and Chromic vertisols are the dominant types of soils in the wereda, particularly the lowland flat plains, valley bottoms and river terraces (Figure 3.5). Texturally, these soils are sandy clay and sandy loam respectively. The soil type and its permeability play a very crucial role in rice production. The rate of rainfall infiltration can also be affected by soil texture, a commonly used indicator of soil permeability.

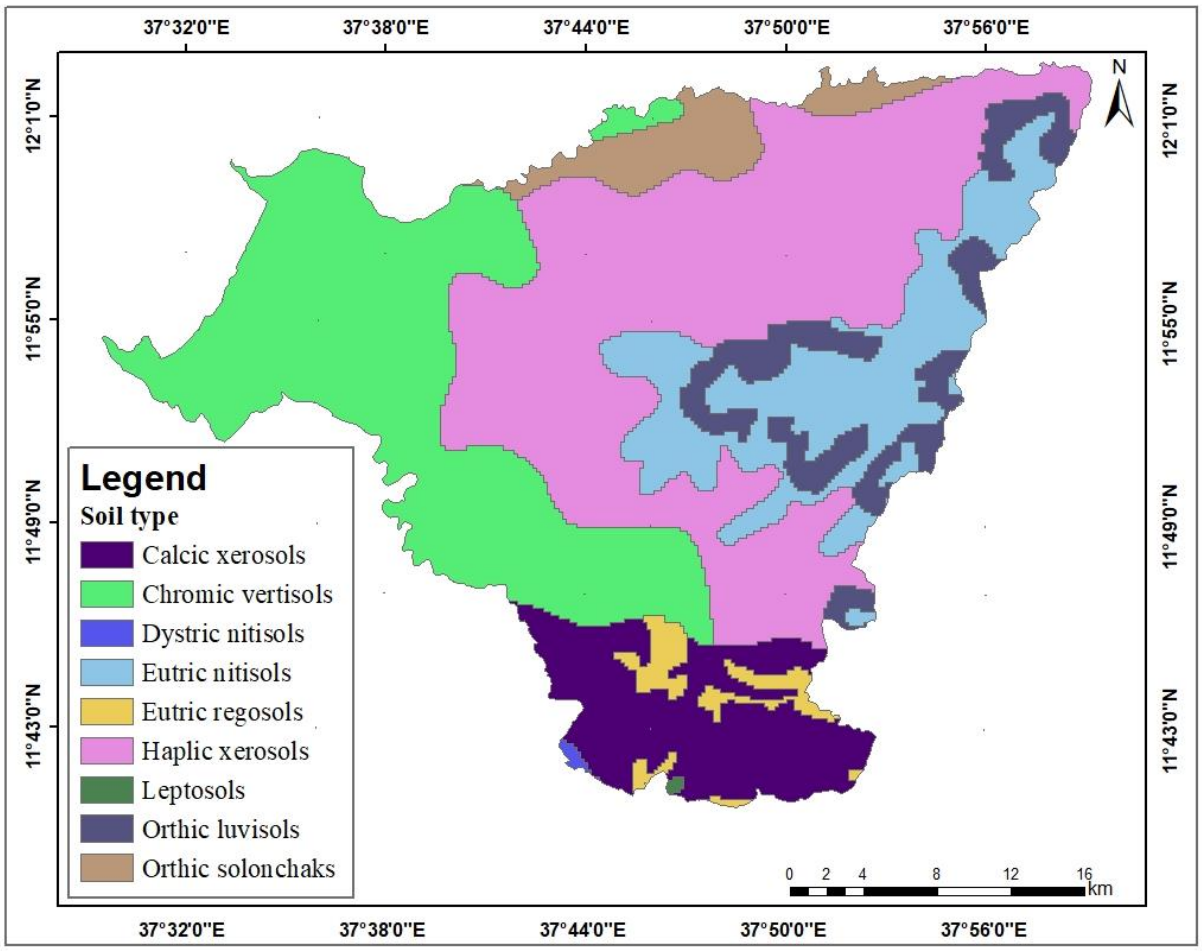

Figure 3.5: Soil type map of the study area (FAO, 2007).

3.1.6 Ecology

Fogera wereda, based on the agro-ecological classification method (altitude and rainfall), is classified into Moist Weyena Dega and Wet Weyena Dega zones (Astewul Takele, 2010). The Moist Weyena Dega accounts 4,845,459 ha (43.6 %) and Wet Weyena Dega accounts 6,267,856 ha (56.4 %) land of the wereda. Rice grows in specific ecological conditions and geographic regions (Yun *et al.*, 2000).

3.1.7 Agriculture

The farming system in the north and western section of the wereda, encompassing the area known as the Fogera plains, and which gets flooded during the rainy season, is mainly rice, fish, horticulture, and livestock (Astewel Takele, 2010). The farming system in the south and eastern section, which varies from lowlands to highlands is cereals, oil crops, horticulture, livestock, and apiculture. Cattle-farming is still a major activity, but crop cultivation has become increasingly important. What makes Fogera unique from other weredas is that it grows rice within Fogera Plain and also recognized for the unique Fogera Cattle breed.

3.1.8 Rice Calendar

The Crop Calendar is a tool that provides timely information about seeds to promote local crop production. It contains information on planting, sowing and harvesting periods of locally adapted crops in specific agro-ecological zones (FAO, 2013). The main rice sowing season in Fogera is between June to July, grows until September, and is mostly harvested during November with some kebeles trailing into December harvests (Table 3.3). The vast majority of rice is produced during the main wet season in Fogera wereda.

Table 3.3 FAO Ethiopia rice crop calendar.

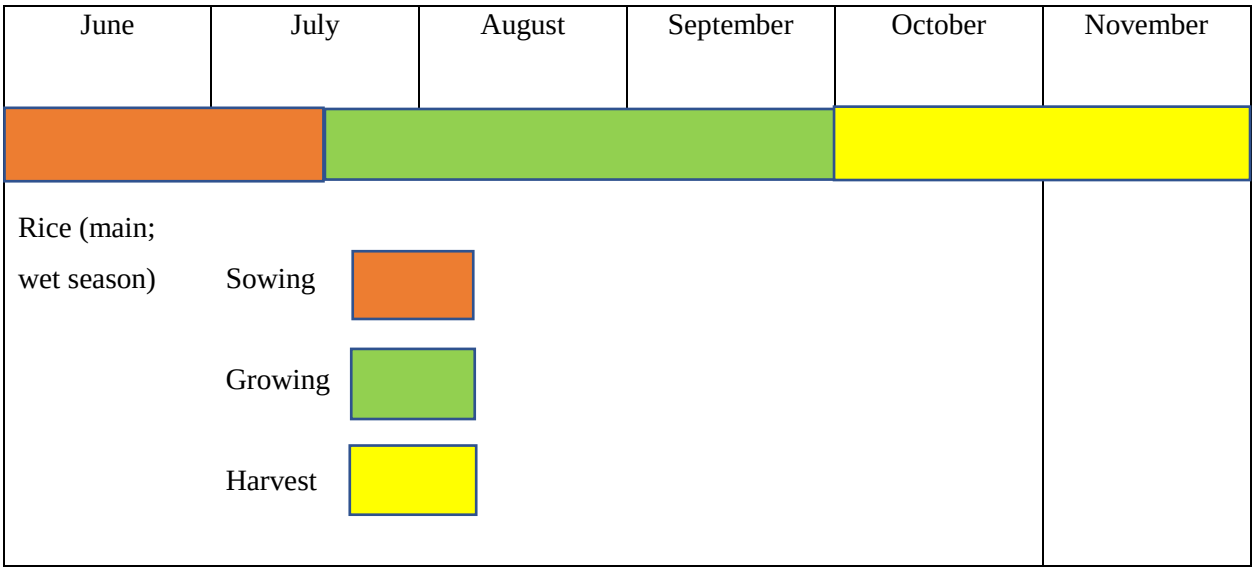

3.2 Materials

3.2.1 Data Description

Sentinel 1 RADAR data

Sentinel-1 collects data in four modes, namely Strip Map (SM), Interferometric Wide Swath (IW), Wide (EW) and Wave Mode (WM), with varying resolutions, extents, incidence angles and polarizations. Of these four acquisition modes of Sentinel-1A, the IW mode is regarded as the primary or default operational mode over land, supporting agriculture, forestry and other natural

resource applications (Skolnik, 2008). Hence, the IW mode is selected in this study to map and monitor rice fields in Fogera wereda, Ethiopia. This mode observes in single and dual polarization VV; VH (vertical transmitting, vertical receiving; vertical transmitting, horizontal receiving) with a 250 km footprint in the range direction. All data are freely available from the ESA Data Hub and mirrored at the Alaska Satellite Facility (ASF). Data were obtained as Standard Archive Format for Europe (SAFE), which contains general product information in XML, for the entire region using the open access data archives. Annotated data sets hold metadata on the main characteristics including acquisition, image properties, polarization, Doppler information, swath merging, calibration, and geographic location (Torbick *et al.*, 2017). SAFE products were obtained as Ground Range Detected (GRD), which have already been focused, multi-looked, calibrated and projected in ground range.

Table 3.4 Sentinel 1 RADAR product specification (ESA Sentinel-1 User Handbook, 2013).

Mode	Incidence Angle	Resolution	Swath Width	Polarization
Strip Map	20 - 45	5 x 5 m	80 km	HH+HV, VH+VV, HH, VV
IWS	29 - 46	5 x 20 m	250 km	HH+HV, VH+VV, HH, VV
Extra Wide Swath	19 - 47	20 x 40 m	400 km	HH+HV, VH+VV, HH, VV
Wave Mode	22 - 38	5 x 5 m	20 x 20 km	HH, VV

In this study, six Sentinel1 RADAR GRD images in IW mode is used during the 2017 rice growing season in Fogera wereda. These images span from the flooding/transplanting stage to the heading/milking stage of paddy rice, a period at which changes in temporal backscatter of the rice crop are most diagnostic. The acquired images are both in the single and dual polarization of vertical transmitted and vertically received (VV), and vertically transmitted and horizontally received (VH) channels. They are in a range and azimuth resolution of 5 m and 20 m, respectively.

Table 3.5 Characteristics of Sentinel 1 RADAR level 1 GRD IW products used in this study.

Date	PD	RON	AT	Polarization
14 June 2017	Descending	152	Normal	VV VH
20 July 2017	Descending	152	Normal	VV VH
1 August 2017	Descending	152	Normal	VV VH
25 August 2017	Descending	152	Normal	VV VH
30 September 2017	Descending	152	Normal	VV VH
12 October 2017	Descending	152	Normal	VV VH

PD, RON, and AT are pass direction, relative orbit number, and acquisition type, respectively.

Sentinel 2 Data

Optical remote sensor images, particularly the multispectral images, are important for calculating NDVI and MNDWI to map rice fields. The European Space Agency (ESA) launched a new optical Sentinel-2A, on 23 June 2015. Sentinel-2A optical images are freely available to the user community and can be downloaded at https://scihub.copernicus.eu/dhus/#/home. Sentinel-2A multispectral image has 13 bands in total, in which four bands (blue, green, red and NIR) have a spatial resolution of 10 m and six bands (including SWIR band) have a spatial resolution of 20 m.

Table 3.6 Band spatial resolution, central wavelength, and bandwidth of the Sentinel-2A image.

Band Number	Spatial Resolution (m)	Central Wavelength (nm)	Bandwidth (nm)
B1	60	443	20
B2	10	490	65
B3	10	560	35
B4	10	665	30
B5	20	705	15
B6	20	740	15
B7	20	783	20
B8	10	842	115
B8A	20	865	20
B9	60	945	20
B10	60	1375	30
B11	20	1610	90
B12	20	2190	180

Due to persistent cloudy weather conditions in the study area during the rice growing season, only a single cloud masked Sentinel-2A image acquired on 09 October 2017 was used in this study.

3.2.2 Tools and software programs used

Tools

In order to achieve the objectives of this study, the following software was utilized:

Software: The software packages used for this study were:

SNAP (Sentinels Application Platform, http:/step.easa.int/main/download/) provided by ESA was used for preprocessing and Sentinel 1 RADAR image backscatter statistics analysis.

IMPACT toolbox: This software was used to preprocess Sentinel-2A optical image.

Geomatica 2017: Geomatica 2017 was used for Sentinel-2A optical cloud masking for extraction of the cloud-free satellite image.

ERDAS Imagine 2015: This was used for image post-processing including layer stacking, Sentinel 1 RADAR image profile backscatter extraction, and accuracy assessment.

CART (Classification and Regression Tree): This software was used to develop a model for Sentinel 1 RADAR image classification and accuracy assessment.

ENVI 5.1: Software used for A decision tree image classification algorithm.

ArcGIS 10.5: ArcGIS 10.5 was used for the preparation of map document, compile and edit GIS datasets and display and analyze spatial data in both vector and raster format.

Microsoft Office Package (2013): Provides the necessary environment for MS Excel, MS Word, MS Powerpoint and MS Access.

3.3 Methodology

The methodology applied in this study includes acquisition of satellite images, preprocessing, backscatter coefficient extraction, identification of optimal polarization, CART model for Sentinel 1 RADAR image classification and accuracy assessment, integrating optical and radar images to map rice, mapping inundation and accuracy assessment as shown in Figure 3.6 the general workflow of the thesis.

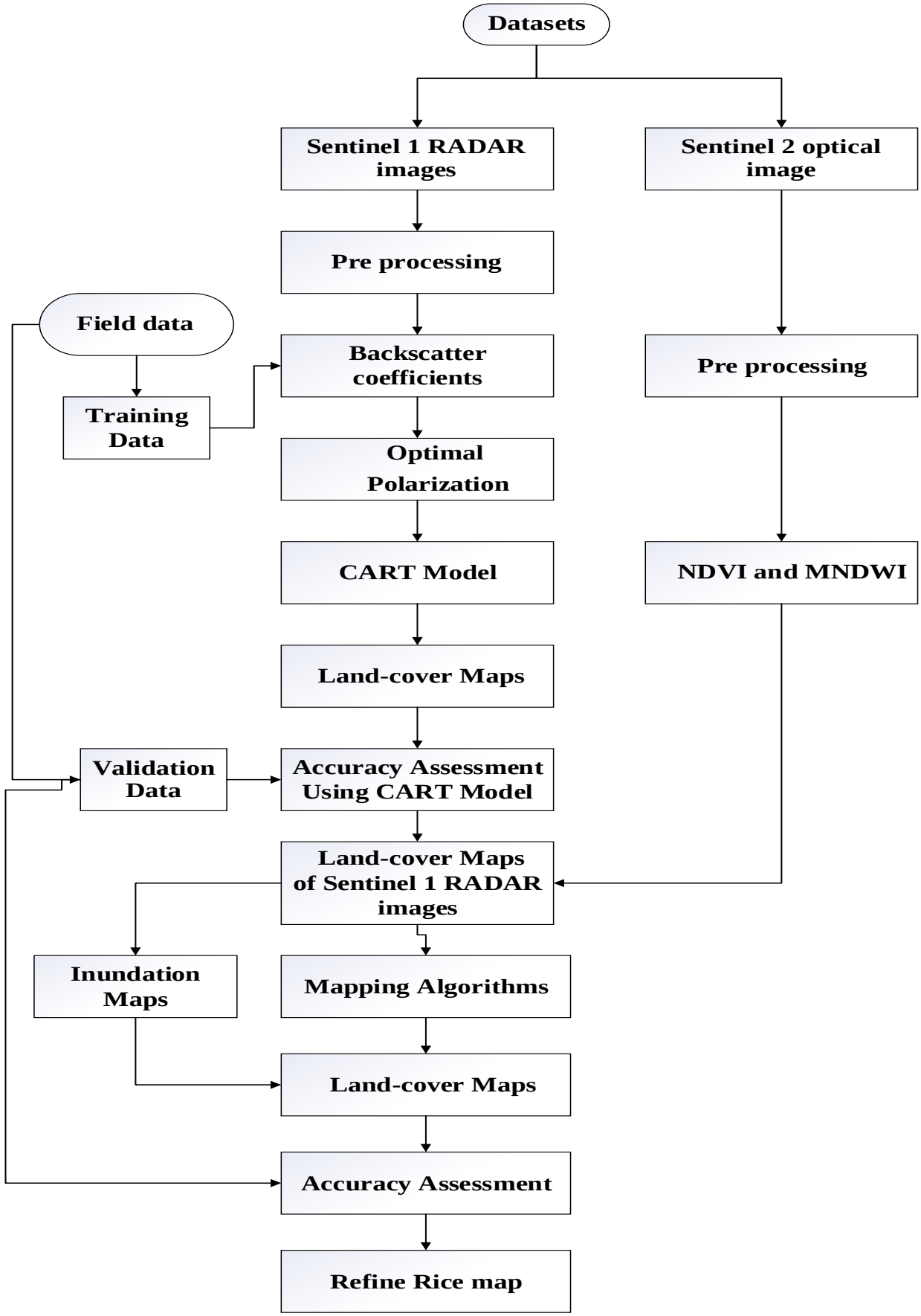

Figure 3.6: General workflow of the thesis

3.3.1 Image pre-processing

3.3.1.1 Sentinel 1 RADAR Radiometric Calibration

Sentinel 1 RADAR SAR images of VV/VH polarizations was first calibrated to sigma naught (σ^0) to provide imagery in which the pixel values can be directly related to the radar backscatter of the scene. Therefore, it is necessary to apply the radiometric correction to SAR images by which the pixel values of the SAR images truly represent the radar backscatter of the reflecting surface. The data calibration compensates for the radiometric influences of different incidence angles- caused by the sensor geometry and topographic characteristics of the surface (Martinis and Rieke, 2015). The radiometric correction is also necessary for the comparison of SAR images acquired with different sensors or acquired from the same sensor but at different times, in different modes, or processed by different processors. For converting digital pixel values to radiometrically calibrated backscatter, all the required information can be found in the product metadata. A calibration vector is included as an annotation in the product allowing simple conversion of image intensity values into sigma or gamma nought values. The Sentinel 1 RADAR GRD product was radiometrically calibrated using SNAP toolbox automatically with the following equation:

$$\sigma^0 = \frac{DN^2}{A\sigma^2} \quad (3.1)$$

Where:

DN: is the pixel digital Number of GRD pixel amplitude directly taken from the measurement file

A: is the value of sigma nought (σ^0)

3.3.1.2 Sentinel 1 RADAR Terrain Correction

Due to topographical variations of a scene and the tilt of the satellite sensor, distances can be distorted in the SAR images. Image data not directly at the sensor's Nadir location have some distortion. Terrain corrections are intended to compensate for these distortions so that the geometric representation of the image will be as close as possible to the real world. The calibrated Sentinel 1 RADAR images were then automatically terrain corrected using range-Doppler terrain correction to produce 10 m square pixel resolution images using Universal Transverse Mercator (UTM) zone 37 N (Mansaray *et al.*, 2017).

3.3.1.3 Sentinel 1 RADAR Speckle Filter

Speckle is a signal-dependent noise which is natural to any images obtained by coherent radiation, including SAR. Unlike optical remote sensing images which are characterized by very

neat and uniform features, SAR images are affected by speckle (Babu *et al*., 2013). It is a granular disturbance, usually modeled as a multiplicative noise that affects SAR images and all coherent images (Argenti *et al*., 2013). It reduces the readability and decreases the usefulness of the images for both human and automatic interpretation (Dekker, 1997). Speckles are caused by random constructive and destructive interference of the de-phased but coherent return waves scattered by the elementary scatters within each resolution cell. Speckle filtering is a preprocessing step that is applied to each temporal or time series Sentinel 1 RADAR images. The speckle filtering suppresses the noise that eases the better backscatter analysis and thus, it turns out to be a critical pre-processing step for detection or classification optimization. In this study speckle filtering using a 7 ×7 gamma map filter with 3 look techniques was applied (Wu *et al.*, 2011; Mansaray *et al.*, 2017).

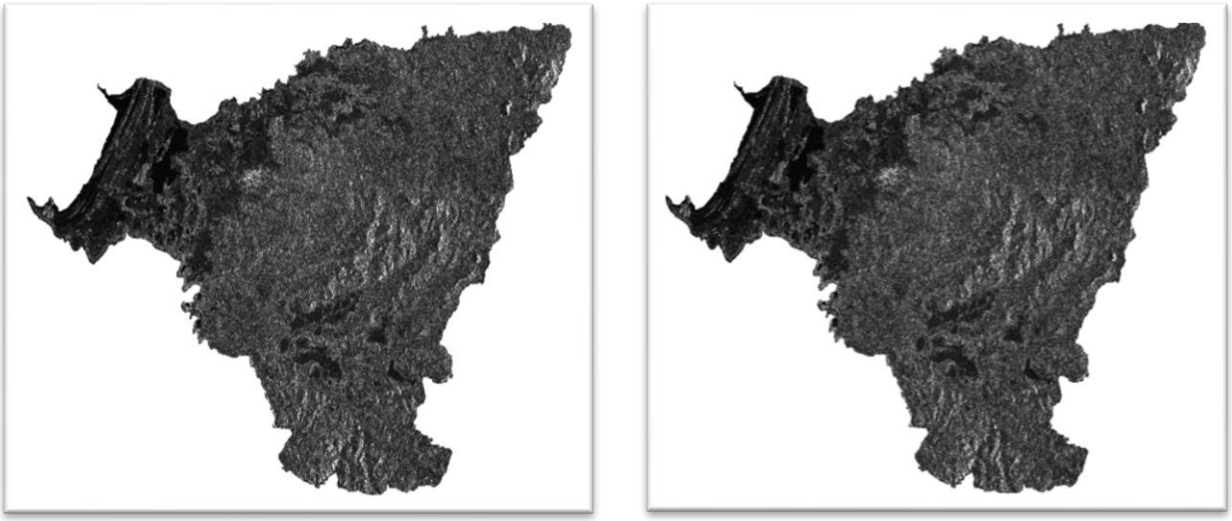

(a) (b)

Figure 3.7: (a) represented a terrain corrected Sentinel 1 RADAR image, b) represented a 7 ×7 gamma map speckle filter Sentinel 1 RADAR image.

3.3.1.4 Linear to decibel conversion

Synthetic aperture radar image is usually presented as a grey scale, with the intensity of each pixel representing the amount of energy returned (Backscatter) from that area on the ground. Backscatter is usually expressed in decibel (backscattering coefficient). Each Sentinel 1 RADAR (both VV and VH) linear to decibel conversion was applied using the formula below.

σ° (dB) = 10*log10σ° (energy ratio), whereby;

$$\text{Energy Ratio} = \frac{\text{Received energy from the sensor}}{\text{Energy reflected in an isotropic way}} \quad (3.2)$$

The backscattered coefficient can be a positive number if there is a focusing of backscattered energy towards the radar or the backscattered coefficient can be a negative number if there is a focusing of backscattered energy away from the radar (Bartsch *et al.*, 2012). Backscatter coefficient (σ°) in decibels (dB) represents target backscattering area (radar cross-section) per unit ground area. Because it can vary by several orders of magnitude, it is converted to dB as 10*log10σ°. This scattering behavior depends on the physical characteristics of the terrain, primarily the geometry of the terrain elements and their electromagnetic characteristics (Bartsch *et al.*, 2012).

3.3.1.5 Sentinel 1 RADAR Image Co-registration

The essential step for image stacking to remove the geometric difference between time series images is co-registration (Getu Tessema, 2017). The Sentinel 1 RADAR input images for stacking must belong to the same coordinate system and as it is important to obtain a high-quality radar data, individual images need to be co-registered. For interferometric processing, two or more images must be registered into a stack. One image is selected as the master and the other images are the slaves (Mansaray *et al.*, 2017). The pixels in slave images will be moved to align with the master image to sub-pixel accuracy. Co-registration ensures that each ground target contributes to the same (range, azimuth) pixel in both the master and the slave image. In this research study 14 June, 2017 Sentinel 1 RADAR image (both VV and VH) is used as a master image to co-registered the other RADAR images (Figure 3.8). The registration is fully automatic with cross-correlation operator in the sentinel application platform (SNAP) SAR co-registration available tools.

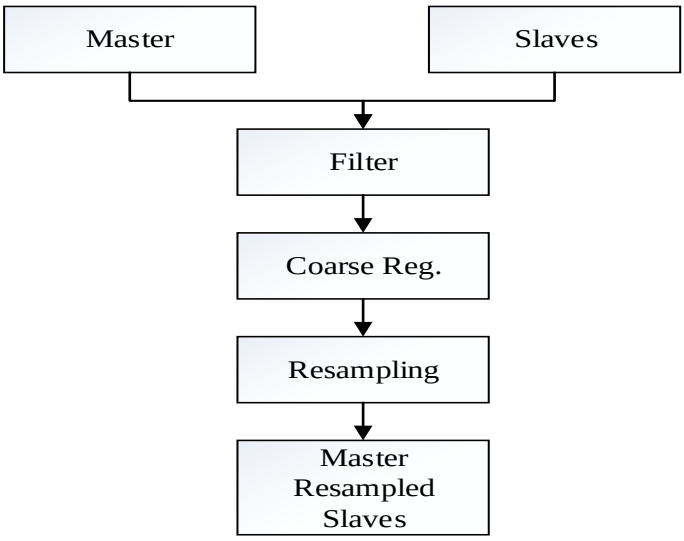

Figure 3.8: Flowchart for Sentinel 1 RADAR image co-registration.

Figure 3.8 shows five original Sentinel 1 RADAR image- slaves (for both VV and VH) was re-projected with respect to the other Sentinel 1 RADAR image- master.

3.3.1.6 Sentinel 1 RADAR Image Stacking

For the analysis and production of statistical parameters or backscatter properties, image stacking is compulsory. It involves the combination of more than one co-registered images. The Sentinel 1 RADAR image stack is a component of co-registration. The create stack operator (CSO) collocates the master and slave images based into a single reference (master) geometry. Basically, the slave image data is subset into geometry of the master image. With performing this operation, the master and slave images share the same geo-positioning information and have the similar dimensions.

3.3.1.7 Sentinel-2 optical image pre-processing

The dataset used in this study is the standard sentinel -2 level -1C product, which was produced by radiometric and geometric corrections, including ortho-rectification and spatial registration on a global reference system with sub-pixel accuracy. The Sentinel-2 Level-1C product is composed of 100 km × 100 km tiles in the UTM/WGS84 projection and provides the Top-Of-Atmosphere (TOA) reflectance. One scene of the Sentinel-2 Level-1C image acquired on 09 October 2017 was downloaded from the ESA Sentinel-2 Pre-Operations Hub (https://scihub.copernicus.eu/). A Sentinel-2 Level-1C zipped (.zip) archives data was pre-processed and converted into a single Geo Tiff, TOA-Reflectance file using IMPACT tool v1.3b. The bands used [B03, B04, B08, B11, B12] corresponding to Sentinel-2 [G, R, NIR, SWIR1, SWIR2] and the output resolution selected is set as “highest” (among selected bands) while staking together bands of different resolution to pan sharp the image to 10 m spatial resolution. The output radiometric resolution will be converted into Byte (8 bit) by using a linear transformation.

TOA RefByte = (DN*0.0255) (3.3)

Image DN values [0-4095] are converted to TOA Reflectance [0,1] using the provided conversion factor (10000) and multiplied by 255 to obtain a byte TOAReflectance [0,255]. The cloud-contaminated portions of 09 October image are removed using Geomatica 2017 software, and then the information of missing data is reconstructed using the 29 October images. The approach is based on the patch-based information reconstruction strategy with the global optimization process.

3.3.2 Field data

Field data collection was conducted from September 5 to September 15, 2017, to obtain training and validation datasets. Figure 3.9 shows photos taken during the 2017 field campaigns

(a)

(b)

(c)

(d)

Figure 3.9: Spatial dynamics of rice cultivation in the study area: (a) and (c) field showing rice at high flooding condition in September 2017, (b) and (d) field showing rice at maturity in September 2017.

Based on the field data collected, the wereda land-cover classification was divided into six broad classes: these are rice, non-rice crops, water, built up, trees and others. Rice refers to paddy rice fields, non -rice crops includes wheat, sorghum, maize, teff, horticulture etc., water includes rivers, lakes, streams, and ponds, built up includes residential and commercial houses, trees include plants with considerable height and density, and others include roads, bare land surfaces, grassland, other low biomass species, and in the final map could include any or a combination of the other classes due to misclassification. This broad classification scheme was adopted to help in identification of optimal polarization (VV/VH) of Sentinel 1 RADAR images in addition to the major focus of his study rice field mapping and monitoring. In addition, the broad land-cover classes of non-rice crops, water, built up, trees and others have also been taken into consideration as their coexistence with rice fields could induce confusions and influence rice classification accuracy.

A total of 611 training and validation data were randomly collected from paddy rice field and other land-cover using a portable Garmin Global Positioning System (GPS) device, and an average horizontal accuracy of 3.0 m was recorded. For paddy rice field 93 training data was collected. The remaining 76 points were reserved for rice field accuracy assessment. Other land cover types (non-rice crops, water, built up and trees) account for a total of 226 training points which were collected and exported to Sentinel 1 RADAR data for the extraction of temporal backscatter profiles. Additionally, 52 points from non-nice crops, and 40,70 and 60 for water, built up and tree respectively was randomly selected for the purpose of map accuracy assessment of Sentinel 1 RADAR images. For map accuracy assessment of integrated Sentinel 1 RADAR and Sentinel 2 optical images, 50 validation points for the other classes were used to know confusions and influence of the class on rice classification accuracy.

The number of training data for rice increased intentionally as it forms the major focus of the study. The number of samples can also be adjusted based on the relative importance of categories within the objectives of the project or the inherent variability within each category. It may be useful to take fewer samples in categories that show little variability, such as water and increase the sampling in the categories that are more variable, such as built up and trees. More samples were collected for the rice class, as it is more variable over time, in addition to being the major focus of this study.

3.3.3 Backscatter Extraction

After pre-processing, the collected training points were overlaid on Sentinel 1 RADAR data for the extraction of temporal backscatter profile using ERDAS Imagine software. Then the average temporal backscatter profile was calculated for each land-cover type.

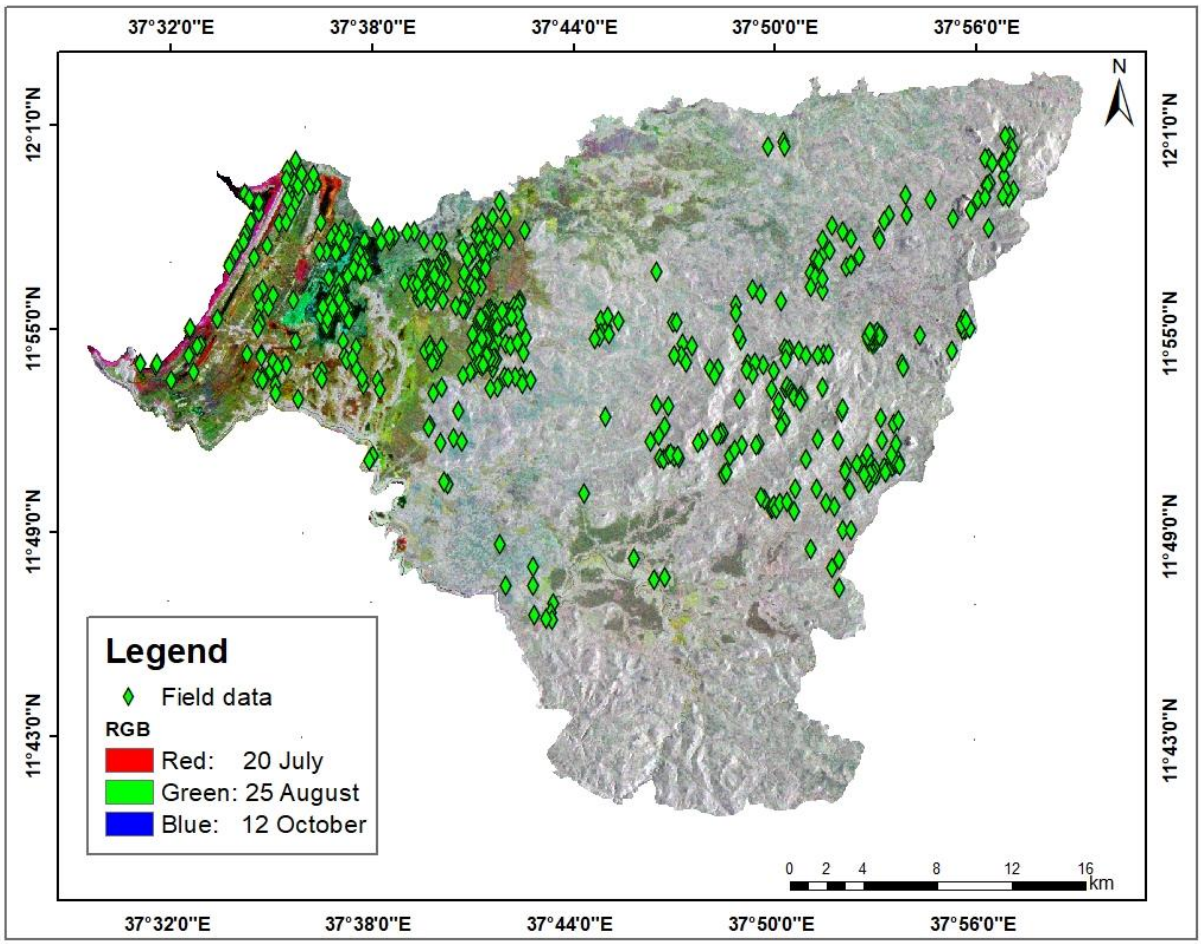

Figure 3.10: Field data Points used for training and validation of 2017.

3.3.4 Optimal polarization for mapping

As the Sentinel 1 RADAR data used in this study are in both single and dual polarization, proposing the most optimal polarization for mapping the targeted land-cover type is important in order to reduce data redundancy and dimensionality, as Sentinel 2 optical indices are also utilized.

Two criteria were considered in the selection of the optimal polarization. The first criterion is based on the temporal increase of paddy rice backscatter, whereas the second exploits a two-class separability measure. The optimal polarization is assumed to be the one which exhibits the most sustained increase in paddy rice backscatter, while at the same time producing the best results with the two-class separability measure. In other words, a polarization has to satisfy both conditions to be considered optimal or else both polarizations will be used as inputs in the decision tree classifier.

According to Choudhury and Chakraborty (2006) the concept of feature separability, two classes are said to be well separated if the distance between their respective class means is larger than that of their standard deviations. The separability criteria between classes a and b are measured by the Bahattacharrya distance as:

$$S_{ab} = \frac{|\mu_a - \mu_b|}{S_a + S_b} \quad (3.4)$$

where μ and S are the mean and standard deviation of the features to be separated, respectively.

The Bhattacharya distance is more theoretically sound because it is directly related to the upper bound of the probabilities of the classification errors (Choudhury and Chakraborty, 2006). It measures the real values between 0 and 2, where 0 indicates complete overlap between the signatures of the two classes and 2 indicates the complete separation between the two classes (Lin *et al.,* 2009). The larger the separability values among the class pairs, the better the final classification results (Wang *et al.,* 2010).

3.3.5 Classification and Regression Trees (CART)

The CART is more complex machine learning algorithms like support vector machine (SVM) and random forest (RF) classification algorithms (Mansaray *et al.,* 2017). After identification of optimal polarization, one of the actual work of this paper is to prepare Land Use Land Cover (LULC) map of the study area. A Classification and Regression Tree (CART) method were applied to generate the updated Land Use Land Cover (LULC) map using a stacked Sentinel 1 RADAR images. Classification and regression trees are intuitive methods, often described in graphical terms. A tree is typically shown growing upside down, beginning at its root. An observation passes down the tree through a series of splits, or nodes, at which a decision is made as to which direction to proceed based on the value of one of the explanatory variables. Ultimately, a terminal node or leaf is reached and predicted response is given. Trees partition the explanatory variables into a series of leaves that contain the most homogeneous collection of outcomes possible. Trees are typically fit via binary recursive partitioning. The term binary refers to the fact that the parent node will always be split into exactly two child nodes. The term recursive is used to indicate that each child node will, in turn, become a parent node, unless it is a terminal node. A single split is made using one explanatory variable. The variable and the location of the split are chosen to minimize the impurity of the node at that point. The CART has a number of advantages over many classification methods (Li *et al*., 2012).

The simplicity of results. The interpretation of results summarized in a tree is very simple. This simplicity is useful not only for purposes of rapid classification of new observations but can also

often yield a much simpler "model" for explaining why observations are classified or predicted in a particular manner.

Tree methods are nonparametric and nonlinear. The final results of using tree methods for classification or regression can be summarized in a series of (usually few) logical if-then conditions (tree nodes). Therefore, there is no implicit assumption that the underlying relationships between the predictor variables and the dependent variable are linear. The CART is not significantly impacted by outliers in the input variables. CART incorporates both testing with a test data set and cross-validation to assess the goodness of fit more accurately.

3.3.6 Identification of optimal node of Sentinel 1 RADAR images

The optimal tree (node) is defined as that tree in the pruned sequence that achieves minimum cost on test data. Because test misclassification cost measurement is subject to sampling error, uncertainty always remains regarding which tree in the pruning sequence is optimal (Batterham *et al*., 2009). Starting at the root node, CART evaluates all possible splits of all predictor variables and picks the “best” single split overall. The best split of the variable selected is better than the best split of any other predictor. The data are then partitioned according to that best split. The same process is applied to all subsequent nodes until all cases have been placed in a terminal node. Because the final partitions do not overlap, each case can only be in one terminal node. The “best” split is the one that reduces impurity the most (Li *et al*., 2012).

The collected data is sufficiently large, the CART model divided into two subsets randomly, namely, one for training (d) and other for testing (t) , where $d \cap t = \phi$. The tree is grown on the training data. Then, using the test set, error rates are calculated for the full tree as well as all smaller subtrees (i.e., trees having fewer terminal nodes than the full tree). Error rates for classification trees are typically the overall misclassification rate, while for regression problems, mean squared error or mean absolute deviation from the median is the criteria used to rank trees of different size. The subtree with the smallest error rate based on the independent test set is then chosen as the optimal tree. The test and learning samples are formed by collecting two independent data sets. Table 3.7 shows the number and percentage of collected learn and test data.

Table 3.7 Sample partition table.

Sample Partition	No.	Pct.
Learn	319	52.21
Test	292	47.79
Total	611	100

No. and Pct. are the Number and Percentage, respectively of collected learn and test data of Sentinel 1 RADAR images.

CART divided the data of major land-cover types in to learn and test data. Table 3.8 shows the number and percentage of collected learn and test data.

Table 3.8 Target breakdown table.

Classes	Sample	No.	Pct.
Rice	Learn	93	55
	Test	76	45
	Total	169	100
Water	Learn	38	48.7
	Test	40	51.3
	Total	78	100
Built	Learn	70	50
	Test	70	50
	Total	140	100
Trees	Learn	66	52.4
	Test	60	47.6
	Total	126	100
Non-Rice crops	Learn	52	53.1
	Test	46	46.9
	Total	98	100

No. and Pct. are the Number and Percentage, respectively of collected major land-cover type learn and test data from Sentinel 1 RADAR VH images.

3.3.7 Root Competitor Splits

The second basic step in the CART is to select the splits on the predictor variables that are used to predict membership in classes of the categorical dependent variables. The split at each node will be found that will generate the greatest improvement in predictive accuracy. This is measured with some type of node impurity measure, which provides an indication of the relative homogeneity (the inverse of impurity) of cases in the terminal nodes. If all cases in each terminal node show identical values, then node impurity is minimal, homogeneity is maximal, and prediction is perfect. A competitive split is one that results in nearly as pure a node as the chosen split. At node *t*, the best split *s* is chosen to maximize a splitting criterion $\Delta i\ (s, t)$. When the impurity measure for a node can be defined, the splitting criterion corresponds to a decrease in impurity. In CART model this is mathematically expressed as

$\Delta i\ (s,\ t) = p(t)\Delta i\ (s,\ t)$ (3.5)

where $p(t)$ is the probability of a case in node t.

Table 3.9 Root Competitor Splits

Competitor	Split	Improvement	Imp. ratio	N Left	N Right
b4	-24.63475	0.16815	33		286
b5	-22.59975	0.16815	1.00000	33	286
b3	-46.30025	0.15082	0.89690	109	210
b6	-23.56275	0.14148	0.84140	30	289
b2	-24.24375	0.12286	0.73064	31	288
b1	-17.52055	0.08667	0.51542	177	142

3.3.8 Optimal node for Rice and the other land-cover mapping

Identification optimal nodes are important because target classes usually overlap (making it impossible to have a clear separation of one target group from the other), a search for optimal nodes usually results in an increased overall accuracy in the class of interest. Figure 3.11 shows the optimal nodes that separate rice and other land-cover types. To identify the optimal node, the collected data divided into 10 nodes based on 6-day imaging dates. Gini index was used in this research study to minimize node impurity. The Gini index impurity measure at a node t is defined as

$i(t) = \sum_{i,j} C(i/j)\ p\ (i/t)\ p(j/t)$ (3.6)

Where $C(i/j)$ is the cost of miss-classifying a class j case as a class i case and p(j/t) the probability of a case in class j given that it falls into node t.

The Gini splitting criterion is the decrease of impurity defined as

$\Delta i\ (s,\ t) = i(t) - P_L i\ (t_L) - P_R i\ (t_R)$ (3.7)

where P_L and P_R are probabilities of sending a case to the left child node t_L and to the right child node t_R respectively. They are estimated as

$P_{L\,=}\, P(t_L)/P(t)$ and $P_{R\,=\,P}(t_R)/P(t)$ (3.8)

Where $p(t)$ is the probability of a case in node t.

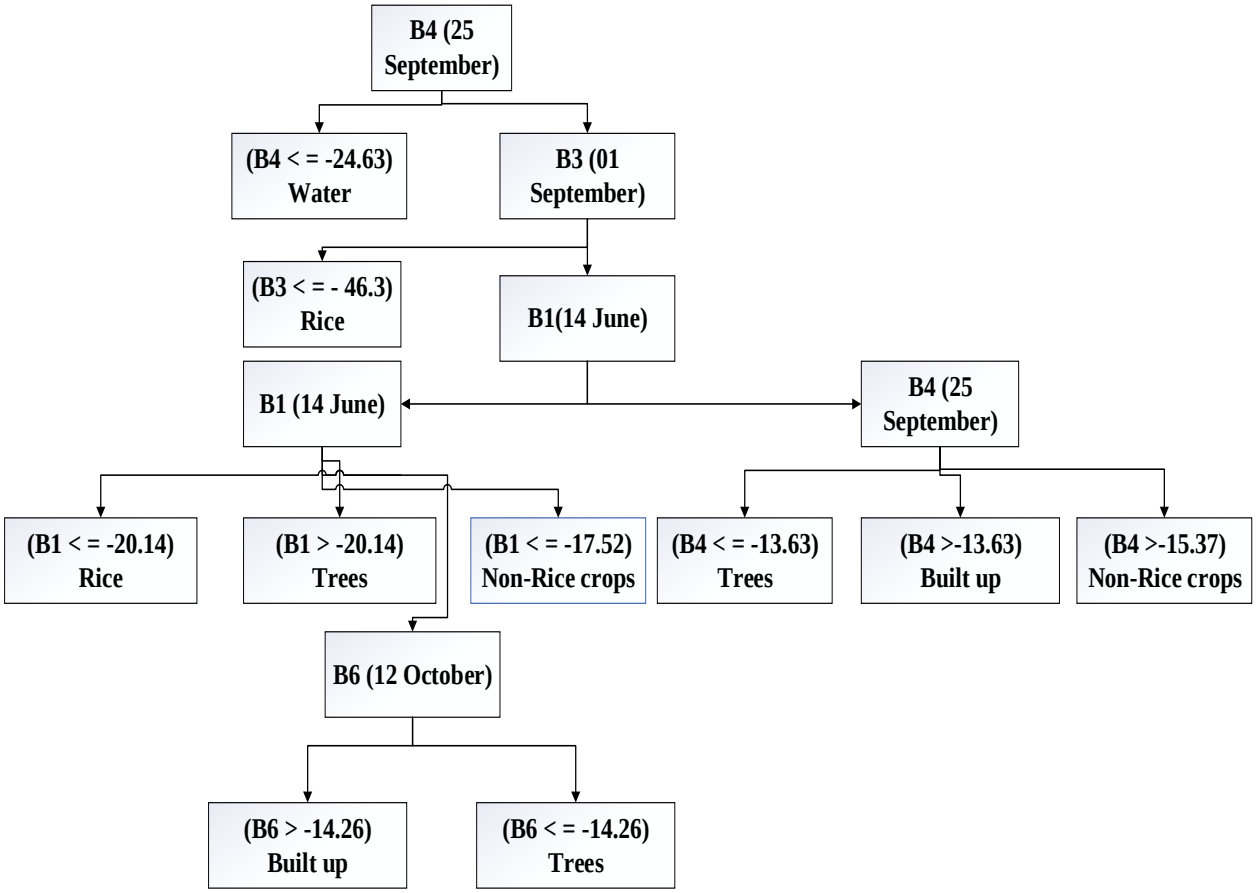

Figure 3.11: CART decision tree classifier based on multi-temporal VH training field points.

Based on Figure 3.11 the optimal node values identified for the mapping of rice are all pixels less than or equal to -20.14 dB b1 (14 June) and all pixels less than or equal to -46.3 dB b3 (01 August).

For the mapping of water, the identified optimal node values are all pixels less than or equal to -24.63 dB at 25 August dates of imaging (b4). For the mapping of built, all pixels greater than -13.63 dB b4 (25 August) and all pixels greater than -14.26 dB b6 (12 October) was identified. This class exhibited the highest temporal backscatter values due primarily to corner reflections from buildings and other vertical objects. For the mapping of trees, all pixels greater than -20.14 dB b1 (14 June), all pixels less than or equal to -15.37 dB b4 (25 August) and all pixels less than or equal to -14.26 dB b6 (12 October) were the optimal node values of this land use type. Trees exhibited the second highest backscatter. For the mapping of non-rice crops, all pixels less than or equal to -17.52 dB b1 (14 June) and all pixels greater than -15.37 dB b4 (25 August) were identified as optimal node values for non-rice crops. Finally, all pixels which do not meet the classification criteria outlined above, were classified as others, a class which as earlier mentioned, contains roads, barren, grasslands, and another low biomass species, and in the final

land-cover map, could include misclassified pixels from rice, water, built, trees and non-rice crops.

Finally, based on the optimal node threshold number a decision tree classification algorithm was applied in this study using ENVI 5.1 software. A decision tree employs tree-structured rules which recursively divide the initial input dataset into increasingly homogeneous subsets based on well-defined splitting criteria (Wang *et al.*, 2010). At each split or node, the values of each explanatory variable are examined and a particular threshold of a single variable that produces the largest reduction in a deviance measure is chosen to partition the data (Rogan *et al.*, 2003). Decision tree classifiers are advantageous in that they are less sensitive to nonlinearities in the input data than classification methods that require an assumption of Gaussian distributions. Results obtained from the CART model have validated automatically via accuracy assessment.

3.3.9 Variable Importance

Calculating variable importance is used to know which imaging date better separate rice from other land-cover types and to rank the six imaging date based on their separating importance. The variable importance of each six imaging date of Sentinel 1 RADAR data X_k is measured by ;

$$M(X_k) = \sum_{t \in T} \Delta i(\tilde{s_k}, t) \quad (3.9)$$

Where $\tilde{s_k}$ is a surrogate split on X_k for s^* , s^* is the best split of t into t_L and t_R

3.4 Accuracy assessment for Sentinel 1 RADAR images

3.4.1Test sample cross-validation

The first and most preferred type of cross-validation is the test sample cross-validation (Li *et al.*, 2012). This type of cross-validation, the tree is computed from the learning sample, and its predictive accuracy is tested by applying it to predict the class membership in the test sample. Test sample estimate was calculated as follows:

Divide L into L_1 and L_2. $N_2 = \neq L_2$. d derived from L_1 . Then

$$R^{ts}(d) = N_2^{-1} \sum_{L2} I(d(X_n) \neq j_n) \quad (3.10)$$

3.4.2 Misclassification error

The misclassification error is simply the proportion of observations in the node that are not members of the majority class in that node. T is the classification tree and $\tilde{T}\{T1, T2, \ldots, tL\}$ denote the set of all terminal nodes of T. The misclassification rate for T is estimated by,

$$R(T) = \sum_{\tilde{T}} R(T)P(t) = \sum_{i=1}^{j} R(T1)\, P(tL) \quad (3.11)$$

Where P(t) is the probability that an observation falls into node t.

3.4.3 Costs

If the costs for the test sample exceed the costs for the learning sample, then this is an indication of poor cross-validation (Li *et al*., 2012). a cost-complexity pruning measure for a tree T is defined as

$$R_\alpha(T) = \sum_{i=1}^{j} R_\alpha(T1) = R^{re}(T) + \alpha|\tilde{T}| \quad (3.12)$$

Where, $|\tilde{T}| = L$ is the number of terminal nodes in the subtree T. Which is a measure of tree complexity and α is the contribution to the measure for each terminal node. R^{re} is re substitution as the estimate of R(T).

3.5 Integrating optical indices with Sentinel 1 RADAR images

From Sentinel 2 optical cloud masked image normalized difference vegetation index (NDVI) and the modified normalized difference water index (MNDWI) were computed to integrate with the temporal Sentinel 1 RADAR images. NDVI has been widely applied in monitoring density and intensity of green vegetation growth using the spectral reflectivity of solar radiation. Green leaves commonly show better reflection in the near-infrared wavelength range than in visible wavelength ranges. When leaves are water stressed, diseased, or dead, they become more yellow and reflect significantly less in the near-infrared range (Mansaray *et al.*, 2017). Normalized Difference Vegetation Indices (NDVI) from the Sentinel 2 data was derived using the following well-known formula:

$$NDVI = \frac{b_{nir} - b_{red}}{b_{nir} + b_{red}} \quad (3.13)$$

where b_{nir} and b_{red} correspond to near-infrared and red spectral bands of Sentinel 2, respectively.

The modified normalized difference water index (MNDWI) which cannot only enhance information about water and restricting the one from vegetation and soil but can also significantly distinguish built-up features from water bodies (Mansaray *et al.*, 2017). MNDWI have been derived using the following equations:

$$MNDWI = \frac{b_{green} - b_{swir}}{b_{green} + b_{swir}} \quad (3.14)$$

where b_{green} and b_{swir} are the green and shortwave infrared bands, respectively.

In the current study, it is proposed that the integration of the aforementioned optical indices with temporal Sentinel 1 RADAR images could provide additional information that would improve overall classification accuracy. The six Sentinel 1 RADAR images from the optimal polarization and the NDVI and MNDWI images were finally layer stacked via bilinear interpolation to produce an 8-band dataset as follows: 14 June image (b1), 20 July Image (b2), 1 August image (b3), 25 August image (b4), 30 September image (b5), 12 October image(b6), 09 October NDVI image (b7) and 09 October MNDWI image (b8). Based on the temporal backscatter of the investigated land-cover classes at the optimal polarization (Figure 3.11) and the spatial distribution of NDVI and MNDWI values, a decision rule mapping algorithm is proposed and validated in this study.

3.5.1 Mapping Algorithm

The classification rule was based on expert knowledge of class signatures and data characteristics using the per-pixel information in each image, with its temporal behavior, and the corresponding temporal backscatter coefficients (dynamic range, minimum and maximum) and the single-date optical indices in each of the land-cover types (Mansaray *et al.*, 2017). NDVI threshold values of rice, trees, and non-rice crops were developed using CART model based on training data collected.

MNDWI and NDVI threshold values for water and built was adopted from (Mansaray *et al.*, 2017) to discriminate paddy rice fields from the other land-cover. All 8 images in the co-registered layer stack were used in the decision rule.

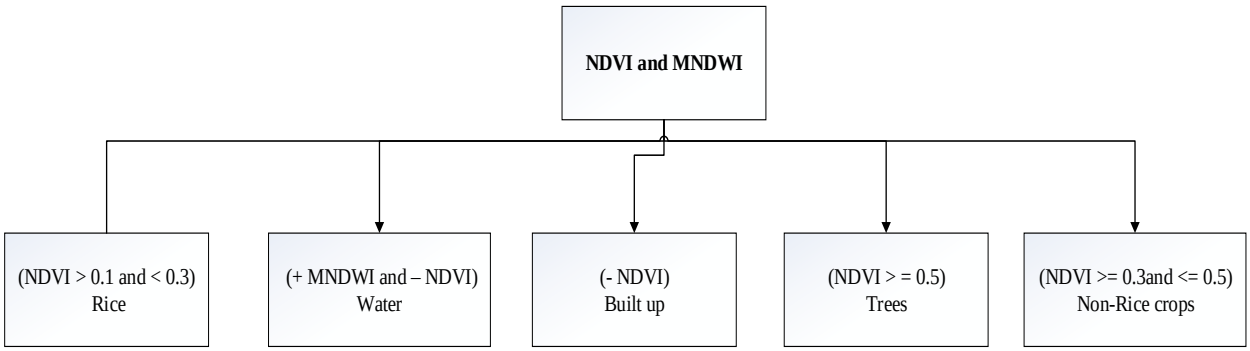

Figure 3.12: optical indices integrated with optimal Sentinel 1 RADAR images.

Figure 3.12 shows NDVI and MNDWI indices derived from a 09 October 2017 image integrated with optimal Sentinel 1 RADAR images shown in Figure 3.11.

Finally, all pixels which do not meet the classification criteria outlined in figure 3.12, were classified as others. Finally, a decision tree classification algorithm is implemented in this study using ENVI 5.1 software to map land-cover classes by integrating Sentinel 1 RADAR and Sentinel 2 optical indices. Results obtained from this algorithm were validated via accuracy tests.

Accuracy assessment

Accuracy assessment is a compulsory activity after any satellite image classification analysis to know whether or not the classification process met its objectives. Accuracy assessment is the degree of correspondence between observation and reality. It refers to assessing the accuracy level of the final categorical map generated by image classification. This can be done by generating a random set of points and comparing the land-cover map of the image with that of obtained in the field i.e. image map with reference data (Eastman, 2003). The most commonly applied methods of accuracy assessment include producer's accuracy, user's accuracy, overall accuracy and Kappa coefficient (Lu *et al.*, 2004). The formula provided here are adopted from Lo and Yeung (2005).

Producer's Accuracy: measures the percentage of correctly classified pixels from a sample data or indirectly indicates errors of omission for a particular class. It is calculated by dividing the number of correctly classified locations to the total number of samples in the reference data or column.

$$\text{Producer's Accuracy} = \left(\frac{C_i}{C_t}\right)100 \quad (3.15)$$

Where Ci = correctly classified sample locations of the reference data or column and Ct = total number of sample locations of the column.

User's Accuracy: measures the probability of each category classified on the map represented actually on the ground. It indirectly indicates the error of commission to a particular category. It is calculated as:

$$\text{User's Accuracy} = \left(\frac{R_i}{R_t}\right)100 \quad (3.16)$$

Where Ri = correctly classified samples in the row and Rt = total number of samples in the row.

Overall Accuracy: also known as Percent Correctly Classified (PCC) simply measures the overall accuracy of the data and calculated as the sum of the diagonal divided by the total number of samples (n). Hence, the formula is given as:

$$\text{Overall Accuracy(PCC)} = \left(\frac{Sd}{n}\right)100 \quad (3.17)$$

Where Sd = sum of values along diagonal and n = total number of sample. According to Lo and Yeung (2005), overall accuracy does not differentiate between errors of commission and errors of omission and overestimates the accuracy of the data due to various limitations.

Overall Kappa Statistics: is another measure of accuracy assessment that makes a better estimate than overall accuracy because it is capable of controlling the PCC index and incorporates off-diagonal values to calculate the coefficients. Kappa coefficient results are always less than 1 and result approaching 1 indicate excellent agreement between the classified map and reference data. It is calculated as:

$$K = \frac{N\sum_{i=1}^{r} x_{ii} - \sum_{i=1}^{r}\left(x_{i+} * x_{+i}\right)}{N^2 - \sum_{i=1}^{r}\left(x_{i+} * x_{+i}\right)} \text{ whereby;}$$

$$K = \frac{(\text{Total} * \text{sum of correct}) - \text{sum of the all the}(\text{Row total} * \text{Column total})}{\text{Total squared} - \text{sum of the all the}(\text{Row total} * \text{Column total})}$$

(3.18)

3.6 Mapping inundation

CART becomes an effective tool to separate water from other land-cover types using Sentinel 1 RADAR VH images. The CART was applied to identify the inundated area in an effort to develop hydroperiod map. Hydroperiod is the frequency, duration, and timing of inundation (Torbick *et al.,* 2017). These rice field characteristics can be used to help understand calendar and intensity patterns. Training data based on identified field conditions in imagery was used to develop CART model. Figure 3.13 shows Sentinel 1RADAR image data backscatter threshold during the rice growing season. The trend of agricultural areas transitioning to inundation is apparent, with backscatter values appearing as darker tones in the time series (Torbick *et al.,* 2017).

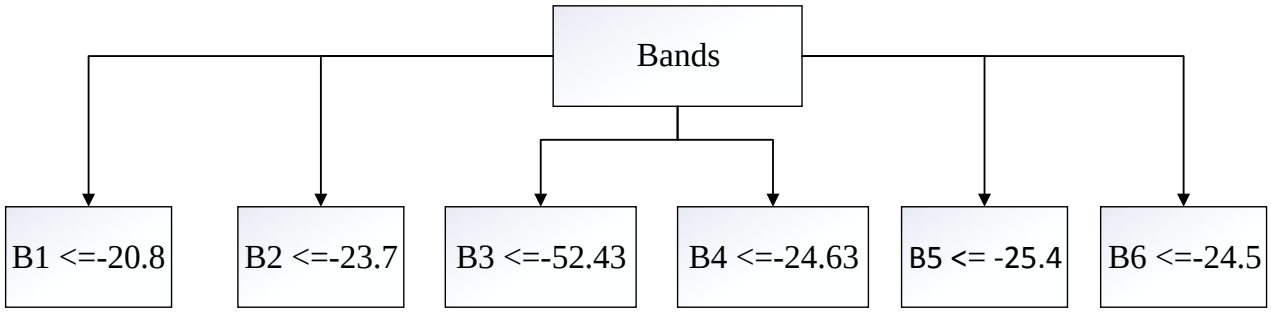

Figure 3.13: CART decision tree classifier based on multi-temporal Sentinel 1 RADAR training pixels.

Figure 3.13 shows the multi-temporal Sentinel 1 RADAR VH image optimal node identified using CART model for mapping inundated area. All pixels which do not meet the classification criteria outlined in figure 3.13 above, were classified as non-inundated area.

Finally, a decision tree classification algorithm is implemented in this study using ENVI 5.1 software to identify inundated area from the non-inundated area. Results obtained from this algorithm were validated via CART model testing methods.

CHAPTER FOUR

4.1 Results

4.1.1 Image interpretation

As rice grow, their radar backscattering characteristics also change. Thus, multi-temporal data can add useful information for identification purposes. In this study, the multi-temporal backscattering profiles of the five land-cover types are derived from the average radar backscattering coefficient of calibration data, which are located in the land use field centers. Figure 4.1 shows the stacked VV and VH images of the study area. Red, Green and Blue color codes represent 20 July, 25 August and 12 October 2017 Sentinel 1 RADAR images, respectively. 20 July weather condition was characterized by high rain and paddy field starts to inundate. 25 August was characterized by rainy weather and paddy rice field inundation increased. 12 October weather condition is characterized by low rainfall and inundation paddy field is highly decreased. This image date includes vegetative, reproductive and ripening rice growth stages. The color variation shows that there is a backscatter difference among different land-cover types. Rice has stronger signals at VV polarizations than that of VH polarization. It appears greenish and distinguishable from other land-cover types. The water surfaces areas were quite smooth at the times of image acquisition and appear as a dark tone on all of the images. The

bright signature of buildings on all the images is attributed to the high radar backscattering coefficients of building materials and corner reflection effects of constructions. The polarization signatures of different kinds of trees vary because it is affected by geometric properties and dielectric constants of the plants and underlayers. Non-rice crops backscatter values didn't show a pronounced difference with other land-cover types in the stacked image.

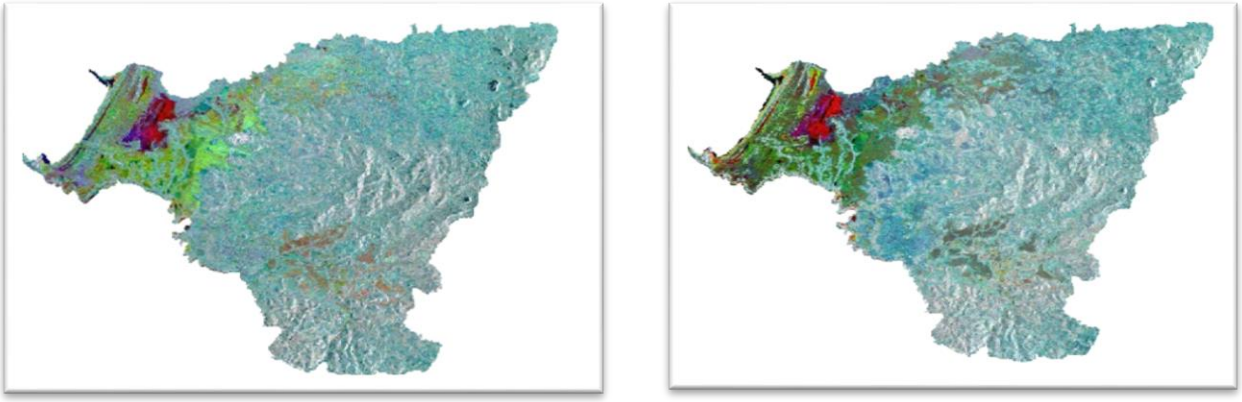

(VV) (VH)

Figure 4.1: The RGB image of VV and VH Sentinel 1 RADAR data 20 July, 25 August and 12 October 2017

At the beginning of the rice season (<25 days after sowing), i.e. the first half of the vegetative stage, flooded and non-flooded rice fields had low and high backscatter, respectively. During the period of 25-70 days, i.e. the second half of the vegetative stage and the reproductive stage, flooded and non-flooded fields had similar low and high backscatter response. In flooded fields, the plant-water double bounce interaction should be less dominant, thus the backscatter of flooded fields should be lower than that of drained fields. The temporal increase of Sentinel 1 RADAR backscatter at two consecutive data acquisition dates were recorded during the rice ripening stage (i.e. 30 September and 12 October VH imaging date). After the age of 70 days, i.e. the ripening stage, the growth (height and biomass) stopped and the leaves changed their orientation to be no more erectophile (i.e. their insertion angles were typically 30-40º) (Le-Toan *et al.,* 2003).

4.1.2 Optimal Polarization Images

4.1.2.1 Based on the temporal increase in paddy rice backscatter

In determining the optimal polarization based on the temporal increase in paddy rice backscatter, backscatter profiles of points were critically examined at both VV and VH polarizations. In any rice field, lowest backscatter profiles are recorded at the sowing and flooding stages of rice.

Table 4.1 shows the average temporal radar backscatter coefficients and their respective standard deviations at VV and VH polarizations for the rice class.

Table 4. 2 The average temporal backscatter coefficients for rice crop at VV and VH polarization.

	Rice VV		**Rice VH**	
Image	**μ**	**s**	**μ**	**s**
14 June 2017	-12.7	0.8	-20.3	1.3
20 July 2017	-11.1	3.3	-19.3	2.5
1 August 2017	-13.0	3.5	-49.0	3.0
25 August 2017	-10.5	3.0	-18.1	2.0
30September 2017	-11.0	2.6	-16.6	1.4
12October 2017	-11.0	2.6	-16.8	1.9

μ and s are the mean and standard deviation, respectively, of backscatter (dB) at corresponding date.

From Table 4.1, it can be observed that the temporal backscatter values at the VV polarization is higher than that at VH polarization at all imaging dates, in agreement with investigations done by (Nguyen *et al.*, 2015). However, the VH polarization shows the most consistent temporal increase in paddy rice backscatter apart from 01 August image date. The consistency is here defined as the number of time points at which an increase in backscatter is recorded. In almost all land-cover type, there is an increase in backscatter up to the second image date (20 July 2017), and there is a sharp decline on 1st of August 2017 at VH polarization due to high flooding condition. The VV polarization shows relatively linear backscatter value in all imaging dates. After 01 August 2017 imaging date, VH polarization shows an increase in backscatter. The VH polarization is to provide a better discrimination of rice from other land-cover types because temporal backscatter profiles are generally stable during the paddy rice growing season in the area under investigation. For both VV and VH polarizations, the curves of radar backscattering coefficient of rice on the different dates show a seasonal fluctuation ranging from -13.0 dB to -10.5 dB and -49.0 dB to -16.8 dB at VV and VH polarization, respectively. This indicates that rice has distinct life cycle variations at this timescale. The VH polarizations especially shows the backscatter variability of rice at different rice growth stage (Figure 4.2).

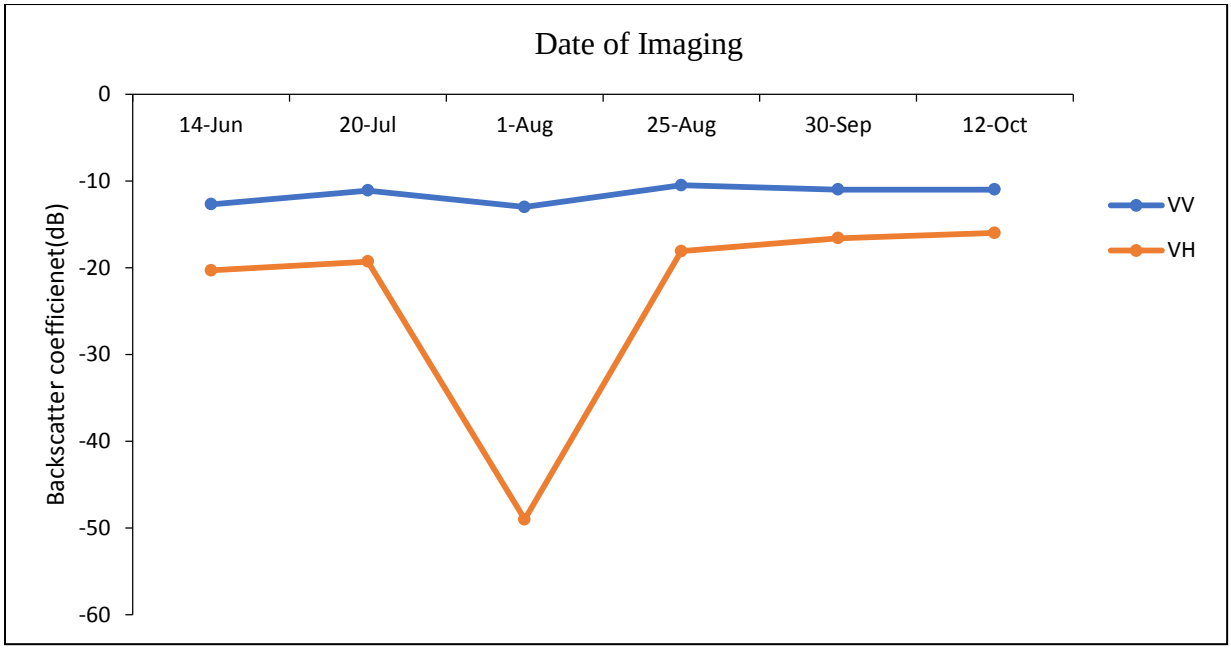

Figure 4.2: Temporal average backscatter profiles of rice class at both polarizations. Data points correspond to Sentinel 1 RADAR images of Fogera wereda acquired on 14 June, 20 July, 01 August,25 August, 30 September and 12 December in 2017, respectively

Table 4.2 Temporal average backscatter coefficients for other land-cover classes at VV polarization.

	Non-Rice crops		**Water**		**Built up**		**Trees**	
Image	**μ**	**s**	**μ**	**s**	**μ**	**s**	**μ**	**s**
14 June 2017	-11.8	1.6	-13.5	4.3	-9.9	3.0	-10.7	2.0
20 July 2017	-9.4	1.9	-17.9	5.2	-8.0	2.5	-9.8	2.0
1 August 2017	-10.0	2.0	-17.0	3.5	-7.8	3.4	-9.5	2.0
25 August 2017	-9.2	1.4	-19.0	5.7	-8.5	2.7	-10.0	2.0
30 September 2017	-10.7	2.3	-18.3	4.6	-9.2	2.8	-10.2	2.0
12 October 2017	-9.5	1.6	-18.8	5.1	-8.4	2.7	-9.9	2.0

μ and s are the mean and standard deviation, respectively, of backscatter (dB) at corresponding class and date.

Table 4.3 Temporal average backscatter coefficients for other land-cover classes at VH polarization.

	Non-Rice crops		**Water**		**Built up**		**Trees**	
Image	**μ**	**s**	**μ**	**s**	**μ**	**s**	**μ**	**s**
14 June 2017	-18.7	1.5	-19.0	3.8	-15.3	3.0	-15.6	2.3
20 July 2017	-16.0	1.5	-24.8	4.1	-14.0	2.0	-15.0	2.0
1 August 2017	-43.6	1.3	-53.2	3.4	-42.0	1.8	-42.4	2.1
25 August 2017	-15.5	1.4	-25.8	3.9	-14.1	2.1	-15.0	1.9
30 September 2017	-16.0	1.5	-24.6	3.7	-14.6	1.7	-15.0	1.9
12October 2017	-15.4	1.3	-22.2	5.4	-14.5	2.1	-15.4	1.8

μ and s are the mean and standard deviation, respectively, of backscatter (dB) at corresponding class and date.

Table 4.2 and Table 4.3 show the average temporal profiles of radar backscattering coefficient of Sentinel 1 RADAR VV and VH polarization data for different land-cover types: Non-rice crops, water, built up and trees. The backscatter values of non-rice crops ranging from -11.8 dB to -9.2 dB at VV polarization and -43.6 dB to -15.4 dB at VH polarization, because the non-rice crops in the study area are highly flooded, and there is high backscatter change on 01 August VH polarizations. As crops grow, backscatter increase mainly due to volume scattering. For both VV and VH polarizations, the radar backscattering coefficient of water on the different dates show a seasonal fluctuation ranging from -19 dB to -13.5 dB at VV polarization and -53.2 dB to -19.0 dB at VH Polarization. Water areas seem relatively dark at all polarizations and on all dates. The radar backscatter signals of the water surface fluctuate mainly due to wind effects. Water is separable from other land cover types for all polarizations and periods. The backscatter values of built up ranging from -9.9 dB to -7.8 dB at VV polarization and -42.0 dB to -14.0 dB at VH Polarization. The built up materials, such as steel and metals, have high radar backscattering coefficient. The backscatter values of trees show a fluctuation ranging from -10.7 dB to -9.5 dB at VV polarization and -42.4 dB to -15.0 dB at VH polarization. For trees, the radar backscattering coefficient may include direct backscattering from the crown volume, direct backscattering from the ground. The VH radar backscattering coefficients at the beginning of August are lower than those in other months. This is because of high rain in the Fogera wereda, so the surface is flooded and forms calm water which decreased the radar backscattering signal.

4.1.2.2 Separability measures using Bhattacharya distance

Results on the determination of the optimal polarization channel based on two-class signature separability measures are given in Table 4.4. Results are computed using Equation (3.4). Separability of rice class with non-rice crops, water, built up and trees was measured using Bhattacharya distance, as shown in Table 4.4. The minimum separability has been observed in VV polarization. Overall, the separability among various rice and other non-rice classes is low to very high.

Table 4.4 Comparison of two-class separability results at VV and VH polarizations.

Class Pairs	VV Polarization	VH Polarization
Rice and Non-Rice crops	0.5	1.3
Rice and Water	1.0	1.6
Rice and Built up	0.8	1.5
Rice and Trees	0.7	1.3
Non-Rice crops and Water	1.4	2.0
Non-Rice crops and Built up	0.4	0.8
Non-Rice crops and Trees	0.3	0.8
Water and Built up	1.3	2.2
Water and Trees	1.4	2.0
Built up and Trees	0.4	0.3

From Table 4.4, the class pair “rice and non-rice crops” is not largely separable as the latter is a combination of crop types (wheat, maize, sorghum, teff, horticulture etc.) which generally exhibit similar (low) backscatter values especially at the start of the rice growing season. The class pair “rice and trees” is not largely separable, thus will be improved using optical indices. In general, a separability value below 0.8 is regarded not large enough to separate two classes. Between 0.8 and 1.5, the quality of the separation between the two classes is regarded as average. Values above 2.0 indicate almost complete separability between classes (Shi *et al.*,1994). From Table 4.4, it can be observed that with exception of the class pairs “built up and trees”, the VH polarization produces better inter-class signature separability. Based on the most sustained increase in paddy rice backscatter at the VH polarization, and the superiority of the VH over the VV channel in the two-class separability measure, the VH polarization as the optimal polarization and with which the optical indices are combined for the mapping of rice fields and the other land-cover categories in this study. It has also been observed that C-band, cross (VH) polarization produces better crop classification results than the like (VV) polarization, and the use of dual polarization does not further improve the classification results. Figure 4.3 shows the

average temporal backscatter profiles of rice class and the other broad land-cover at the VH polarization

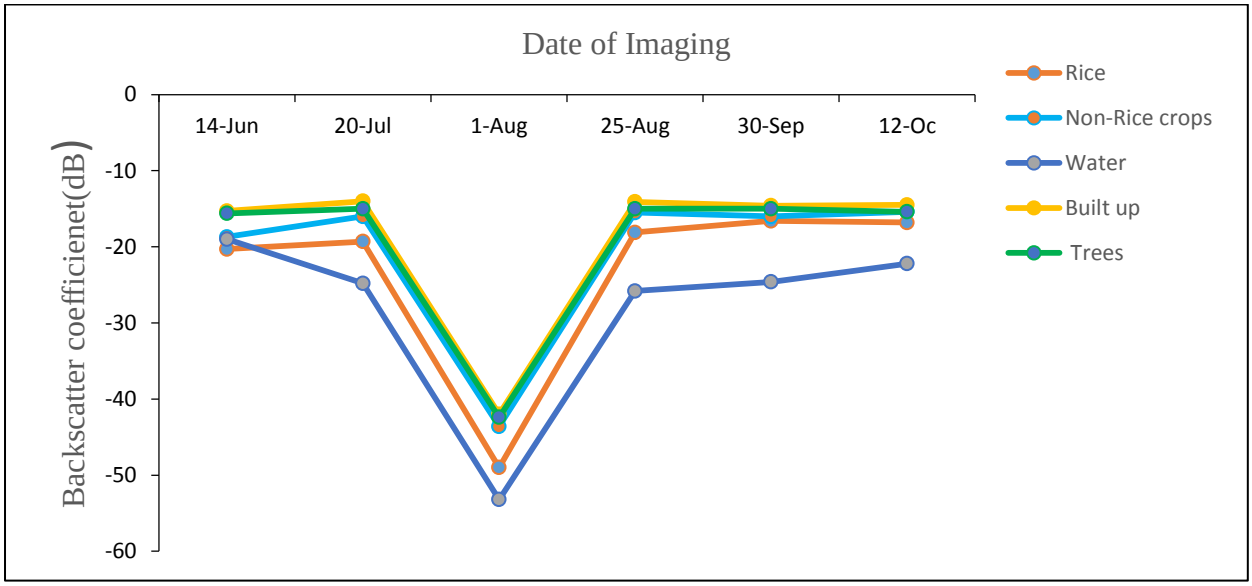

Figure 4.3: The average temporal backscatter profiles of rice class and the other land-cover at VH polarization.

In Figure 4.3, it can be clearly seen that, apart from the rice class, the other land-cover classes especially built up and trees show higher overlap temporal backscatter profiles to all paddy rice growing season. In addition, mapping and monitoring of rice after 01 August VH images was not possible, due mainly to high overlap of rice backscatter with the other land-cover classes. Therefore, based on the observed increase in the backscatter of paddy rice at the first two months of growth and its sharp decline temporal backscatter profiles of rice and the other land-cover classes of 01 August imaging date was used for mapping algorithms. In this research study, two mapping algorithms were applied. One obtained only from the temporal VH images of Sentinel 1 RADAR and the other derived from the synergistic application of temporal Sentinel 1 RADAR images and single-date Sentinel 2 indices. To map rice and other land-cover classes using optimal Sentinel 1 RADAR VH images, machine learning CART algorithms are used to identify optimal nodes.

4.1.3 Optimal node of Sentinel 1 RADAR VH images

Figure 4.4 shows the optimal node that identified rice from other land-cover classes. The backscatter values of this optimal node identified by CART is used to map rice and the other land- cover types in the subsequent analysis.

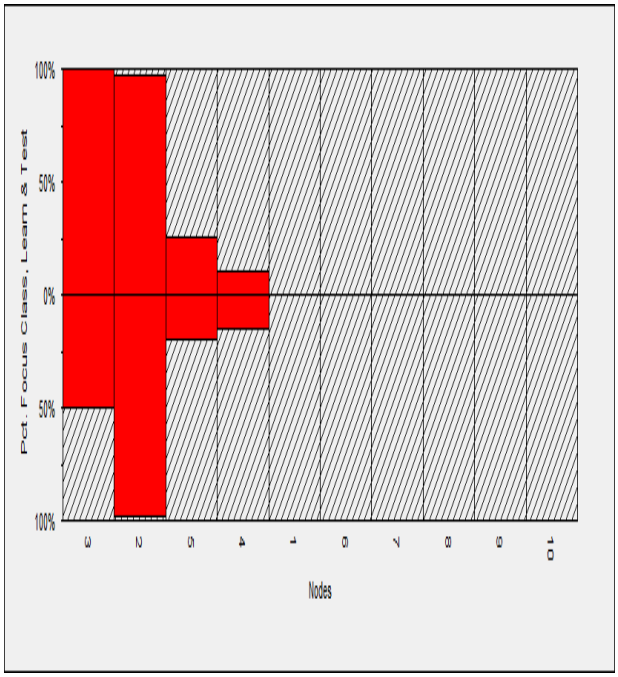

(a) Rice

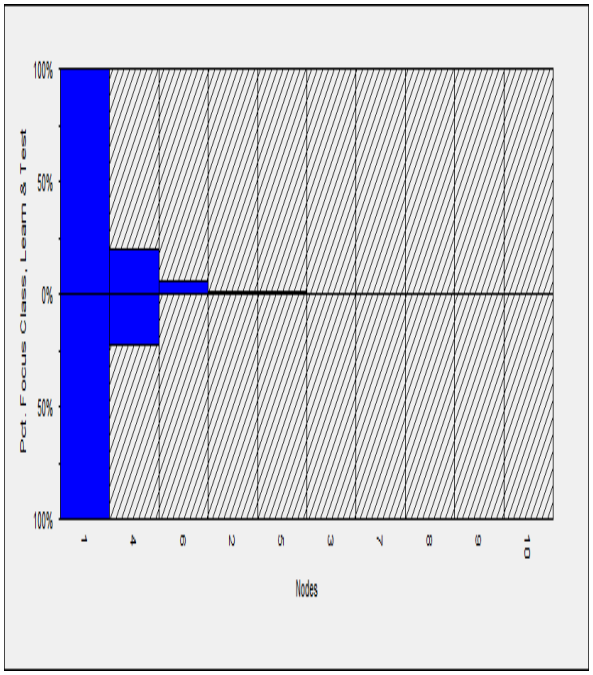

(b) Water

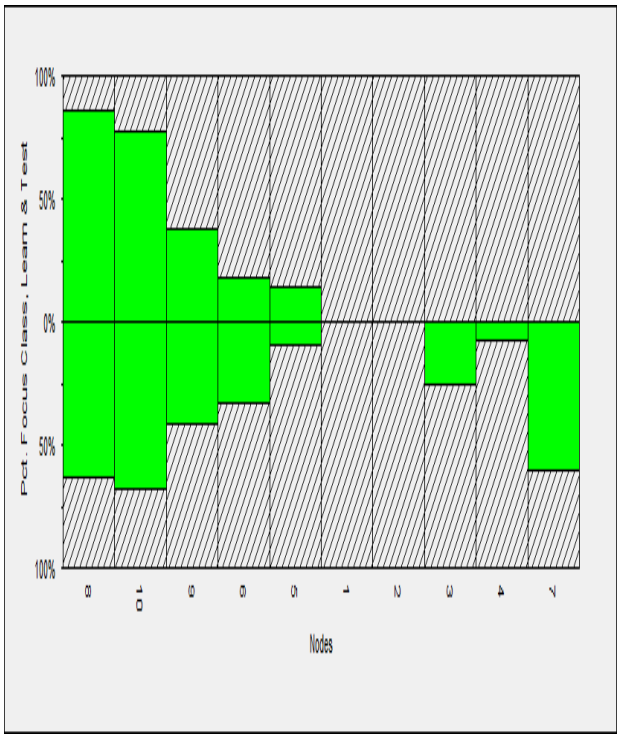

(c) Built up

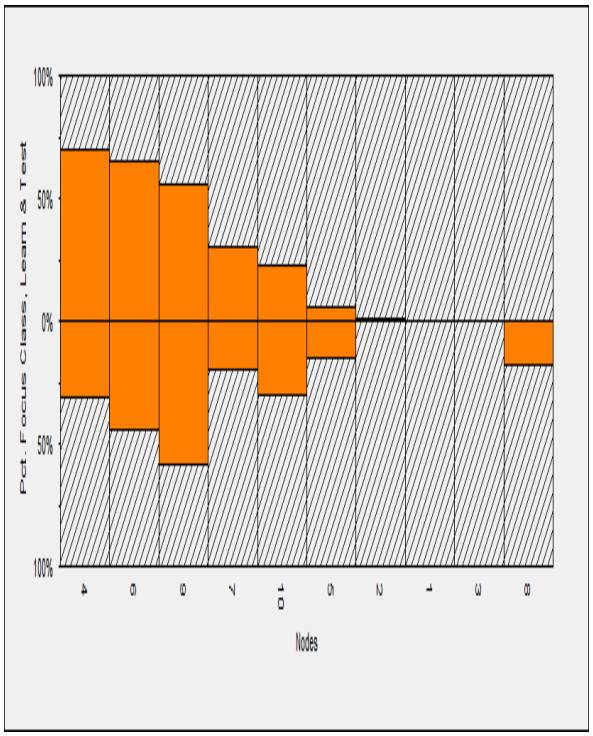

(d) Trees

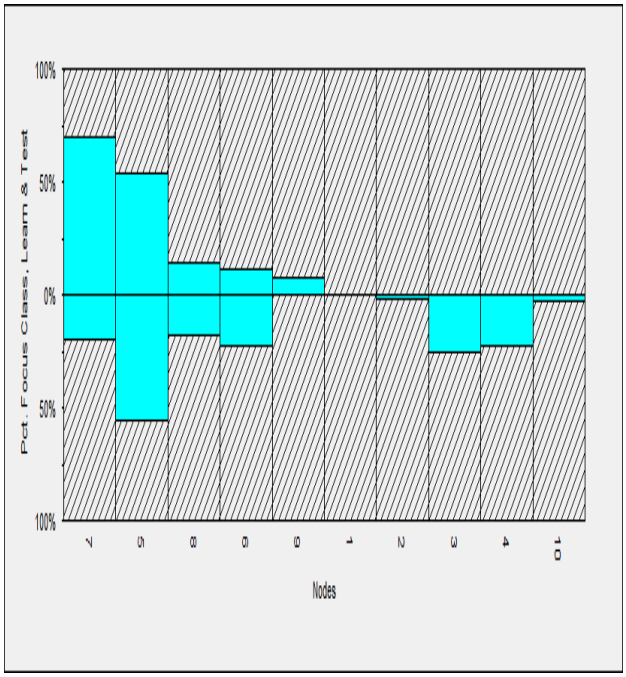

(e) Non-Rice crops

Figure 4.4: The optimal nodes of rice and other land-cover classes

Based on figure 4.4, Node 3 and Node 2 are the 14 June and 01 August, respectively of Sentinel 1 RADAR VH image optimal nodes that differentiate rice from the other land-cover classes. For the mapping of water Node1 (25 August), Node 8 (12 October) and Node 10 (25 August) was used for the mapping built up , Node 4 (14 June), Node 6 (25 August) and Node 9 (25 August) was used for the mapping of trees and Node 7 (25 August) and Node 5 (14 June) was used for the mapping of non-rice crops.

4.1.4 Variable Importance

Figure 4.5 shows that the percentage of each imaging date importance developed using CART model to differentiate land-cover classes at VH polarizations image.

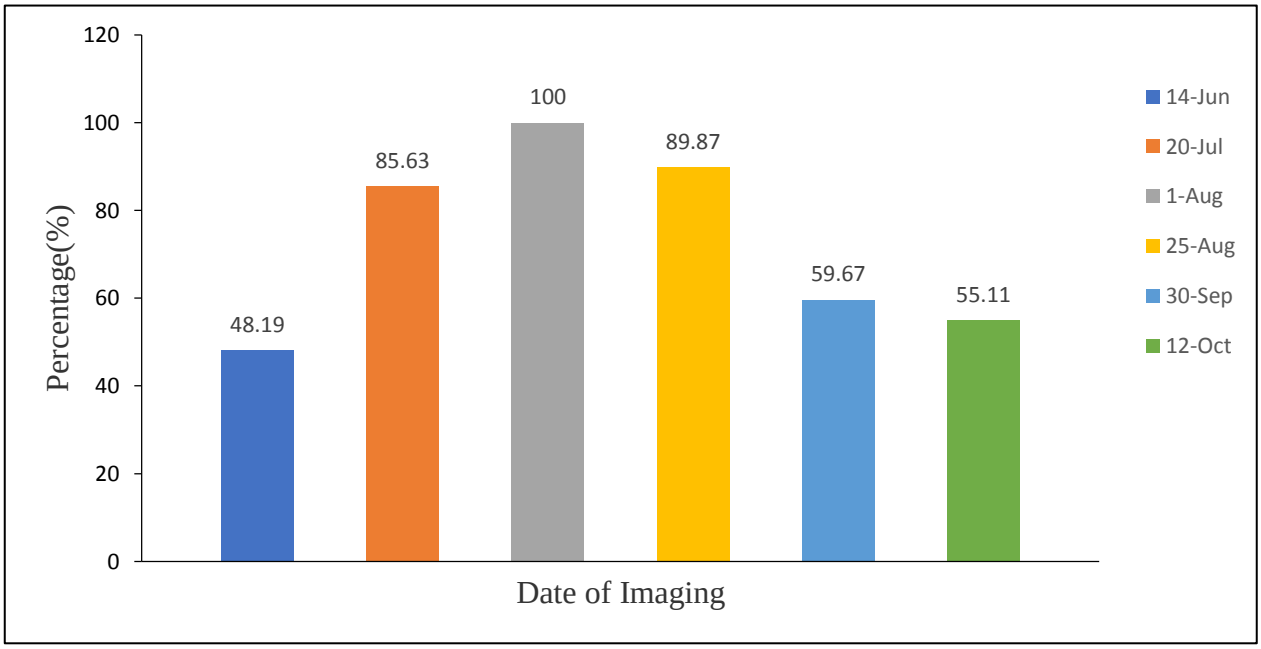

Figure 4.5: The optimal variable importance in terms of percentage.

Figure 4.5 shows the importance of the six-date images in separating land-cover classes. One can see that the VH polarization image of 01 August has high importance in separating the different land-cover classes (100%), followed by 25 August and 20 July 2017. The Sentinel 1 RADAR VH polarization image of 14 June, 30 September and 12 October 2017 has relatively low importance to separate land-cover classes. Based on the variable importance identified, the land-cover type mapped using Sentinel 1 RADAR VH polarization images in the subsequent imaging date has a different degree of misclassification errors.

4.1.5 Rice Mapping Results from Sentinel 1RADAR VH Images

Results from the use of only 14 June VH images of Sentinel 1 RADAR data are presented in Figure 4.6.

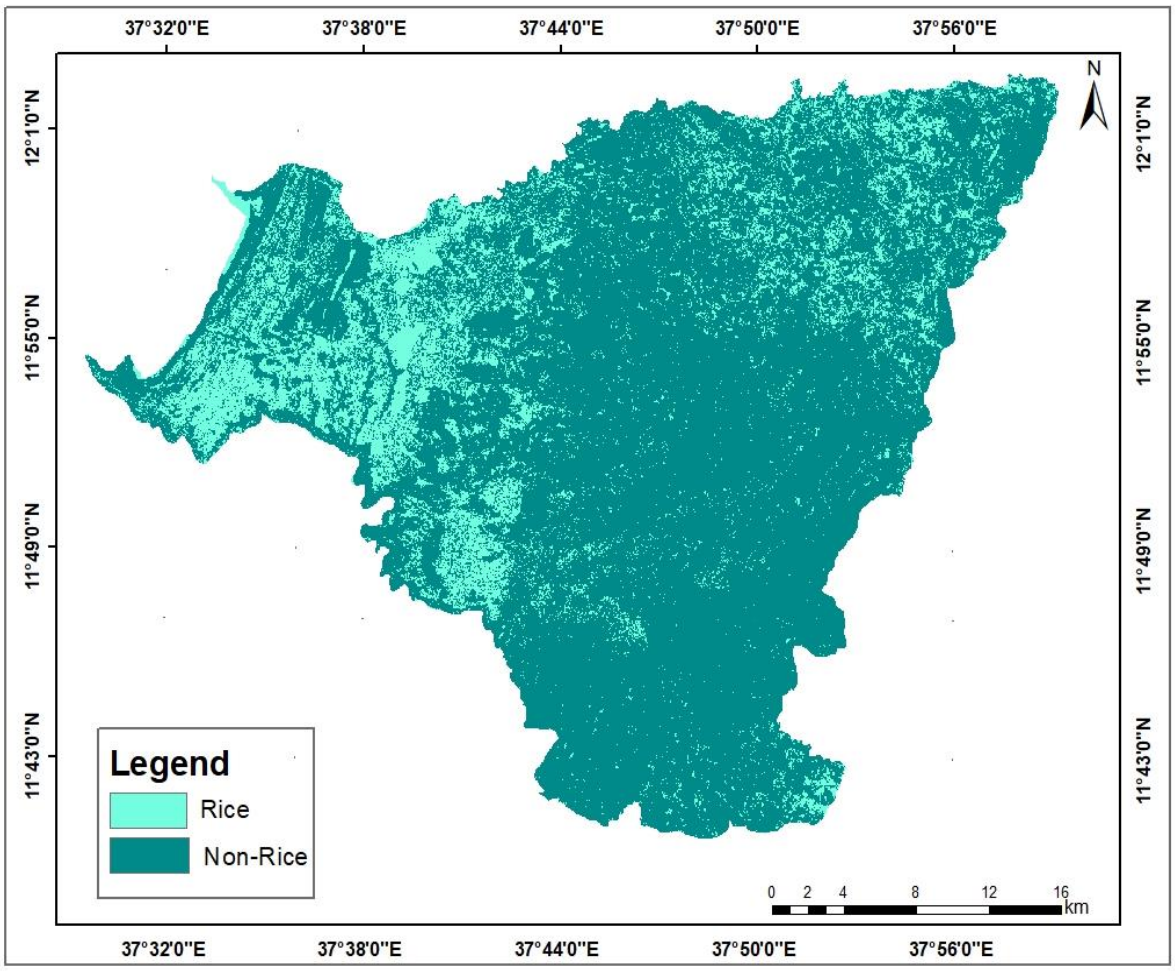

Figure 4.6: Simplified rice and non-rice map of study area derived from the use of only 14 June VH images of Sentinel1RADAR data.

In Figure 4.6, paddy rice mapped using 14 June Sentinel 1 RADAR VH image show wide misclassification errors, mainly due to differences in planting dates and varieties. Late planting rice crop is not mapped using 14 June imaging date. As temporal backscatter coefficients of rice

are largely a function of rice growth stage and conditions, inter-field differences between paddy fields could affect the performance of rice mapping algorithms in which temporal backscatter change is used as the main classification feature. In a single-season rice cultivation system, planting dates could vary up to 3 weeks between adjacent paddy rice fields. Mapping paddy field using 01 August Sentinel 1 RADAR VH polarization imaging date could improve the classification accuracy.

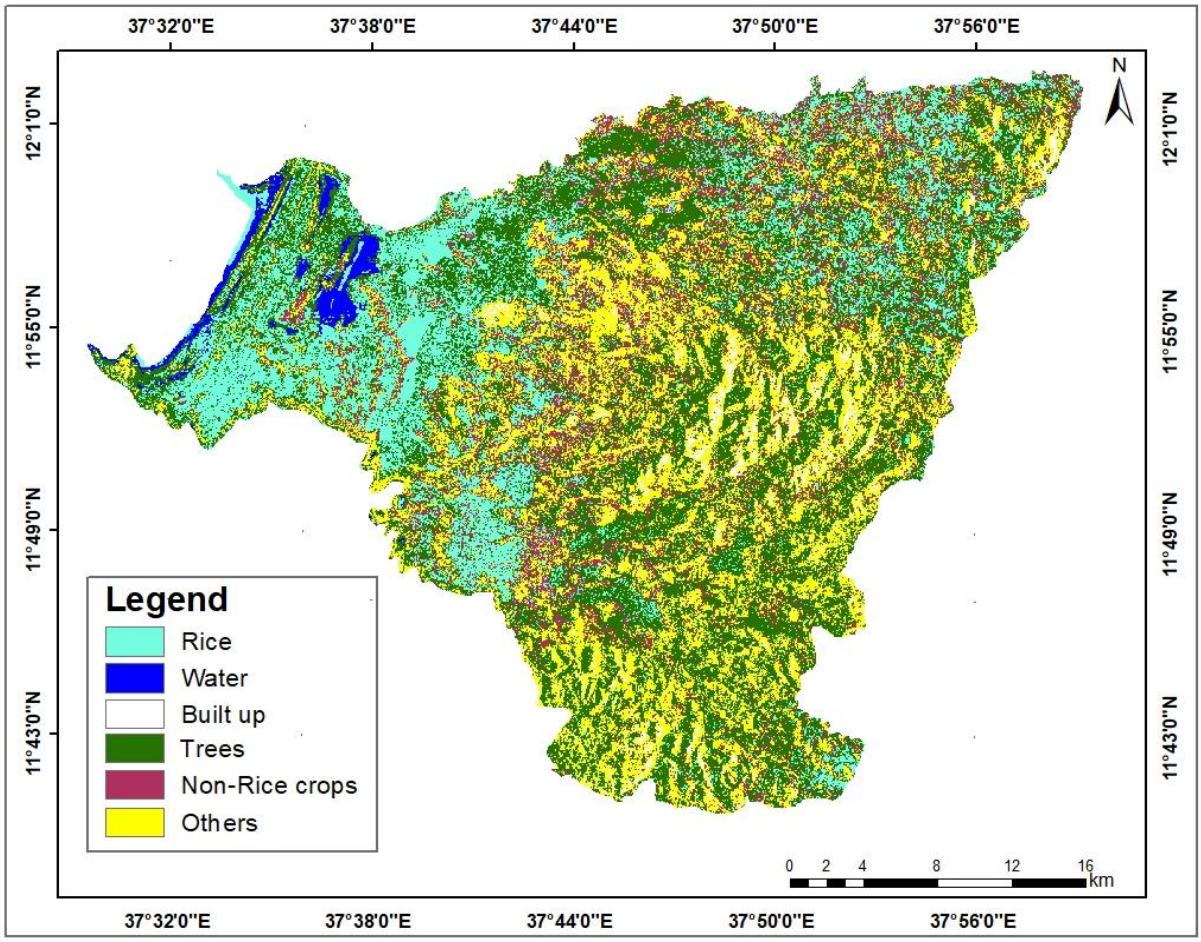

Figure 4.7: Simplified rice and the other land-cover map of study area derived only from VH images of Sentinel 1RADAR data.

In Figure 4.7, it can be observed that there are wide misclassifications especially with rice, built up and trees. Some pixels within deep water surfaces have been classified as rice. Even on land, more pixels have been misclassified as rice. These areas typically show low microwave backscatter. As the prevalence of surface winds could increase the roughness and, hence, the backscatter signals at a subsequent acquisition, some of these pixels could be misclassified as rice. From the total area of the wereda, paddy rice field accounts 20,911.2 ha. The accuracy assessment report for the land-cover map presented in Figure 4.7 is given in Table 4.5 - 4.8.

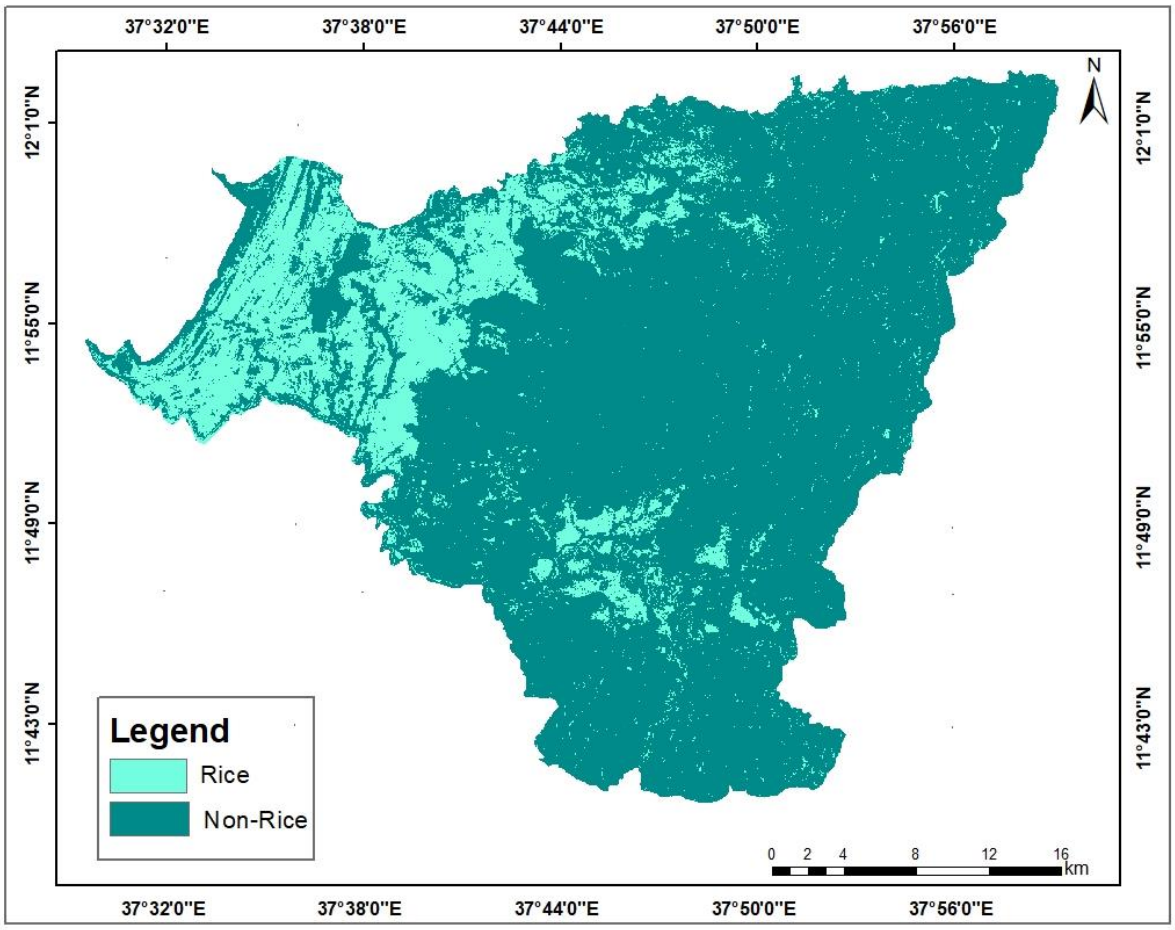

Figure 4.8: Simplified rice and non-rice map of study area derived only from the use of only 01 August VH images of Sentinel1RADAR data.

Figure 4.8 shows rice and non-rice map of the study area based on 01 August Sentinel 1 RADAR VH images. Based on the optimal node identified in Figure 4.4 paddy rice in this imaging date identified were more accurate. This indicates late planting of paddy rice in this area in 2017 were identified based on 01 August VH images. In addition, based on the variable importance in Figure 4.5, 01 August VH image shows higher percentage in separating the different land-cover types. From the total area of the wereda, paddy rice field accounts 19,846.9 ha. CART model integrated 14 June and 01 August Sentinel 1 RADAR VH image to improve the mapping accuracy of paddy fields. The accuracy assessment report for the land-cover map presented in Figure 4.8 is given in Table 4.5 - 4.8.

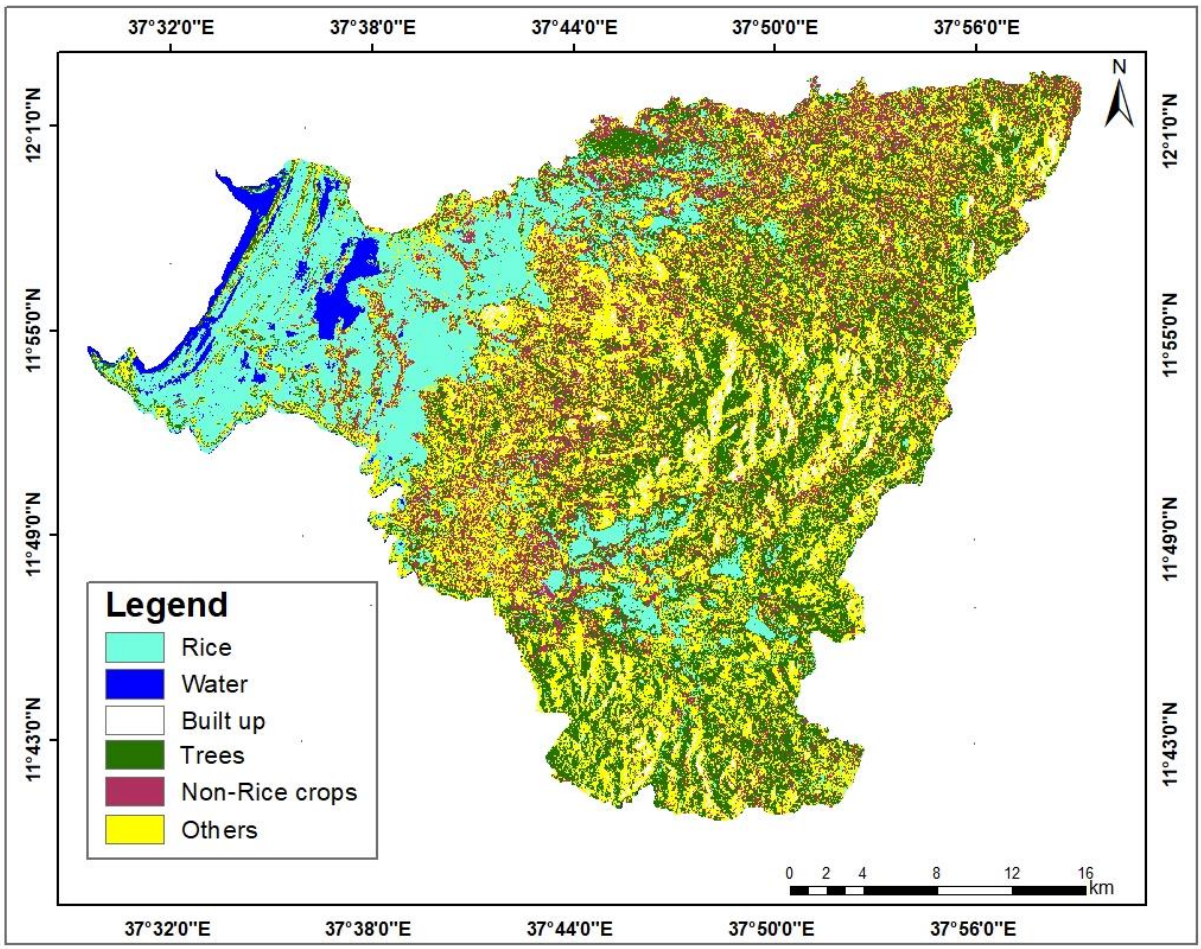

Figure 4.9: Simplified rice and the other land-cover map of study area derived only from VH images of Sentinel 1RADAR data.

4.1.6 Accuracy assessment

To calculate accuracy levels, an error matrix is constructed to show the discrepancy between classified categorical maps and their corresponding actual or reference maps for the selected locations (Lo and Yeung, 2005). The error matrix or confusion metrics is an array of values assigned to a category in the reference data and the classified map to be evaluated. The rows represent the categories of the classified map while columns represent the categories of validation data in the error matrix as shown in Tables 4.5, 4.6, 4.9 and 4.10. The values along the diagonal represent the number of correctly classified points or the number of points that agree with validation data. All non-zero values of the diagonal indicate disagreement of the classified map and validation data or misclassification of pixels, i.e. errors of commission and omission. Commission errors are wrong inclusions and indicate the number of points whose pixels wrongly included in row categories, but omission errors are wrongly excluded pixels from column categories. As such the elements in the error matrix are represented as Cij (the value in the ith

row and jth column) and refer to the number of points assigned to category i of the classified map while it belongs to category j.

The minimum producer's accuracy (PA) report for the study is found to be 48.6%, 51.4% and 58.3% mapping results from Sentinel 1 RADAR VH images and 64.0% mapping results from integrated Sentinel 1 RADAR and Sentinel 2 optical indices image classification. The accuracy assessment for water category is exceptionally highest in all accuracy assessment results for samples drawn from this category are very small and the area covered by water is easily differentiated during classification. Accuracy assessment evaluation results for user's accuracy (UA) range from 50.7% to 100% for all categories. Therefore, the results in both producer's and user's accuracy show that the performance of classification for mapping results from Sentinel 1 RADAR VH and integrated Sentinel 1 RADAR VH and Sentinel 2 optical indices error margins are within acceptable accuracy for rice and water and unacceptable accuracy for built up, trees, non-rice crops and other land-cover types. The overall accuracy of the report for this study from mapping results using Sentinel 1 RADAR VH images developed by CART are 74.3% for learn data and 69.9% for test data, and the overall accuracy of the report developed from mapping results from integrated Sentinel 1 RADAR VH and Sentinel 2 optical indices image are 79.5 % for 2017 classified maps. The accuracy assessment report for the land-cover map was extracted using CART model are presented in Table 4.5 – 4.8. The accuracy assessment summarized each optimal node impurities. In Table 4.5, even though most learn points of rice have been correctly classified, there are some commission errors in this class. 18 commission errors in non-rice crops are derived from the misclassification of rice. 24 commission errors in built up are derived from the misclassification of trees. 9 commission errors in trees are derived from the misclassification of built up. In addition, 6 omission errors in the class non-rice crops are derived from the misclassification of trees. Water shows a relatively good agreement with learn data.

Table 4.5 Confusion Matrix - Learn classification with Sentinel 1 RADAR VH images.

Classes	Rice	Water	Built	Trees	Non-Rice crops	Row Total
Rice	74	3	0	1	0	78
Water	0	33	0	0	0	33
Built up	0	0	36	9	1	46
Trees	1	0	24	49	6	83
Non-Rice crops	18	2	10	7	45	82
CT	93	38	70	66	52	319
PA (%)	79.6	86.8	51.4	74.2	86.5	
UA (%)	94.9	100.0	78.3	59.0	54.9	
Overall Classification Accuracy: 74.3%			Kappa Statistic: 0.67			

CT, PA, and UA are column total, producer's accuracy, and user's accuracy, respectively.

In Table 4.6, even though most test points of rice have been correctly classified, there are some commission errors in this class. 12 commission errors in non-rice crops are derived from the misclassification of rice. In the land-cover types of built up, trees and non-rice crops show no improvement in accuracy. Water shows a relatively very good agreement with test data.

Table 4.6 Confusion Matrix - Test classification with Sentinel 1 RADAR VH images.

Classes	Rice	Water	Built	Trees	Non-Rice crops	Row Total
Rice	62	3	1	0	2	68
Water	0	37	0	0	0	37
Built up	0	0	34	14	3	51
Trees	2	0	23	35	5	68
Non-Rice crops	12	0	12	11	36	71
CT	76	40	70	60	46	292
PA (%)	81.6	92.5	48.6	58.3	78.3	
UA (%)	91.2	100.0	66.7	51.4	50.7	
Overall Classification Accuracy: 69.9%			Kappa Statistic:0.62			

CT, PA, and UA are column total, producer's accuracy, and user's accuracy, respectively.

In Table 4.7, the misclassification error for each land-cover type was computed. The highest misclassification error report for the study is found 34, 19, and 17 for learn data of the 2017 classification results for built up, rice and trees land-cover types, respectively.

Table 4.7 Misclassification – Learn with Sentinel 1 RADAR VH images

Classes	No. Cases	No. Mis-Classed	Pct. Error	Cost
Rice	93	19	20.43	0.20430
Water	38	5	13.16	0.13158
Built up	70	34	48.57	0.48571
Trees	66	17	25.78	0.25758
Non-Rice crops	52	7	13.46	0.13462

In Table 4.8, the misclassification error for each land-cover type was computed. The highest misclassification error report for the study is found 36, 25, and 14 for test data of the 2017 classification results for built up, trees and rice land-cover types, respectively.

Built up, Trees and Non-Rice crops test sample cost is greater than learn sample cost, which indicates poor cross-validation

Table 4.8 Misclassification – Test with Sentinel 1 RADAR VH images

Classes	No. Cases	No. Mis-Classed	Pct. Error	Cost
Rice	76	14	18.42	0.18421
Water	40	3	7.50	0.07500
Built up	70	36	51.43	0.51429
Trees	60	25	41.67	0.41667
Non-Rice crops	46	10	21.74	0.21739

4.1.7 Mapping Results from Sentinel 1 RADAR and Sentinel 2

Results from the proposed mapping algorithm, which utilizes both the temporal VH images of Sentinel 1 RADAR and the single-date NDVI and MNDWI from Sentinel 2 are presented in Figure 4.10 and 4.11.

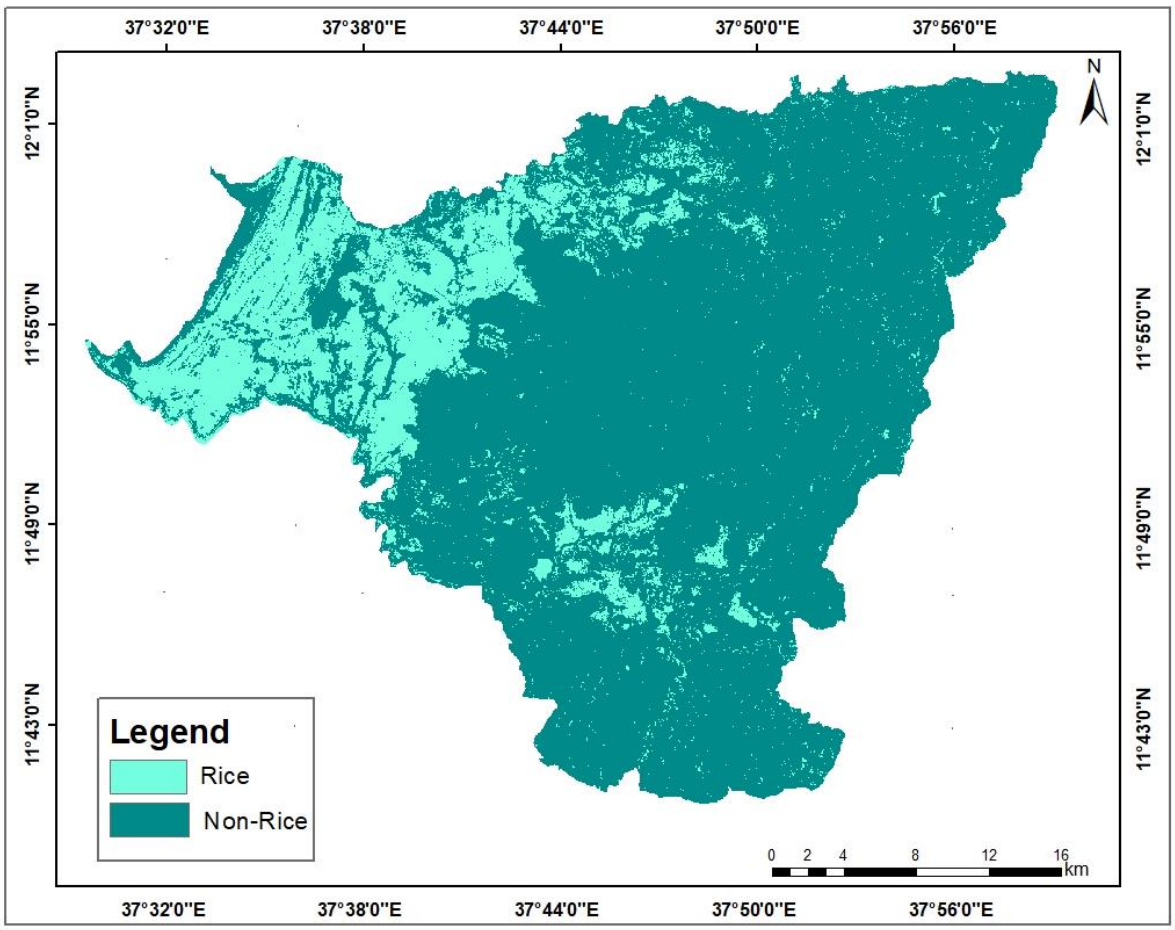

Figure 4.10: Simplified rice and non-rice map of study area derived from Sentinel 1 RADAR VH and Sentinel 2 optical images.

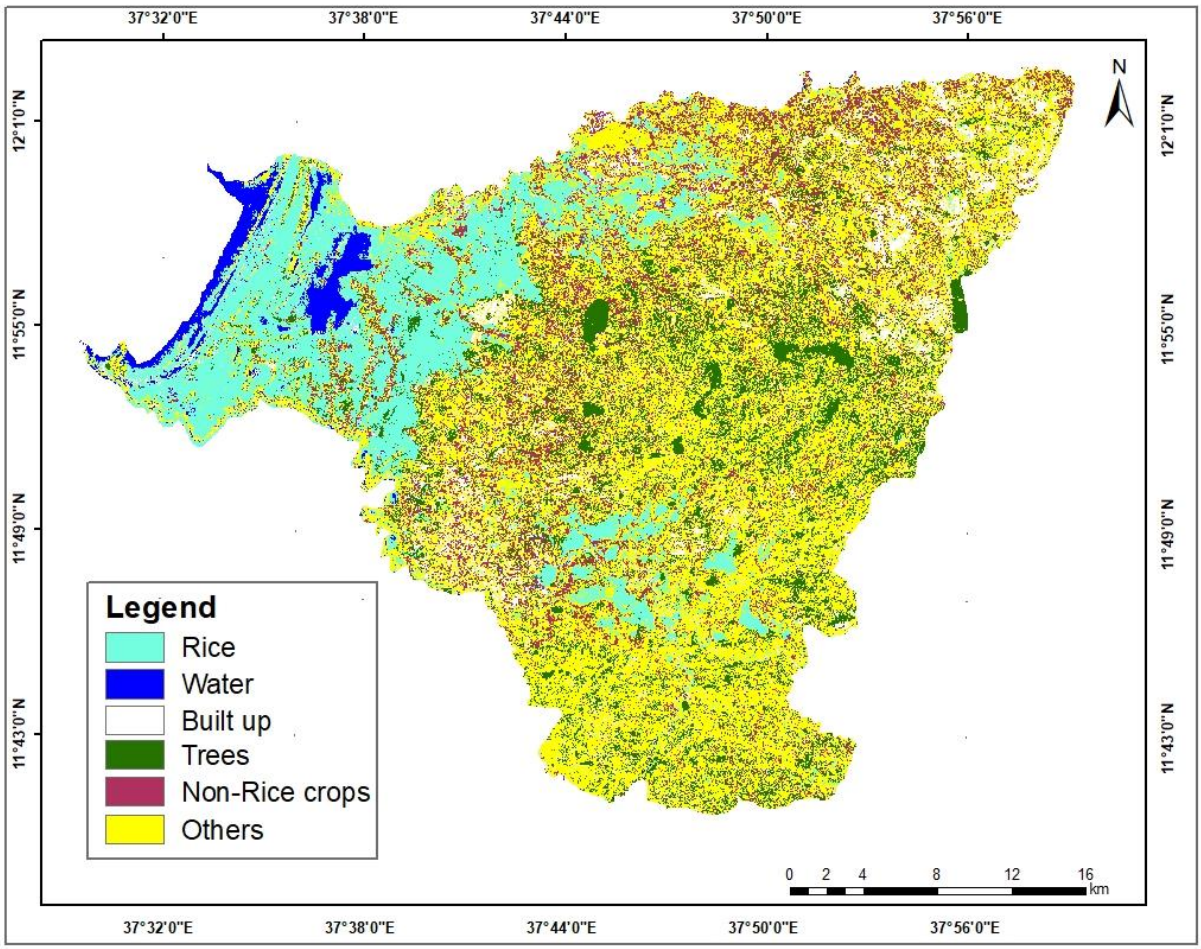

Figure 4.11: Simplified rice and the other land-cover map of study area derived from Sentinel 1RADAR VH and Sentinel 2 optical images.

In Figure 4.11, 88 test classification errors observed in Figure 4.9 have been reduced significantly with the introduction of single-date optical indices (NDVI and MNDWI). Figure 4.11 shows greater class homogeneity as much of the misclassified, island or mixed pixels have been eliminated compared to maps using Sentinel 1 RADAR VH images. Rice is more clearly delineated. The area covered by trees has significantly reduced as a consequence of the increase in the area covered by the class others. In addition, the area covered by built up and non-rice crops has significantly increased as a consequence of the decreased in the area covered by the class trees. The classification accuracy assessment of simplified rice and the other land-cover map is shown in Table 4.9.

Table 4.9 Error matrix of accuracy assessment of classification with Sentinel 1 RADAR VH and Sentinel 2 optical.

Classes	Rice	Water	Built	Trees	Non-Rice crops	Others	Row Total
Rice	70	0	0	0	0	0	70
Water	1	38	0	0	0	2	41
Built up	0	0	51	8	1	5	65
Trees	0	0	8	42	2	6	58
Non-Rice crops	3	0	5	4	39	5	56
Others	2	2	6	6	4	32	52
CT	76	40	70	60	46	50	342
PA (%)	92.1	95.0	72.9	70.0	84.8	64.0	
UA (%)	100	92.7	78.5	72.4	69.6	61.5	
Overall Classification Accuracy: 79.5%				Kappa Statistic:0.76			

CT, PA, and UA are column total, producer's accuracy, and user's accuracy, respectively.

In Table 4.9, the commission errors previously recorded in rice have all been eliminated, with, however, 6 omission errors. There is an increase in the accuracy of built up and trees. In Figure 4.11, it can be clearly seen that, integrating Sentinel 1 RADAR and Sentinel 2 optical indices improve the land-cover accuracy of rice which is a major focus of this study. From the total area of the wereda, paddy rice field accounts 19,157.8 ha. Paddy rice cultivation is mostly concentrated in the northwestern part of the study area, which mainly includes the lowland paddy rice.

4.1.8 Mapping Inundation

Rice systems vary spatially across Fogera wereda and can undergo tremendous variability with the magnitude and timing of inflection in Sentinel 1 RADAR requiring robust approaches to accurately map inundation. In the present study, the optimal node value for discrimination of the inundated area from non-inundated was set in the Figure 3.13. Relatively high inundation was observed on 01 August 2017. Inundation map and areal coverage of the study area using sentinel 1 RADAR optimal polarization (VH) is shown in Figure 4.12 - 4.17 on six dates from the 2017 time-series.

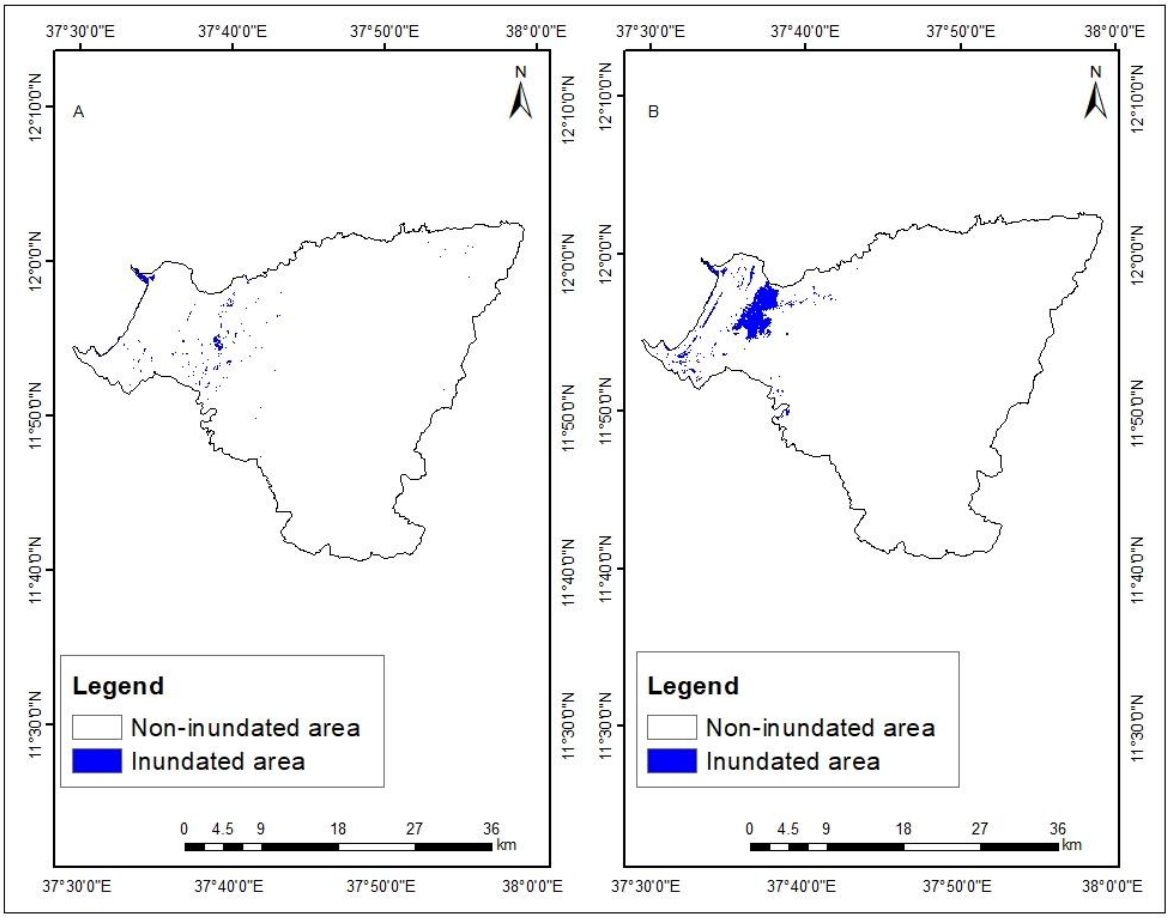

Figure 4.12: Inundation patterns in Fogera wereda using Sentinel 1 RADAR VH images, (A) 14 June and (B) 20 July images.

The extracted inundation areal coverage using the 14 June and 20 July Sentinel 1 RADAR VH images is shown in Figure 4.13.

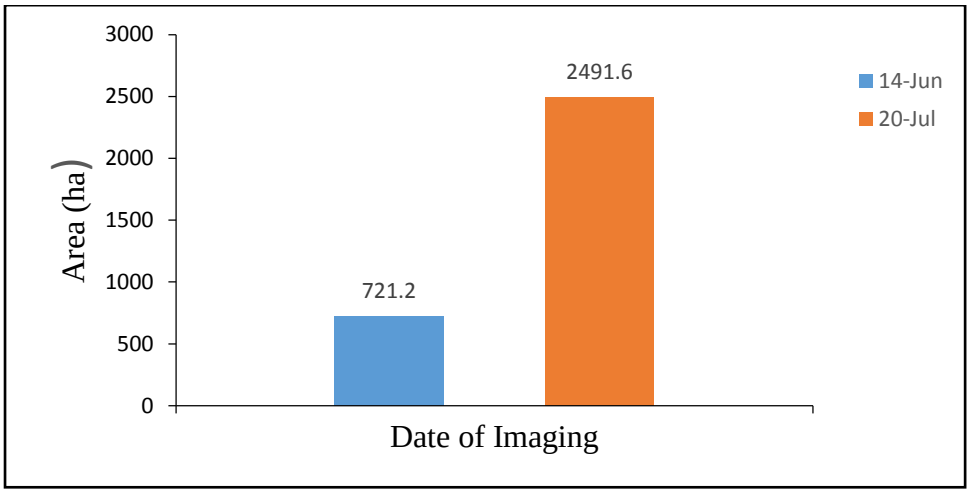

Figure 4.13: The 14 June and 20 July 2017 inundated areal extent calculated using CART modeling techniques.

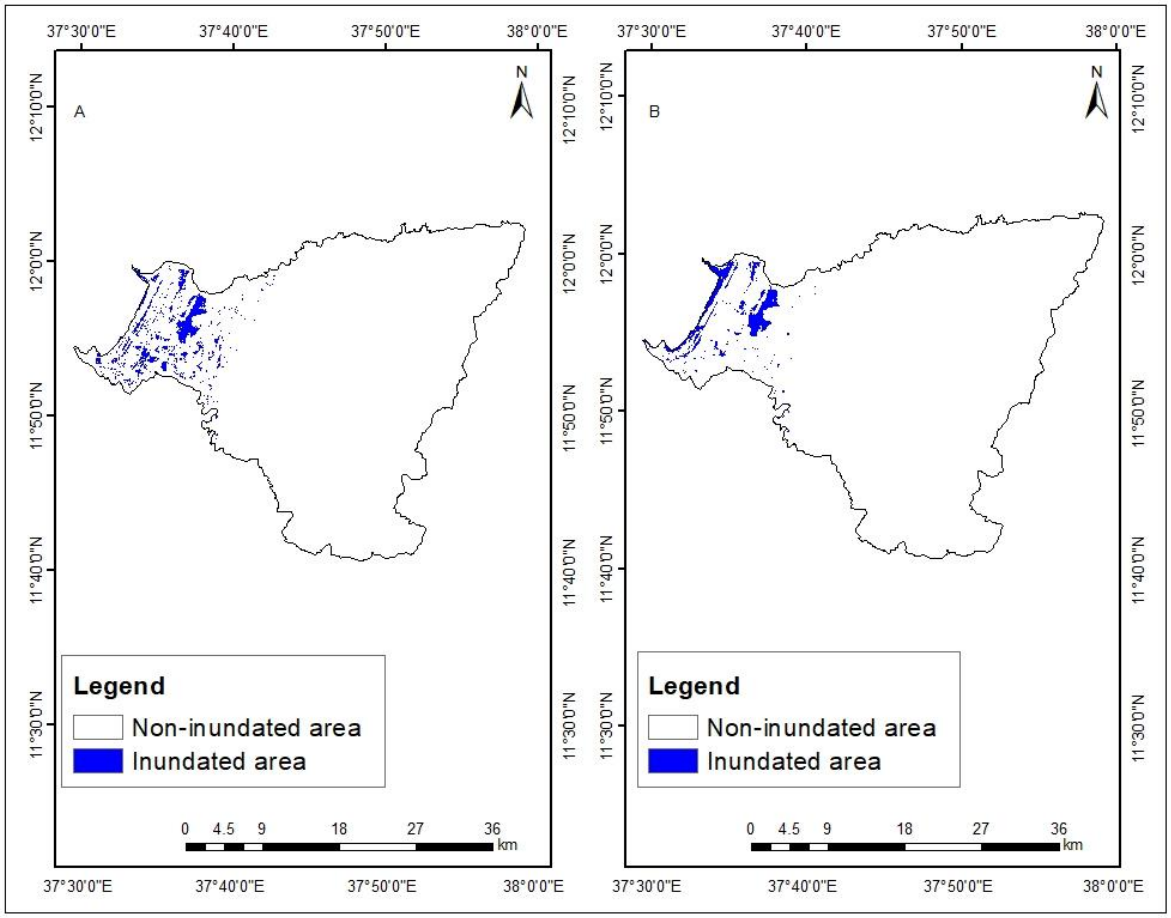

Figure 4.14: Inundation patterns in Fogera wereda using Sentinel 1 RADAR VH images, (A) 01 August and (B) 25 August images.

The extracted inundation areal coverage using the 01 August and 25 August Sentinel 1 RADAR VH images is shown in Figure 4.15.

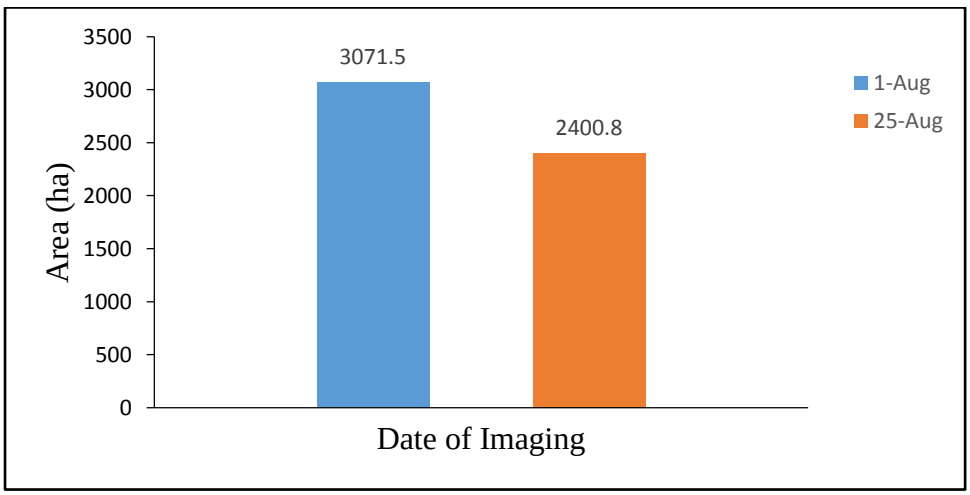

Figure 4.15: The 01 August and 25 August 2017 inundated areal extent calculated using the CART modeling techniques

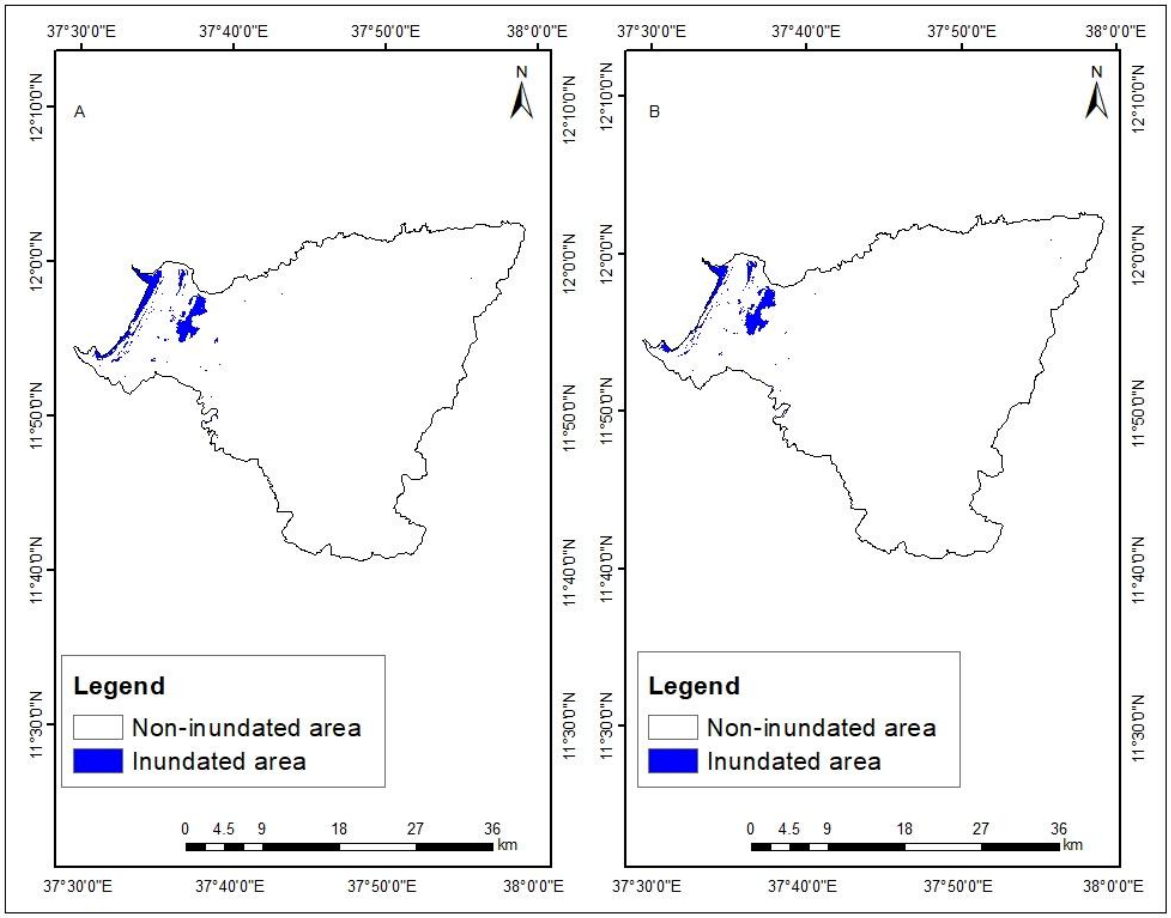

Figure 4.16: Inundation patterns in Fogera wereda using Sentinel 1 RADAR VH images, (A) 30 September and (B) 12 October images.

The extracted inundation areal coverage using the 30 September and 12 October Sentinel 1 RADAR VH images is shown in Figure 4.17.

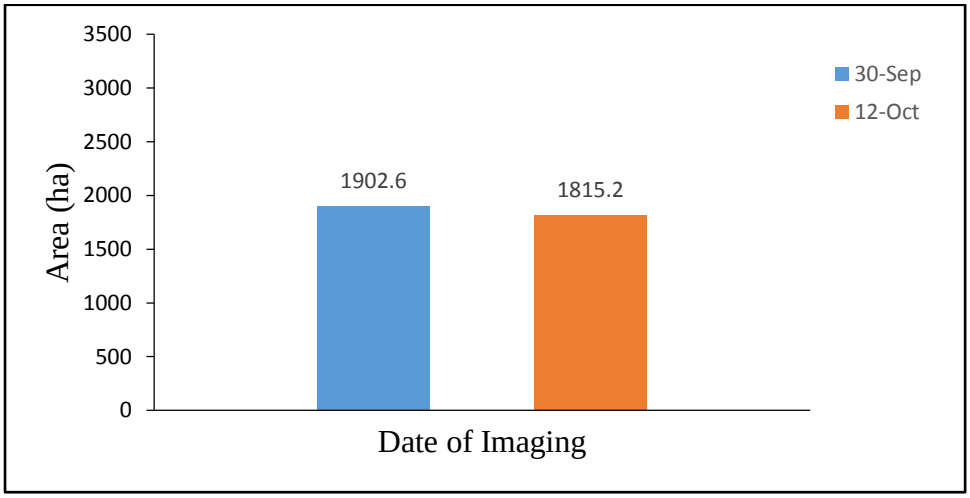

Figure 4.17: The 30 September and 12 October 2017 inundated areal extent calculated using CART modeling techniques.

Sentinel 1 RADAR VH images are now more accurate to map and monitor the amount of hydroperiod information (i.e., frequency, duration, timing), especially in cloudy regions such as Ethiopia. Figure 4.12, 4.14 and 4.16 show inundation is mostly concentrated in the northwestern part, which mainly includes the lowland paddy fields of the study area. Figure 4.15 show inundated area in ha during 01 and 25 August covered large area compared to other imaging dates mainly due to the overflow of the two major rivers (Rib and Gumera) that recharge Lake Tana. The time series inundation map showed the large area covered by water. The inundated area is mostly concentrated in the northwestern part of the study area, which mainly includes the lowland paddy rice field of the wereda. The CART learn data (optimal node) in Figure 3.12 was validated using test data matrix generated by CART model. The accuracies of Sentinel 1 RADAR VH polarization in identifying inundated area from the non-inundated area are shown in Table 4.10. The accuracy assessment generated by CART model summarized the 6 optimal node impurities. In Table 4.10, even though most test points of the inundated area have been correctly classified, there are some commission errors in this class. 4 commission errors in the non-inundated area are derived from the misclassification of inundated area. In addition, 1 omission errors in the class non-inundated area are derived from the misclassification of inundated area.

Table 4.10 Confusion Matrix - Test classification with Sentinel 1 RADAR VH images.

Class	Non-inundated area	Inundated area	Row Total
Non-inundated area	251	4	255
Inundated area	1	36	37
CT	252	40	292
PA (%)	99.6	90	
UA (%)	98.4	97.3	
Overall Classification Accuracy: 98.3 %		Kappa Statistic: 0.93	

CT, PA, and UA are column total, producer's accuracy, and user's accuracy, respectively.

Table 4.10 shows the accuracy for the inundated area of the study. The accuracy for the inundated area shows good agreement with test data.

4.1.9 Rice and other land use statistics

Table 4.11 Rice land use area (in ha)

Date	14 June VH Images	01 August VH Images	VH + optical indices
Area (in ha)	20,911.2	19892.5	19157.8

Table 4.11 shows the area of rice crop at different rice growth phase. Rice crop mapped using the three different imaging date shows variations in terms of areal coverage and mapping accuracy. 14 June and 01 August Sentinel 1 RADAR derived operational estimate show a difference of 1,018.7 ha. 01 August Sentinel 1 RADAR derived rice field estimate and mapping results using integrating Sentinel 1 RADAR VH images and optical indices show a difference of 734.7 ha. Monitoring paddy fields (area) through different time mapping in one growing season is important, mainly to exclude the damaged paddy field and to include the late sowed and misclassified rice. Table 4.12 shows the area mapped using Sentinel 1 RADAR VH optimal image (01 August) and by integrating optimal image with sentinel 2 optical indices of different land-cover types.

Table 4.12 Rice and other land use area (in ha)

Land use type	VH Images area (in ha)	VH + optical indices area (in ha)
Water	2400.8	1791.2
Built up	3049.6	8867.9
Trees	32583.6	14238.1
Non-Rice crops	17746.9	22634.2
Others	35467	44451.2

4.1.10 Estimation of Production Under Rice Cultivation

The area under rice cultivation in Fogera wereda from 2007 to 2016 reported by Fogera wereda Agricultural and Rural Development Office is plotted in Table 4.13. It shows that the reported rice area ranged between 11,085 ha in 2007 and 21,945 ha in 2016. Integrating Sentinel 1 RADAR and Sentinel 2 optical indices derived operational estimate for the year 2017 was 19,157.8 ha and the available rice census provided by Fogera wereda Agricultural and Rural Development Office rice area was 22,105 ha. This is a difference of 2,947.2 ha.

Table 4.13 Rice-cropped area, total production, and yield reported by Fogera wereda Agricultural and Rural Development Office.

Year	No. of HHs	Area (ha)	Total Production (Tons)	Yield (Tons/ha)
2007	12145	11085	664161	59.9
2008	17358	11146	660672	59.3
2009	20582	14149	850717	60.1
2010	21945	18428.5	1137783	61.3
2011	26248	16070.5	1166473	72.6
2012	29912	19310	1587366	82.2
2013	30481	19333.75	1506673	77.9
2014	36547	20896	1540860	74.6
2015	37423	21341	1589905	74.5
2016	38482	21945	1711710	78

The rice area (ha) in Fogera wereda is plotted against total production (Tons) in Figure 4.18. A moderate linear regression equation with the goodness of fit $R^2 = 0.94$ based on the area and total production reported area was developed and is given below: The scattering of data points in Figure 4.18: can be categorized into a single point (down left) and a points cluster (upright).

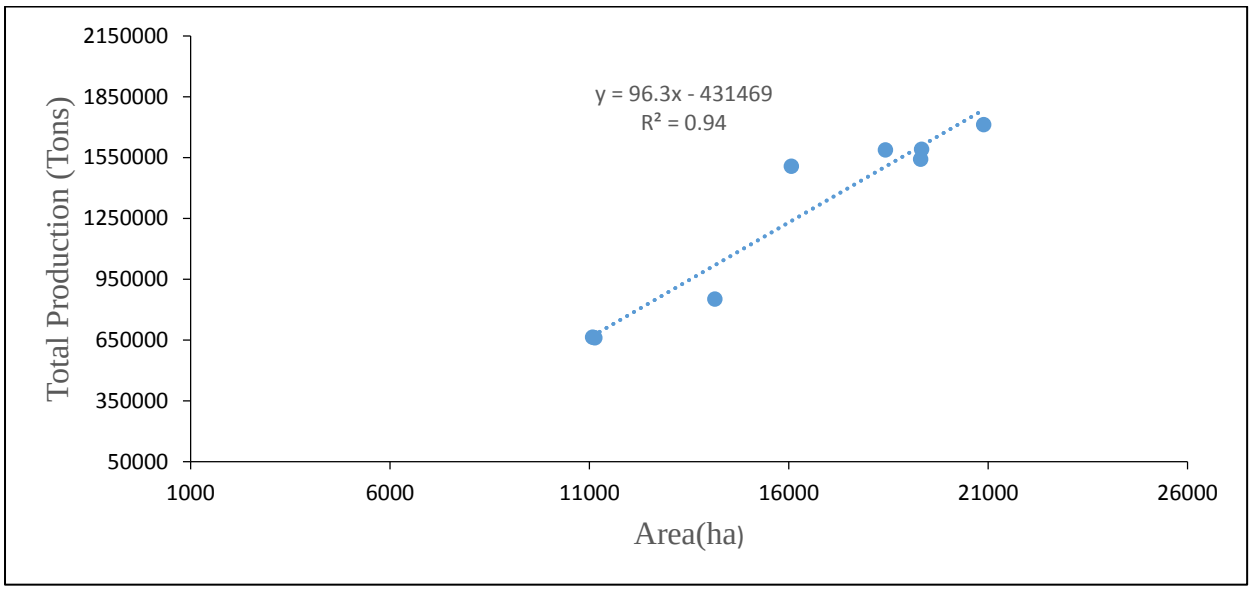

Figure 4.18: Relation between the area under rice and total production in Fogera wereda reported by Fogera wereda Agricultural and Rural Development Office from 2007 to 2016.

4.2 Discussion

The use of Sentinel 1 RADAR C-band microwave image in rice mapping and monitoring has various advantages. In the first place, the energy from the radar signals can penetrate through the cloud and rainfall. Its ability to detect features at day and night is another instance of the preferability of using the microwave technology for high cloud prone areas. Sentinel 1 RADAR data create a new opportunity for agricultural land monitoring at finer spatiotemporal scales. These new generation Sentinel 1 RADAR data have been tested in rice and other land use type monitoring (Nguyen *et al*., 2016, Shao *et al.,* 2016, Torbick *et al.,* 2017). In this study, new C-band like and cross-polarization (VV and VH) Sentinel 1 RADAR with the Sentinel 2 data was used to monitor rice fields in Fogera wereda, Ethiopia, during the 2017 growing season. The temporal backscatter values of rice are determined by rice growth phase and conditions. Additionally, differences in a variety of rice and management practice result in differences in rice growth and temporal backscatter. Therefore, applying the temporal backscatter difference as a classification method, a major source of uncertainty could arise mainly due to different radar backscatter response patterns between fields. This demands the use of time series Sentinel 1 RADAR data, that would capture even subtle changes in backscatter values between paddy fields.

In this study, six temporal images of Sentinel 1 RADAR data have employed, covering a part of the rice-growing season (sowing to ripening) in which marked the difference in backscatter profiles are most pronounced. In this study, the observed temporal backscatter values at the VV Sentinel 1 RADAR polarization are higher for all land use types, this work is comparable with investigations done by (Wang *et al.,* 2010, Wu *et al.,* 2011). However, the VH Sentinel 1 RADAR polarization showed the most sustained increase in backscatter profile of rice compared to VV except 01 August high flooding imaging date. VH backscatter of rice sharply decreased during 01 August imaging date, increasing sharply on 25 August and decreasing slightly at ripening growth stage. The VV channel shows relatively linear backscatter profile of rice at periods equivalent to the rice growing stage. Using the classes separability measures reported in (Townsend *et al.,* 2001), the Sentinel 1 RADAR VH polarization have an overall better performance in separating the investigated land-cover types. Hence, given its more sustained increase in temporal backscatter with rice with the exception of 01 August Sentinel 1 RADAR VH images and its better two-class signature separability, the Sentinel 1 RADAR VH polarization was observed optimal for this study, and whose temporal image data were used in subsequent analysis. In addition, Sentinel 1 RADAR images (both VV/VH) data was tested to

identify the optimal polarization in a similar area with that of the study area (Aneded and Bahir Dar Zuriya weredas) which is comparable with investigations done in this study.

Water showed the lowest temporal backscatter in this study, water surface has a specular reflectance property as the transmitted signal is reflected away from the SAR sensor (Zhou *et al.*, 2014, Getu Tessema, 2017). Built up showed the highest temporal backscatter values, which is largely attributed to corner reflection effects of constructions (Wang *et al.*, 2010). Trees also showed high temporal backscatter values second only to built up.

The first paddy rice mapping results presented are only based on 14 June VH image from Sentinel 1 RADAR data, which is during rice sowing period. This mapping was employed using CART classification method, the paddy rice mapping during sowing exclude late planting rice. The resultant land use map from this approach shows high misclassifications of rice and the other land-cover types. The second paddy rice mapping presented in this study is only based on 01 August VH images from Sentinel 1 RADAR data. Mapping paddy rice using 20 July, 25 August, 30 September and 12 October was not possible, mainly due to high overlap between rice and the other land-cover types in the study area. The paddy rice mapping during high flooding stage includes late-planted rice. Even though most validation rice crop pixels were correctly classified using 01 August VH images, there were some commission errors in this land use types. Several water pixels have been misclassified as rice. An increase in surface roughness, which could be brought by moving wind, could increase the backscatter profile of a given pixel between Sentinel 1 RADAR acquisitions (Bouvet *et al.*, 2011). High confusions also exist between built up and trees, this indicates the application of Sentinel 1 RADAR images for the identification of built up and trees is poor in this study area. This is due to the material used for the construction of built up in the study area is mostly mud, which may result in similar backscatter value like trees. In addition, non-rice crops confused highly with trees. The application of Sentinel 1 RADAR images for mapping and monitoring of built up, trees and non-rice crops is not promising in the result found this study area. In maps prepared by Sentinel 1 RADAR shows the large area covered by trees, a condition that is very unlikely in the study area. 23 points of test data of the class built up have been misclassified as trees. In order to reduce some of these confusions, the combined use temporal VH RADAR data with the NDVI and MNDWI indices. The introduction of the above-mentioned optical indices into the mapping algorithm brought a substantial reduction in inter-class misclassification as evident in the corresponding producer's and user's accuracies. In the rice land use types, these optical indices reduced most omission errors derived from the commission in the non-rice crop classes. In Table 4.5 and 4.6, 6 of the commission errors in the rice class are accounted for by the class water. It is assumed that at 09 October (date

of optical image), rice plants in the study area have acquired surface area for NDVI to be greater than or equal to 0.1, but less than 0.3. The use of the condition, NDVI greater than or equal 0.5, slightly reduced the commission errors in trees and hence, an overall slight increase in the classification accuracy of trees and built up is shown. It can be observed that the areas initially misclassified as trees in Figure 4.7 and 4.9 have been classified as built up and others in Figure 4.11. This is quite agreeable; the class others occupy a larger percentage in the study area Table 4.12. As the major focus of this research is paddy rice mapping, it is important to look the relative advantages of the two mapping algorithms in identifying rice fields. With the integration of optical indices, there is a slight increase in the producer accuracy of rice but a substantial increase in its user accuracy, compared to test data of optimal Sentinel 1 RADAR accuracy. This research study proposed that a pixel is classified as rice when it meets the temporal backscatter value criterion, while having NDVI values greater than or equal to 0.1, but less than 0.3. With the integration of Sentinel 1 RADAR VH images with the single-date Sentinel 2 NDVI and MNDWI indices, there is a considerable increase in the accuracy of rice land use and the decrease of commission and omission errors in non-rice land use types brought a high increase in overall land-cover classification accuracy. Mapping inundation area of the study using time series Sentinel 1 RADAR VH optimal node and inundation area generated by integrating Sentinel 1 RADAR VH images and Sentinel 2 indices (MNDWI) map was compared. The refined inundated area generated by time series Sentinel 1 RADAR VH images show better overall accuracy. This is mainly due to the ability of C-band Sentinel-1 SAR in the mapping of inundation below full or dense crop canopies (Schlaffer *et al.*, 2015). The satellite-based monitoring of rice and other crops is of prime importance in Fogera wereda as well as in countries with rice cultivation and has a number of advantages compared to assessments solely based on ground data collection. The all-weather capability, active sensing system that operates independently of sun illumination of Sentinel 1 RADAR satellite allows wall-to-wall coverage of the province and includes hard-to-access areas. For production assessment, a linear regression model was developed. If the value of (R^2) obtained is greater than 0.5 then the relation between the response variable and the explanatory variable is quite high (Sellam and Poovammal, 2016). Based on the model a positive and strong relationship with a coefficient of determination (R^2) of 0.94 was obtained.

CHAPTER FIVE

5. Conclusion and Recommendations

5.1 Conclusion

Rice production forming an integral part in meeting global food demands, it is important to not only monitor rice cultivation at large scales, but also those at relatively smaller scales such as in Fogera wereda. In an attempt to fill some of the knowledge gaps in agricultural mapping and monitoring in Fogera landscapes, this study is conducted to test the potential of the new Sentinel 1 RADAR images in rice mapping and monitoring during the high cloudy season, which is even not thinkable to find cloud-free optical images during Kiremit (June, July and August) season in the study area. In addition, this study tests the potential of integrating the new Sentinel 1 RADAR images with Sentinel 2 optical indices for refining rice field.

Total six-scene Sentinel 1 RADAR(VV/VH) images covering a period from June to October 2017 are tested for the identification of optimal polarization and mapping after preprocessing.

The VH polarization of Sentinel 1 RADAR to be the optimal polarization for rice field mapping as it exhibited the most sustained increase in the temporal backscatter of rice, relative to the nearly uniform temporal backscatter profiles of the other land-cover classes like rice. Using a two-class separability measure, the VH polarization showed better inter-class discrimination ability and was thus combined with NDVI and MNDWI images in the proposed rice mapping algorithm. CART model was used for the identification optimal node and mapping paddy fields. The paddy fields extracted from CART optimal node was 20,911.2 ha for 14 June 2017 and 19,892.5 ha for 01 August 2017 growing seasons. Other imaging dates of Sentinel 1 RADAR VH images were not used for rice mapping, mainly due to high backscatter value overlap between rice and the other land-cover types. The introduction of NDVI and MNDWI, increase the overall classification accuracy from CART test validation of Sentinel 1 RADAR VH image data 69.9% to 79.5%, and the Kappa statistic from 0.62 to 0.76. This increase in overall classification accuracy by (9.6%) has demonstrated the added value of cloud masked optical data to the more available radar data in cloud-prone tropics for land-cover mapping. The result also shows that using more temporal optical data, the potential of Sentinel 1 RADAR data in paddy rice mapping will be fully realized. The increase in rice user's accuracy (reduction in commission errors) compared to CART test validation with the addition of the two optical indices confirms the operational applicability of integrating the new Sentinel 1 RADAR data with optical data is a robust method for rice mapping in tropical and highly heterogeneous landscapes.

Even though, this study has only mapped rice fields at different rice growth stage, including mapping inundation that results refine rice extent a single time point (2017), results could be instrumental in updating previous records while providing a basis for revealing the spatiotemporal dynamics of rice cultivation in Fogera wereda and its potential impacts on food availability, water resource utilization, and land-use management. This study could be regarded as one of, if not the first, to test the operational applicability of integrating the new Sentinel 1 RADAR data with Sentinel 2 optical indices for mapping smallholder rice fields in Fogera at a wereda scale, providing details of individual rice field boundaries. Moreover, this study has shown the VH polarization to increase sharply after planting and decrease highly at high flooding, demonstrates the potential of Sentinel 1 RADAR in monitoring other rice biophysical parameters that show similar temporal behaviors such as above ground biomass and leaf area index. Hence, this scientific contribution would be of much interest to the agricultural remote sensing community.

This study investigates the application of remote sensing technology to monitor rice crop and the final refined rice field accounts 19,157.8 ha, with 2,947.2 ha difference from the area estimated by Fogera wereda Agricultural and Rural Development Office. Monitoring paddy fields through the different date of mapping reduced uncertainties occurred on rice crop in one growing season. A positive and strong relationship with a coefficient of determination (R^2) of 0.94 was observed between the cultivated rice area and total production of the growing season for the years 2007 to 2016.

5.2 Recommendations

The present study has analyzed and evaluated Sentinel 2 Optical and Sentinel 1 RADAR images for monitoring of rice crops. Based on the findings of the study, the following recommendations have been drawn for future works in the so-called field of study.

- To preprocess Sentinel 1 RADAR images a high processing speed computer (at least 6 GB RAM), strong internet connection and new version image processing software is required.
- Polarization is one of the decisive factors in the analysis of the Sentinel 1 RADAR images for extraction of rice area. The present study used the VV and VH mode of polarization which in some extent lacks detection of the full rice extent. Although the results from the optimal VH polarization were promising, it could be better to use HH polarization (if available) than VH. The mode (HH) can fully capture the rice extent by its capability of horizontal transmission and horizontal reception of SAR signals.

- Paddy rice mapping using Sentinel 1 RADAR VH polarization was done by using CART model. For operational purposes, this rice mapping algorithm needs to be further investigated for other crops and at other weredas in Ethiopia, where the cultivation systems may be different.
- The RADAR image is not easy to analyze and interpret, further research should be conducted using the improved method and more advanced image classification algorithms.
- In the study area, rice agricultural activities like the ploughing, seeding, harvest start at a different time which depends on most rainfall conditions and farmer's time schedule due to this reason denser time-series Sentinel 1 RADAR data should be analyzed in order to monitor rice crop.
- For mapping inundation, Sentinel 1 RADAR VH polarization data is by far better than optical data, in addition to all weather penetration capability.

References

Aboelghar, M., Arafat, S., Abo Yousef, M., El-Shirbeny, M., Naeem, S., Massoud, A., and Saleh. N. (2011). Using SPOT data and leaf area index for rice yield estimation in Egyptian Nile delta. *The Egyptian Journal of Remote Sensing and Space Sciences.*1**4** (2): 81−89.

Akbari, V. (2013). *Multitemporal Analysis of Multipolarization Synthetic Aperture Radar Image for Robust Surface Change Detection*. University of Toronto, Canada, 256 pp.

Al-Ali, Mohamed. (2011). Assessment of high resolution SAR imagery for mapping food plain water bodies: A comparison between radarsat-2 and TerraSAR-X, Unpublished PhD Thesis, Durham theses, Durham University, 264 pp.

Argenti, F., Lapini, A., Bianchi T., and Alparone, T. (2013). A tutorial on speckle reduction in synthetic aperture radar images. *Geosci. Remote Sens.* **1 (**3): 6 −35.

Astewul Takele. (2010). Analysis of rice profitability and marketing chain: the case of Fogera Woreda, South Gonder zone, Amhara National Regional State, Ethiopia. Unpublished MSc Thesis, Haramaya University, Haramaya, Ethiopia.118pp.

Babu, M., Subramanyam, M.V., and Prasad, G. (2013). Effect of speckle filtering on SAR high resolution data for image fusion. *International Journal of Engineering and Innovative,* **3 (**1): 143−153.

Bakker, W.H., Janssen, L.F., Werir, J.C., Gorte, H.G., Pohl, C., Woldai, T., Horn, A.J.and Reeves, C.V. (2001). *Principle of Remote Sensing*. International Institute for aerospace survey and earth science(ITC), Enschede,170pp.

Balzter, H., Cole, B., Thiel, C., and Christiane, S. (2015). Mapping CORINE Land Cover from Sentinel-1A SAR and SRTM Digital Elevation Model Data using Random Forests. *Remote Sens. **7** (11)*: 14876-14898.

Ban, Y. (2003). Synergy of multitemporal ERS-1 SAR and Landsat TM data for classification of agricultural crops. *Can. J. Remote Sens.* **29** (4): 518–526.

Blaes, X., Vanhalle, L., and Defourny, P. (2005). Efficiency of crop identification based on optical and SAR image time series. *Remote Sens. Environ*. **96** (3): 352–365.

Bartsch, A., Trofaier, A. M., Hayman, G., Sabel, D., Schlaffer, S., Clark, D. B and Blyth, E. (2012). Detection of open water dynamics with ENVISAT ASAR in support of land surface modeling at high latitudes. *Bio-geosciences*, **9** (7): 703−714.

Batterham, P.J., Christensen, H., and Mackinnon, A.J. (2009). Modifiable risk factors predicting major depressive disorder at four-year follow-up: a decision tree approach. *BMC Psychiatry*. **9** (75): 1-15.

Bouvet, A., and Le Toan, T. (2011). Use of ENVISAT/ASAR wide-swath data for timely rice fields mapping in the Mekong River Delta. *Remote Sens. Environ*. **115** (4): 1090–1101.

Calla, O.P.N. (2013). Applications of microwave in remote sensing. *Indian Journal of Radio and Space Physics (IJRSP).* **19**: 343−358.

CCRS. (2013). *Fundamentals of remote sensing*. Natural Resource, Canada. 258pp.

Central Statistical Agency (CSA). (2007, 2014-2017). Summary and statistical report of the 2007, and 2014-2017 population and housing census. Addis Ababa: Central Statistical Agency.

Chang, K.W., Shen, Y., and Lo, J.C. (2005). Predicting rice yield using canopy reflectance measured at booting stage. *Agron. J.* **97** (3): 872–878.

Choudhury, I., And Chakraborty, M. (2005). SAR signature investigation of rice crop using RADARSAT data. *Int. J. Remote Sens* .***3 (****27):*519–534.

Dawe, D., Pandey, S., and Nelson, A. (2010). Emerging trends and spatial patterns of rice production. In Rice in the Global Economy: Strategic Research and Policy Issues for Food Security; *International Rice Research Institute (IRRI):* Los Baños, Philippines.35pp.

Dekker, R.J. (1997). SAR change detection techniques and applications. *Int. J. Remote Sens.* **19 (**6): 1133 -1146.

Dorigo, W., De Jeu, R., Chung, D., Parinussa, R., Liu, Y., Wagner, W., and Fernandez-Prieto, D. (2012). Evaluating global trends (1988–2010) in homogenized remotely sensed surface soil moisture. *Geophys. Res. Lett*. **39:** 1-7.

D'Urso, G., Richter, K., Calera, A., Osann, M.A., Escadafal, R., Garatuza-Pajan, J., Hanich, L., Perdigão, A., Tapia, J.B., and Vuolo, F. (2010). Earth Observation products for operational irrigation management in the context of the PLEIADeSproject. *Agric. Water Manag.* **98** (2): 271–282.

Eastman, J. R. (2003). *IDRISI Kilimanjaro Guide to GIS and Image Processing*. Clark University Worcester, MA, USA, 306 pp.

Food and Agriculture Organization of the United Nations. Available online: http://www.fao.org/home/en (accessed on 12 January 2018).

FAO. (2007). Digital Soil Map of the World. Available online: version 3.6. http://www.fao.org/geonetwork/srv/en/metadata.show?id=14116

Gerald, F., Christopher, C., Michael, T., Tobias, U., and Evence, Z. (2014). Integration of Optical and Synthetic Aperture Radar Imagery for Improving Crop Mapping in Northwestern Benin, West Africa. *Remote Sens*. ***6*** *(7)*: 6472-6499.

Getachew Afework. (2000). Rice adaptation in Metema Woreda North Gondar one of the Amhara Regional State. Unpublished technical report, Bureau of Agriculture, Bahir Dar, Ethiopia, 110 pp.

Getu Tessema. (2017). Flood detection and mapping using microwave remote sensing; a case study on lake Koka catchment, Awash River Basin, Ethiopia. Unpublished MSc Thesis, Addis Ababa University, Addis Ababa, Ethiopia. 83pp.

Hagen, S., Heilman, P., Marsett, R., Torbick, N., Salas, W., Ravensway, J., and Qi, J. (2012) Mapping total vegetation cover across western rangelands with MODIS data. Rangel. *Ecol. Manag.* **65** (5): 456–467.

Henderson, H.A., and Lewis, A.J. (1998*). Principles and Applications of Imaging Radar*. John Wiley and Sons. 103pp.

Hunt, E.B, Marin, J. and Stone, P.T. (1996). *Experiments in Induction*; Academic Press, New York.125 pp.

Immitzer, M., Vuolo, F., and Atzberger, C. (2016). First Experience with Sentinel-2 Data for Crop and Tree Species Classifications in Central Europe. *Remote Sens.* **8** (166):1-27

Inglada, J., Vincent, A., Arias, M., and Marais-Sicre, C. (2016). Improved Early Crop Type Identification by Joint Use of High Temporal Resolution SAR and Optical Image Time Series. *Remote Sens.* **8** (5): 1–21.

Inoue, Y., Sakaiya, E., and Wang, C. (2014). Capability of C-band backscattering coefficients from high-resolution satellite SAR sensors to assess biophysical variables in paddy rice. *Remote Sens. Environ.* **140:** 257–266.

Kontgis, C., Schneider, A., and Ozdogan, M. (2015). Mapping rice paddy extent and intensification in the Vietnamese Mekong River Delta with dense time stacks of Landsat data. *Remote Sens. Environ.* **169:** 255–269.

Koppe, W., Gnyp, M.L., Hutt, C., Yao, Y., Miao, Y., Chen, X. and Bareth, G. (2013). Rice monitoring with multi-temporal and dual-polarimetric TerraSAR-X data. *International Journal of Applied Earth Observation and Geoinformation*. **21:** 568–576.

Kuenzer, C. and Knauer, K. (2013). Remote sensing of rice crop areas. *Int. J. Remote Sens.* **34** (6): 2101–2139.

Le-toan, T., Laur, H., Mougin, E. and Lopes, A. (1989). Multitemporal and dual-polarization observations of agriculture vegetation covers by X-band SAR images. *IEEE Trans. Geosci. Remote Sensing.* **27** (6): 709-717.

Liang, S. (2004). *Quantitative Remote Sensing of Land Surfaces.* Wiley, New Jersey, 501pp.

Li, C., Gluer C.C., Eastell, R., Felsenberg, D., Reid, D.M., Rox, D.M., and Lu, Y. (2012). Tree-structured subgroup analysis of receiver operating characteristic curves for diagnostic tests. *Acad Radiol.* **19** (12): 1529-1536.

Lin, H., Chen, J., Pei, Z., Zhang, S., and Hu, X. (2009). Monitoring sugarcane growth using ENVISAT ASAR data. *IEEE Trans. Geosci. Remote Sens*. **47** (8): 2572–2580.

Lo, L. P., and Yeung, K. W. (2005). *Concepts and Techniques of Geographic Information System*. Prentice-Hall of India Private Limited, New Delhi, 492 pp.

Lopez-Sanchez, J.M., Ballester-Berman, J.D., and Hajnsek, I. (2011). First results of rice monitoring practices in Spain by means of time series of TerraSAR-X dual-pol images. *IEEE J. Sel. Top. Appl. Earth Obs. Remote Sens.* **4:** 1–11.

Lu D., Mausel P., Brondizio, E. and E. Moran, E. (2004). Change detection techniques. *Int. J. Remote Sensing.* **25 (**12): 2365–2407.

Mansaray, L.R., Huang, W., Zhang, D., Huang, J. and Li, J. (2017). Mapping Rice Fields in Urban Shanghai, Southeast China, Using Sentinel-1A and Landsat 8 Datasets. *Remote Sens.***9 (**3): 1-23.

Martinis, S. and Rieke, C. (2015). Backscatter analysis using multi-temporal and multi-frequency SAR Data in the Context of Flood Mapping at River Saale. *Int. J. Remote Sens.* **7 (**5): 7733−7752.

McNairn, H., Champagne, C., Shang, J., Holmstrom, D., and Reichert, G. (2009). Integration of optical and Synthetic Aperture Radar (SAR) imagery for delivering operational annual crop inventories. *ISPRS J. Photogramm. Remote Sens.* **64** (5): 434–449.

Michael, J.H., Ticehurst, C.J Lee, J.S., Grunes, M.R., Donald, G.E., and Henry, D. (2005). Integration of optical and radar classifications for mapping pasture type in Western Australia. *IEEE Trans. Geosci. Remote Sens.* **43** (7): 1665–1681.

Navarro, A., Rolim., J., Miguel, I., Catalão, J., Silva, J., Painho, M., and Zoltán., V. (2016). Crop Monitoring Based on SPOT-5 Take-5 and Sentinel-1A Data for the Estimation of Crop Water Requirements. *Remote Sens.* **8 (**6): 1-20.

Nelson, A., Setiyono, T., Rala, A.B., Quicho, E.D., Raviz, J.V., Abonete, P.J., Maunahan, A.A., Garcia, C.A., Bhatti, H.Z.M., and Villano, L.S. (2014). Towards an Operational SAR-Based Rice Monitoring System in Asia: Examples from 13 Demonstration Sites across Asia in the RIICE Project. *Remote Sens.* **6** (11): 10773–10812.

Nguyen, B.A., Clauss, K., Cao, S., Naeimi, V., Kuenzer, C., and Wagner, W. (2015). Mapping rice seasonality in the Mekong Delta with Multi-Year Envisat ASAR WSM Data. *Remote Sens*. **7** (12): 15868–15893.

Nguyen, B.A., and Wagner, W. (2017). European Rice Cropland Mapping with Sentinel-1 Data: The Mediterranean Region Case Study. *Water*. **6 (**9): 1-26.

Nguyen Lam-Dao, *M*. (2009). Rice Crop Monitoring using new generation synthetic aperture radar (SAR) imagery. Unpublished Ph.D. Thesis, University of Southern Queensland, Queensland, Australia.163pp.

Phuong, L.T., Venkatesh, R., Khang, N., Phung, P., & Nguyen, L. (2016). Analysis of Sentinel -1 SAR data for mapping rice crop in the Mekong Delta, Vietnam. **In:** *International Conference on Geoinformatics for Spatial-Infrastructure Development in Earth & Allied Sciences (GIS-IDEAS)*, pp. 1-5. Osaka. Japan.

Reddy, S.R. (2004). *Agronomy of field crops*. Department of Agronomy ANGR Agricultural University SV Agriculture College, India,136pp.

Rogan, J., Miller, J., Stow, D., Franklin, J., Levien, L., and Fischer, C. (2003). Land-cover change monitoring with classification trees using Landsat TM and ancillary data. *Photogramm. Eng. Remote Sens*. **69** (7): 793–804.

Sanyal, J. and Lu, X. X. (2004). Application of remote sensing in flood management with special reference to monsoon Asia: A review, *Natural Hazards.* **33** (2): 283−301.

Sarmap. (2009). Synthetic aperture radar and sarscape - SAR guidebook, 120 pp.

Schlaffer S., Matgen P., Hollaus M. and Wagner W. (2015). Flood detection from multi-temporal SAR data using harmonic analysis and change detection. *Int.J. Appl. Earth Obs Geoinf.* **38:**15–24.

Sellam, J. and Poovammal.v. (2016). Prediction of Crop Yield using Regression Analysis. *Indian Journal of Science and Technology*. ***38** (9):1-5.*

Shao, Y., and Lunetta, R.S. (2012). Comparison of support vector machine, neural network, and CART algorithms for the land-cover classification using limited training data points. *ISPRS J. Photogramm. Remote Sens*. **70:** 78–87.

Shao, Z., Fu, H., Fu, P., and Yin, L. (2016). Mapping Urban Impervious Surface by Fusing Optical and SAR Data at the Decision Level. *Remote Sens.* **52** (8): 1-21.

Shen, S., Yang, S., Li, B., Tan, B., Li, Z., and Le Toan, T. (2009). A scheme for regional rice yield estimation using ENVISAT ASAR data. *Sci. China Ser. D Earth Sci.* **52:**1183–1194.

Shi, J., Dozier, J., and Rott, H. (1994). Snow mapping in alpine regions with synthetic aperture radar. *IEEE Trans. Geosci. Remote Sens.* **32** (1): 152–158.

Skakun, S., Kussul, N., Shelestov, A.Y., Lavreniuk, M., and Kussul, O. (2015). Efficiency assessment of multitemporal C-band Radarsat-2 intensity and Landsat-8 surface reflectance satellite imagery for crop classification in Ukraine. *IEEE J. Sel. Top. Appl.* **9** (8):3712 – 3719.

Skolnik, M. I. (2008). *Radar Handbook*. The McGraw-Hill, USA, New York, 1351 pp.

Tilahun Gebey, Kahsay Berhe, Dirk Hoekstra and Bogale Alemu. (2012). Rice value chain development in Fogera woreda based on the IPMS experience. *International Livestock Research Institute (ILRI)*.1-31.

Torbick, N., Chowdhury, D., Salas, W., and Qi, J. (2017). Monitoring rice agriculture across Myanmar using time series Sentinel-1 assisted by Landsat 8 and PALSAR 2. *Remote Sens.* **9** (2): 1-22.

Torbick, N., and Salas, W. (2014). Mapping agricultural wetlands in the Sacramento Valley, USA with satellite remote sensing. *Wetl. Ecol. Manag.* **23** (1): 79–94.

Townsend, P.A. (2001). Mapping seasonal flooding in forested wetlands using multi-temporal Radarsat SAR. Photogramm. *Eng. Remote Sens.* **67** (7): 857–864.

Veloso, A., Mermo, S., Bouvet, A., Le Toan, T., Planells, M., Dejoux.J. F and Eric, C. (2017). Understanding the temporal behavior of crops using Sentinel-1 and Sentinel-2-like data for agricultural applications. *Remote Sens. Environ.* ***199****:* 415–426.

Vivone, G., Alparone, L., Chanussot, J., Dalla Mura, M., Garzelli, A., Licciardi, G.A., Restaino, R., and Wald, L. (2015). A critical comparison among pansharpening algorithms. IEEE Trans. Geosci. *Remote Sens*. **53** (5): 2565–2586.

Waldner, F., Lambert, M. J., Li, W., Weiss, M., Demarez, V., Morin, D., Marais-Sicre, C., Hagolle, O., Baret, F., and Defourny, P. (2015). Land cover and crop type classification along the season based on biophysical variables retrieved from multi-sensor high-resolution time series. *Remote Sens.* **7** (8): 10400–10424.

Wang, D., Lin, H., Chen, J., Zhang, Y., and Zeng, Q. (2010). Application of multi-temporal ENVISAT ASAR data to agricultural area mapping in the Pearl River Delta. *Int. J. Remote Sens.* **31** (6): 1555–1572.

Wu, F., Wang, C., Zhang, H., Zhang, B., and Tang, Y. (2011). Rice crop monitoring in South China with RADARSAT-2 quad-polarization SAR data. *IEEE Geosci. Remote Sens. Lett.* **8** (2): 196–200.

Yonezawa, C., Negishi, M., Azuma, K., Watanabe, M., Ishitsuka, N., Ogawa, S., and Saito, G. (2012). Growth monitoring and classification of rice fields using multitemporal RADARSAT-2 full-polarimetric data. *Int. J. Remote Sens.***33** (18): 5696–5711.

Yun, D., Yihang, Z., Feng, L., Qunming, W., Wenbo, Li., and Xiaodong, L. (2016). Water Bodies' Mapping from Sentinel-2 Imagery with Modified Normalized Difference Water Index at 10-m Spatial Resolution Produced by Sharpening the SWIR Band. *Remote Sens. **8** (4):1-19.*

Yun, S., Xiangtao, F., Hao, L., Jianhua, X., Ross, S., Brisco, B., Brown, R., and Staples, G. (2001). Rice monitoring and production estimation using multitemporal RADARSAT. *Remote Sens. Environ*. **76** (3): 310–325.

Zhang, Y., Wang, C., Wu, J., Qi, J., and Salas, W.A. (2009). Mapping paddy rice with multitemporal ALOS/PALSAR imagery in southeast China. *Int. J. Remote Sens.* **30** (23): 6301–6315

Zhou, Y., Xiao, X., Qin, Y., Dong, J., Zhang, G., Kou, W., Jin, C., Wang, J., and Li, X. (2014). Mapping paddy rice planting area in rice-wetland coexistent areas through analysis of Landsat 8 OLI and MODIS images. *Int. J. Appl. Earth Obs.* **46:** 1–12.

Appendices

Annex I: Confusion Matrix developed by CART model.

Confusion Matrix – Learn

	Actual Class	Total Class	Percent Correct	Predicted Classes				
				rice N = 76	water N = 33	built N = 46	trees N = 83	non rice crops N = 81
	rice	93	79.57%	74	0	0	1	18
	water	38	86.84%	1	33	0	3	1
	built	70	51.43%	0	0	36	24	10
	trees	66	74.24%	1	0	9	49	7
	non rice crops	52	86.54%	0	0	1	6	45
	Total:	319						
	Average:		75.72%					
	Overall % Correct:		74.29%					

Confusion Matrix – Test

	Actual Class	Total Class	Percent Correct	Predicted Classes				
				rice N = 65	water N = 37	built N = 51	trees N = 68	non rice crops N = 71
	rice	76	81.58%	62	0	0	2	12
	water	40	92.50%	0	37	0	3	0
	built	70	48.57%	1	0	34	23	12
	trees	60	58.33%	0	0	14	35	11
	non rice crops	46	78.26%	2	0	3	5	36
	Total:	292						
	Average:		71.85%					
	Overall % Correct:		69.86%					

Misclassification – Learn

Class	N Cases	N Mis-Classed	Pct. Error	Cost
rice	93	19	20.43%	0.20430
water	38	5	13.16%	0.13158
built	70	34	48.57%	0.48571
trees	66	17	25.76%	0.25758
non rice crops	52	7	13.46%	0.13462

Misclassification – Test

	Class		N Cases	N Mis-Classed	Pct. Error	Cost
	rice		76	14	18.42%	0.18421
	water		40	3	7.50%	0.07500
	built		70	36	51.43%	0.51429
	trees		60	25	41.67%	0.41667
	non rice crops		46	10	21.74%	0.21739

Annex II: The extracted backscatter (σ^0) value of rice crop at six imaging date of Sentinel 1 RADAR VH images.

b1_Stacked	b2_Stacked	b3_Stacked	b4_Stacked	b5_Stacked	b6_Stacked
-21.66	-16.11	-43.09	-16.64	-16.56	-18.76
-20.54	-22.48	-51.24	-24.30	-22.36	-17.88
-19.28	-23.03	-50.98	-19.58	-19.94	-17.27
-19.74	-16.94	-45.27	-16.80	-17.19	-20.43
-19.13	-19.25	-50.20	-19.07	-15.73	-15.50
-19.48	-17.62	-49.46	-19.17	-15.74	-16.46
-19.00	-20.53	-49.86	-22.82	-18.24	-20.32
-18.97	-20.47	-48.68	-24.21	-21.34	-18.87
-20.52	-17.30	-49.92	-23.11	-18.63	-18.38
-20.98	-17.53	-43.24	-15.64	-16.69	-15.26
-18.78	-21.16	-51.07	-18.44	-18.97	-16.70
-19.40	-21.53	-51.03	-17.95	-18.90	-16.86
-20.31	-20.11	-52.46	-18.71	-19.25	-16.97
-20.98	-22.25	-52.43	-20.08	-19.49	-16.38
-20.17	-19.98	-48.78	-20.56	-15.99	-16.65
-20.31	-25.20	-53.38	-21.53	-16.21	-17.40
-19.18	-22.60	-50.97	-18.86	-15.41	-16.67
-20.16	-17.78	-47.35	-20.95	-16.34	-18.04
-17.62	-19.44	-49.80	-20.08	-16.51	-15.76
-20.14	-21.04	-48.50	-18.18	-16.49	-17.67
-19.37	-20.96	-47.75	-19.05	-15.74	-17.68
-18.66	-21.59	-50.33	-21.83	-15.21	-15.77
-17.79	-21.19	-51.06	-20.10	-15.38	-18.27
-21.13	-21.17	-45.29	-18.08	-15.15	-17.01
-20.66	-21.37	-45.54	-18.54	-17.85	-17.98
-19.84	-22.36	-51.01	-19.02	-13.44	-16.46
-21.06	-19.13	-44.71	-16.00	-15.82	-16.90
-19.82	-19.53	-47.00	-16.41	-15.70	-16.37

-20.31	-25.66	-50.58	-19.75	-17.69	-18.10
-19.94	-20.17	-49.88	-16.25	-17.61	-18.18
-19.70	-21.28	-49.40	-19.03	-15.81	-15.72
-20.39	-20.63	-48.80	-19.14	-18.74	-15.88
-21.09	-19.34	-51.66	-22.40	-16.80	-19.90
-18.54	-19.18	-45.37	-16.34	-14.91	-15.39
-20.10	-19.50	-49.14	-18.46	-15.83	-16.73
-18.63	-19.16	-46.32	-16.84	-15.70	-19.38
-20.65	-22.06	-50.87	-20.19	-17.65	-14.40
-23.51	-21.64	-47.71	-18.13	-15.99	-19.11
-21.85	-16.97	-48.65	-17.35	-17.37	-19.84
-20.21	-19.33	-45.43	-16.88	-16.46	-16.24
-18.76	-21.95	-50.76	-19.06	-17.12	-17.20
-20.81	-22.66	-53.85	-19.04	-16.68	-15.45
-18.29	-14.99	-47.43	-21.73	-15.95	-17.37
-20.20	-18.67	-49.76	-19.47	-16.34	-16.51
-19.19	-21.06	-49.21	-20.04	-14.52	-17.73
-21.78	-18.75	-43.30	-16.59	-15.77	-14.49
-21.25	-17.56	-43.33	-16.09	-16.47	-14.18
-21.75	-20.21	-44.81	-17.74	-16.36	-15.05
-19.62	-17.54	-44.89	-16.47	-17.42	-15.54
-19.34	-25.36	-47.92	-17.22	-20.08	-17.38
-19.12	-20.15	-47.13	-16.45	-16.04	-16.14
-19.38	-18.22	-48.80	-17.78	-17.79	-16.56
-19.03	-23.01	-48.03	-17.63	-19.66	-26.57
-18.87	-25.99	-49.74	-18.33	-16.76	-27.36
-19.66	-21.63	-51.59	-19.40	-15.68	-17.69
-18.95	-25.13	-51.94	-20.90	-20.54	-22.72
-19.46	-19.37	-50.23	-16.86	-17.61	-15.09
-19.32	-18.94	-47.97	-16.46	-18.63	-18.82
-16.52	-22.98	-52.93	-15.42	-16.93	-21.79
-20.44	-18.42	-50.88	-17.80	-16.45	-14.49

-21.79	-19.39	-50.17	-20.08	-16.83	-17.59
-23.74	-22.76	-51.85	-20.67	-16.94	-15.05
-19.24	-18.98	-51.45	-17.67	-17.08	-15.82
-19.67	-22.46	-51.30	-18.84	-15.61	-16.58
-20.45	-21.60	-51.58	-17.68	-17.61	-16.44
-18.95	-21.66	-52.94	-20.26	-16.82	-16.86
-20.19	-16.58	-48.62	-17.68	-17.83	-16.56
-17.10	-21.43	-50.09	-20.08	-16.76	-15.89
-22.33	-17.53	-48.95	-16.84	-16.38	-16.79
-18.21	-18.94	-49.91	-19.02	-17.74	-15.74
-19.89	-22.58	-49.68	-19.06	-15.98	-16.90
-18.51	-16.68	-50.80	-19.43	-16.51	-17.99
-22.65	-18.09	-46.28	-16.98	-15.25	-16.46
-21.43	-14.63	-45.08	-15.79	-14.52	-16.78
-22.12	-17.29	-44.47	-16.22	-15.21	-17.41
-19.74	-19.08	-49.27	-16.76	-16.99	-16.76
-19.10	-15.69	-48.71	-18.18	-16.25	-17.08
-19.99	-16.96	-49.10	-19.43	-14.79	-16.95
-19.44	-18.86	-51.84	-17.77	-17.55	-17.10
-19.98	-15.49	-45.41	-18.38	-15.71	-16.11
-18.42	-17.45	-49.12	-17.99	-17.20	-17.10
-19.65	-18.61	-49.07	-17.21	-15.85	-16.29
-18.89	-19.98	-49.92	-19.71	-16.73	-18.20
-24.58	-18.16	-47.95	-17.62	-17.02	-17.41
-20.24	-20.62	-48.76	-17.47	-15.28	-17.23
-20.90	-18.67	-50.71	-19.72	-15.85	-17.39
-18.59	-18.39	-47.95	-17.49	-17.16	-16.30
-23.14	-16.60	-49.75	-18.26	-15.94	-15.55
-19.23	-18.84	-51.55	-19.74	-14.76	-17.40
-19.36	-17.91	-50.31	-19.47	-16.27	-13.28
-19.82	-22.07	-50.91	-18.40	-17.64	-18.18
-20.08	-20.71	-52.62	-19.04	-16.09	-16.22

-20.86	-20.68	-50.45	-19.79	-16.50	-17.65
-20.91	-22.98	-51.87	-21.75	-17.42	-14.29
-18.85	-18.41	-46.12	-15.76	-16.38	-13.85
-21.18	-19.28	-50.71	-17.32	-17.17	-17.11
-21.15	-15.91	-45.43	-13.69	-15.60	-17.79
-21.36	-20.67	-45.88	-16.62	-14.67	-15.45
-19.54	-15.12	-41.76	-14.99	-14.67	-15.25
-20.68	-22.78	-53.40	-18.69	-14.64	-15.81
-21.05	-18.18	-51.99	-16.87	-14.07	-16.02
-21.31	-20.21	-50.33	-20.23	-15.94	-17.25
-21.27	-23.94	-55.11	-19.45	-15.58	-16.56
-20.51	-19.60	-44.69	-19.99	-18.50	-14.64
-19.73	-19.08	-47.08	-17.74	-16.22	-16.35
-18.95	-17.07	-48.57	-16.39	-16.34	-16.60
-22.07	-18.54	-51.61	-20.09	-15.11	-16.71
-21.57	-15.60	-47.38	-16.07	-14.55	-17.55
-20.04	-18.30	-50.38	-16.93	-18.68	-17.38
-23.18	-21.72	-46.78	-17.51	-18.05	-17.20
-19.54	-18.66	-50.53	-18.50	-14.66	-15.32
-20.17	-17.70	-49.42	-16.61	-16.25	-13.02
-18.40	-19.83	-49.30	-16.77	-15.97	-16.41
-20.01	-19.88	-48.10	-14.90	-16.92	-16.74
-19.77	-16.19	-45.76	-16.10	-15.50	-15.86
-18.27	-15.23	-42.15	-15.45	-16.33	-16.03
-21.80	-16.73	-40.57	-18.60	-17.05	-14.64
-20.57	-16.37	-43.83	-15.42	-16.89	-14.73
-20.61	-15.63	-42.37	-14.29	-14.78	-16.01
-19.76	-15.69	-42.65	-16.64	-17.00	-14.24
-20.58	-18.99	-43.45	-14.27	-14.21	-14.65
-19.35	-18.37	-50.10	-16.99	-16.90	-15.92
-22.45	-18.28	-51.93	-19.08	-16.51	-17.80
-20.26	-18.04	-50.34	-19.45	-17.37	-16.94

-20.45	-20.82	-51.17	-20.03	-17.33	-17.87
-21.22	-17.92	-48.15	-16.62	-17.65	-17.67
-20.87	-17.54	-50.94	-19.00	-15.88	-15.55
-20.84	-17.23	-50.52	-18.88	-16.32	-16.32
-20.71	-16.22	-42.81	-14.13	-15.80	-15.53
-20.69	-20.56	-50.62	-15.97	-16.55	-17.02
-19.89	-19.88	-50.02	-15.53	-17.60	-16.69
-19.11	-15.18	-43.00	-16.21	-14.44	-12.79
-19.13	-15.39	-43.32	-14.63	-15.95	-14.45
-21.59	-17.71	-43.11	-16.19	-15.81	-14.96
-23.32	-19.73	-51.63	-18.02	-16.80	-17.22
-21.91	-17.48	-48.91	-16.17	-15.52	-17.09
-21.46	-18.58	-51.76	-17.56	-16.42	-19.42
-21.95	-19.46	-53.27	-18.08	-16.25	-18.37
-20.91	-20.59	-52.66	-19.45	-16.24	-16.64
-20.53	-21.49	-52.32	-19.69	-16.47	-16.98
-22.05	-17.56	-52.31	-19.05	-16.16	-15.50
-19.22	-18.31	-51.56	-19.08	-14.82	-17.37
-22.37	-17.65	-51.95	-19.48	-17.24	-15.86
-21.76	-16.56	-49.90	-18.03	-15.59	-17.50
-21.09	-19.69	-50.54	-18.66	-15.82	-16.72
-22.30	-19.84	-53.46	-19.42	-15.67	-16.40
-18.85	-15.37	-43.34	-15.51	-15.88	-16.73
-20.53	-15.98	-43.20	-15.51	-15.80	-14.38
-19.80	-17.38	-43.59	-14.79	-16.40	-15.70
-21.56	-12.93	-44.82	-16.97	-16.59	-14.64
-20.29	-17.46	-43.19	-13.19	-16.75	-15.65
-20.05	-19.59	-50.00	-17.21	-17.07	-17.79
-21.00	-19.78	-50.48	-17.74	-18.17	-19.37
-19.85	-19.14	-50.87	-16.38	-17.71	-16.64
-21.34	-19.10	-53.03	-18.42	-15.41	-17.60
-21.91	-15.53	-46.70	-16.06	-15.69	-15.80

-23.28	-16.97	-50.02	-19.08	-16.81	-17.14
-20.81	-15.40	-49.82	-18.13	-15.50	-17.55
-20.42	-19.34	-51.69	-19.14	-15.86	-17.30
-20.39	-20.69	-49.66	-19.53	-19.40	-16.11
-19.38	-24.01	-51.78	-21.28	-19.85	-15.53
-20.20	-21.59	-52.76	-17.67	-20.26	-14.87
-20.61	-21.19	-52.66	-18.28	-18.52	-17.03
-19.93	-26.82	-50.13	-17.60	-17.38	-21.03
-22.76	-19.20	-52.69	-21.09	-15.57	-15.36
-20.37	-16.87	-47.09	-16.62	-16.21	-17.39
-19.04	-20.57	-51.80	-21.48	-15.32	-16.67
-20.04	-17.22	-48.22	-15.44	-17.20	-15.91
-18.76	-20.26	-51.78	-17.81	-16.49	-19.75

I the undersigned declare that this thesis is my original work and has not been presented for a Degree in any other university and that all sources of materials used for the thesis have been duly acknowledged.

Teshome Talema Mekonnen. Signature _____ Date_____

School of Earth Science June, 2018

This thesis has been submitted for examination with my approval as university advisor.

Advisor:

Dr. Binyam Tesfaw_____ Signature _____Date_____

Co-Advisor:

_____ Signature _____Date_____